AEROELASTIC RESPONSE OF A TYPICAL WING SECTION UNDER NONLINEARITIES AND GUST LOADS

A Dissertation

by

YOGESH BABBAR

Submitted to the Office of Graduate and Professional Studies of
Texas A&M University
in partial fulfillment of the requirements for the degree of

DOCTOR OF PHILOSOPHY

Chair of Committee,	Thomas W. Strganac
Committee Members,	Edward B. White
	John E. Hurtado
	Othon K. Rediniotis
	Alan Palazzolo
Head of Department,	Rodney Bowersox

May 2015

Major Subject: Aerospace Engineering

ABSTRACT

Aeroservoelasticity (ASE) is the interdisciplinary study of the interaction of structural, inertial, aerodynamic, and control loads for aircraft systems, and is inherently a nonlinear phenomenon. One of the goals of ASE research is to provide active gust load alleviation in aircraft to improve ride quality, minimize airframe fatigue, and increase performance.

The goal of this research is to develop a robust aeroelastic (AE) predictive model for a wing section that represents a typical flexible wing in flight, and which will be used as a platform for developing ASE controllers. The various components of this research, including an unsteady aerodynamic module, a structural module, and a gust module, have been individually developed and validated with experiments. The experimental facility, comprising of a pitch-plunge free vibration apparatus, a real-time gust sniffing sensor, and an oscillating vane gust generator, are designed and developed at Texas A&M as test beds for current and future ASE research.

Both the experiments and predictive model are used to explore nonlinear behavior of the system response. For example, the research has led to experimentally derived bifurcation diagrams depicting possible responses. The limit cycle oscillations (LCO) observed in experiments are captured by the predictive model. The AE model allows for parametric study of wing response on various system features such as nonlinear structural stiffness, nonlinear Coulomb damping, mass imbalance, and other design features. Also, the response of a wing under oncoming gusts is examined. This AE predictive model will serve as a platform to develop ASE models and controllers in future, and the experimental facility will serve as a test bed for validation of developed controllers.

DEDICATION

This work is dedicated to my parents Mr. Om Parkash Babbar and Mrs. Bimla Babbar for having unbounded faith in my ability and for showing immense patience throughout the course of my PhD.

ACKNOWLEDGEMENTS

I would like to thank my adviser, Prof. Thomas Strganac for providing me a environment where I enjoyed freedom to pursue my ideas. He treated me like an equal and that translated into further confidence in my engineering and scientific ability. He was always available for discussions and his inputs provided more clarity into the subject. I enjoyed my life in graduate school and a big reason was a great adviser.

I want to thank my committee members Dr. White, Dr. Hurtado, Dr. Palazzolo and Dr. Rediniotis for giving me guidance through the course of the research as and when I needed.

I also want to thank Arun Mangalam, Senior Scientist, Tao Systems of Integration Inc. for research funding, collaboration and guidance. Arun's keen understanding of industry needs and knowledge of the subject proved helpful at various stages of this work.Thanks also go to NASA and AFRL for providing the funding for this research.

Thanks to my colleague and friend, Vishvas Samuel Suryakumar for providing immense support in data acquisition, signal processing and theoretical conceptualization. It was often a result of long discussions with him that new ideas emerged and major challenges were overcome.

It would not have been possible to complete this work without the support of my wife, Sneha Chawla. The long hours I spent in lab conducting experiments and writing required many sacrifices from her. Her planning skills are a big reason I was able to finish this work in time.

I want to thank William Seward, who provided me insights into mechanical design, and provided major manufacturing support to complete experimental apparatus

on tight deadlines. Through the process, I gained interest in mechanical design for manufacturing.

Last but not the least, I extend my department to the Aerospace Engineering department for facilities and equipment. Yolanda Veals and Andrea Loggins extended full cooperation and guided me through the procurement process for hardware.

NOMENCLATURE

AE	Aeroelastic
ASE	Aeroservoelastic
CFD	Computational Fluid Dynamics
GLA	Gust Load Alleviation
LCO	Limit Cycle Oscillation
ODE	Ordinary Differential Equation
NASA	National Aeronautics and Space Administration
NATA II	Nonlinear Aeroelastic Test Apparatus
PPDS	Pitch Plunge Drive System
TAMU	Texas A&M University
a	Nondimentional location of center of gravity from leading edge
Al	Matrix related to Peter's lag states
b	Wing semi chord
bl	Matrix related to Peter's lag states
c	Wing chord
c_d	Damping coefficient
c_α	Pitch damping
c_h	Plunge damping
$C(k_r)$	Theodoreson's function
$C_{L,\alpha}$	Coefficient of lift curve slope
c_α	Pitch viscous damping coefficient
$C_{M,\alpha}$	Coefficient of moment curve slope
cl	Matrix related to Peter's lag states

dl	Matrix related to Peter's lag states
e	Nondimensional pitch axis location from leading edge
F	External force that drives the system
$F_{c,h}$	Plunge damping force
F_d	Coulomb damping force
$F_{k,\alpha}$	Torsional spring load
F_y	Measured normal force
h	Plunge displacement
$\dot{h}$	Plunge rate
$\ddot{h}$	Plunge acceleration
l	Moment of inertia
I_α	Moment of inertia of pitch support assembly
I_{cam}	Cam moment of inertia
I_w	Wing moment of inertia
k	Linear spring constant
k_r	Reduced frequency
k_1	Pitch stiffness coefficient 1
k_2	Pitch stiffness coefficient 2
k_3	Pitch stiffness coefficient 3
k_h	Plunge stiffness constant
$k_{\alpha,l}$	Linear pitch stiffness
k_h	Plunge stiffness
L	Lift
L_{qs}	Lift as per quasi-steady model
L_s	Lift as per quasi-static model

L_{usp}	Lift as per Peter's model
m	Mass of the system
M	Pitching moment
M_a	Aerodynamic moment
m_α	Total pitching mass
m_{cam}	Pitch cam assembly mass
m_{car}	Mass of plunge carriage
M_g	Moment due to gust
m_h	Plunging mass
M_{qs}	Pitching moment as per quasi-steady model
M_s	Pitching moment as per quasi-static model
M_{us}	Pitching moment as per the unsteady model
M_{usp}	Pitching moment as per the Peter's model
m_w	Wing assembly mass
n_c	Number of cycles
N	Number of induced flow states
q	Dynamic pressure
s	Nondimensional time
$\tilde{s}$	Laplace variable
S	Wing surface area
T	Time period of oscillation
V	Reduced velocity
x	State Vector
$\dot{x}$	State vector derivative
x_α	Center of gravity of total pitching mass

x_{cam}	Center of gravity of cam assembly
x_w	Wing center of gravity aft of pitch axes
U	Freestream velocity
α	Pitch displacement
$\dot{\alpha}$	Pitch velocity
$\ddot{\alpha}$	Pitch acceleration
δ	Logarithmic decrement
$\ddot{h}$	Plunge acceleration
λ_n	Induced flow states
λ_0	Average induced flow velocity
ω	Circular frequency
ω_α	Reference frequency for non-dimensionalisation
Ω_F	Flutter frequency
ρ	Density of air
ζ_α	Non-dimensional pitch damping ratio
ζ_h	Non-dimensional plunge damping ratio

TABLE OF CONTENTS

Page

ABSTRACT ii

DEDICATION iii

ACKNOWLEDGEMENTS iv

NOMENCLATURE vi

TABLE OF CONTENTS x

LIST OF FIGURES xii

LIST OF TABLES xvi

1. INTRODUCTION 1

1.1 Aeroelasticity 1
1.2 Nonlinear aeroelasticity: Wind Tunnel Studies 2
1.3 Identification of Gust Response 2
1.4 Previous Work and Motivation for Current Research 3
1.5 Research Objectives and Methodology 5

2. THEORY 9

2.1 Aerodynamic Models 9
2.2 Structural Model and damping 13
2.3 Idealized aeroelastic system system 16

3. EXPERIMENTAL SETUP 18

3.1 Wind Tunnel 19
3.2 Pitch Plunge Drive System 19
3.2.1 Pitch Module 21
3.2.2 Plunge Mechanism 24
3.2.3 Wing Assembly 26
3.2.4 Sensor Suite and Actuators 27
3.3 PPDS as Gust Generator 27
3.4 Gust Sniffer 29

3.5 Nonlinear Aeroelastic Test Apparatus II 29
3.6 Complete Setup 31

4. AEROELASTIC SYSTEM EQUATIONS AND IDENTIFICATION 33

4.1 Equations of motion for NATA II wing 33
4.2 System Identification 36
4.2.1 Wing inertial parameters 37
4.2.2 Wing aerodynamic parameters 40
4.2.3 Mount stiffness parameters 41
4.2.4 Mount damping parameters 43
4.2.5 Mount inertial parameters 46

5. VALIDATION OF COMPONENT MODELS 48

5.1 Validation of Aerodynamic Models 48
5.2 Validation of structural model 50

6. PREDICTIVE AEROELASTIC MODELS 54

6.1 Flutter Speed Prediction 54
6.1.1 Flutter speed of a typical section 55
6.1.2 Flutter speed of wing on NATA 62
6.2 Time domain aeroelastic model 65

7. MODELING AND VALIDATION OF GUST LOADS 71

7.1 Gust Sniffer Calibration 72
7.2 Gust Loads Model Identification 72
7.3 Aeroelastic loads under harmonic gust 76

8. RESULTS AND DISCUSSION: NONLINEAR AEROELASTIC RESPONSE 81

8.1 Aeroelastic behavior of Linear System: Simulations 81
8.2 Effect of Stiffness Nonlinearity on Aeroelastic Response: Simulations 84
8.3 Effect of Damping Nonlinearity on Aeroelastic Response: Simulations 85
8.4 Stable and unstable boundaries: Simulations 87
8.5 Stable and unstable boundaries: Simulations and Experiments comparison 89

9. CONCLUSIONS AND FUTURE WORK 94

BIBLIOGRAPHY 96

APPENDIX A 99

LIST OF FIGURES

FIGURE		Page
1	Aeroservoelasticity and related fields of study	1
2	Schematic of LCO response. Reprinted from Figure 1 [1] with permission; Strganac, April, 2015	5
3	Schematic for a response based ASE Control	6
4	Schematic for ASE Control enhanced with gust information	6
5	Schemetic for ASE control elements targeted in current research	7
6	General Aeroelastic Section	9
7	A simple spring mass damper system with viscous damping and Coulomb damping	13
8	Typical system response with viscous damping	14
9	Typical system response with Coulomb damping	16
10	Simplified general aeroelastic system	17
11	Overview of experimental setup	18
12	Gust Generator as installed on test section. Major components: 1.Frame, 2.Pitch Module, 3.Plunge mechanism, 4.Wing assembly	21
13	Pitch Module detailed view. Major components: 1.Back plate, 2.Wall, 3.Pitch actuator, 4.Mini wall, 5.Gearbox, 6.Motor shaft, 7.Drive shaft, 8.Wing shaft, 9.Crank. 10.Drive pin, 11.Connecting rod, 12.Wing bar, 13.Spine, 14.Extension channel, 15.Plunge encoder	22
14	Plunge mechanism 1. Plunge motor, 2. Main drive shaft, 3. Primary belt drive, 4. Secondary belt drive, 5. Plunge drive shaft, 6. Plunge crank wheel, 7. Plunge crank pin, 8. Counterweight, 9. Plunge connecting rod, 10. Flywheel	24

15 Wing balance sub-assembly. 1. AOA Plate, 2. Balance, 3. Balance interface plate, 4. Offset plate, 5. Wing mount tube 26

16 Schematic of PPDS actuation and data acquisition map 28

17 A sketch of Gust Sniffer 29

18 NATA II and Wing detailed drawing 30

19 Front View from inside the test section 31

20 Side View of the experimental setup 31

21 Wing mounted on NATA 34

22 Identification of wing mass as the slope of linear fit between measured normal force and plunge acceleration. $m_w = 4.03\ kg$ 38

23 Identification of wing c.g. location as slope of linear fit between measured pitching moment and normal force. $x_w = 0.0364\ m$ 39

24 Identification of wing moment of inertia as slope of linear fit between measured pitching moment and pitch acceleration. $I_w = 0.0260\ kg\ m^2$ 40

25 Identification of wing aerodynamic parameters. $C_{L_\alpha} = 5.45$ and $C_{M_\alpha} = 0.183$ 41

26 Identification of plunge stiffness. $k_h = 2641.8\ N/m$ 42

27 Identification of pitch stiffness. k_4=2302.1 Nm/rad, k_3=933.5 Nm/rad^2, k_2=10.6 Nm/rad^3, k_1=18.7 N/m 43

28 Identification of pitch damping (viscous model). $\zeta_\alpha = 0.0322$ 44

29 Identification of plunge damping (Coulomb case: $F_d = 2.0 \pm 0.5\ N$, Viscous case: $\zeta_h = 0.0416$) 45

30 Determination of optimum number of lag states for Peter's model for C_L 48

31 Comparison and Validation of aerodynamic models with experiments for C_L 50

32 Comparison and Validation of aerodynamic models with experiments for C_M 51

33 Validation of modeled pitch damping (viscous) with experiments . . . 52

34 Validation of modeled plunge damping (viscous and Coulomb) with experiments . . . 53

35 Flutter speed prediction for the Hodges wing with quasi static and unsteady aerodynamic models . . . 57

36 Flutter speed prediction of NATA wing as a function of aerodynamic models with damping values $\zeta_h = 0.0416, \zeta_\alpha = 0.0322$ . . . 63

37 Effect of structural damping on predicted flutter speed . . . 64

38 Effect of wind speed, U, on LCO response at the same plunge initial condition of $h_0 = 0.005\ m, \alpha_0 = 0\ rad$ . . . 67

39 Effect of plunge initial condition on LCO response at $U = 13\ m/s$ . . . 68

40 Effect of plunge initial condition on flutter response of linear system at $U = 13\ m/s$ . . . 70

41 A sketch of Gust Sniffer . . . 71

42 Gust Sniffer Calibration at various wind speeds . . . 72

43 Measured Gust angle and lift as input experimental data for model development . . . 74

44 Comparison of Step response of gust model with theoretical models . . . 75

45 Comparison of predictions of gust model theoretical models with measured data . . . 76

46 Comparison of predictions of gust model theoretical models with measured data at $U \approx 10\ m/s$ . . . 77

47 Comparison of predictions of gust model theoretical models with measured data . . . 79

48 Comparison of predictions of gust model theoretical models with measured data . . . 80

49 Determination of flutter boundary for the linear system . . . 82

50 Validation of flutter boundary location: time domain behavior (refer back to last figure) . . . 83

51 Comparison of predictions of gust model theoretical models with measured data 84

52 LCO amplitude prediction for limiting values of identified total pitch inertia 85

53 Comparison of predictions of gust model theoretical models with measured data 86

54 Schematic of LCO response. Figure 1 from [1] 87

55 Effect of identification errors on stable and unstable boundaries . . . 88

56 Comparison of predicted and measured unstable boundaries 89

57 Comparison of predictions of gust model theoretical models with measured data 90

58 Comparison of predictions of gust model theoretical models with measured data 91

59 Experimental boundaries 93

LIST OF TABLES

TABLE Page

1 Parameters and capabilities of PPDS 20

2 Parameters to be estimated from System Identification techniques . . 37

3 Identified aeroelastic system parameters 47

1. INTRODUCTION

1.1 Aeroelasticity

Aeroelasticity is the study of the interaction between aerodynamic, elastic and inertial loads (forces and moments) generated in elastic structures in an airstream. On an airplane, control surface deflection will exert loads which further interact with the aeroelastic forces. Such interaction is studied under the field of Aeroservoelasticity. Figure 1 shows the expanded version of classical Collar Diagram of aeroelasticity including control effects. Depending on the flight regime, other factors such as shock waves or thermal effects may interact with the aeroelastic loads making the phenomenon more complicated.

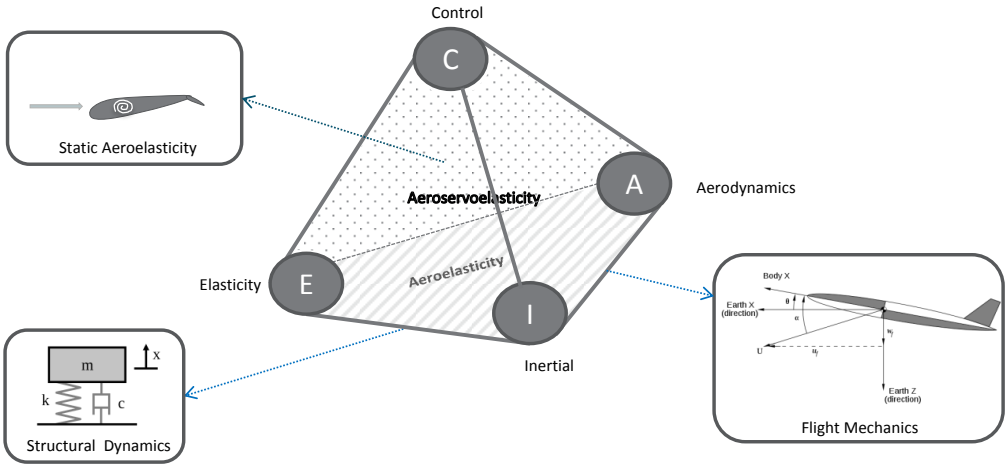

Figure 1: Aeroservoelasticity and related fields of study

The four corners of this pyramid represent the four types of loads arising due to elasticity, inertial, aerodynamic and control aspects. Hodges [2] elucidates the

fields of study involving the interaction of a combination of these aspects. The field of structural dynamics wherein the classical problems of spring, mass, damper and simple and compound pendulum are studied falls at the juncture where elastic and inertial loads interact. In above figure, it is represented by the edge of the pyramid connecting the vertices E and I. The field of flight mechanics, where rigid body aircraft motion is studied falls at the juncture of aerodynamic and inertial loads. Similarly, the field of static aeroelasticity, wherein problem of aeroelastic divergence is studied falls at the juncture of elastic loads and aerodynamic loads . The problem of control reversal falls on the plane including the vertices C, E and A represented as the back face of the pyramid. Aeroelasticity falls at the base of this pyramid between the vertices E, I, and A.

1.2 Nonlinear aeroelasticity: Wind Tunnel Studies

Aeroelasticity is nonlinear by its very nature. Individual disciplines such as aerodynamics and structures, that make up aeroelasticity have their individual nonlinear contributions. For example, at high angles of attack, the lift force generated by a wing does not remain a linear function of angle of attack. Tang and Dowell [3] describe the impact of aerodynamic nonlinearities on aeroelastic behavior in rotorcraft. Kim and Strganac [4] present studies in nonlinear aeroelastic behavior of a cantilevered wing in presence of wing stall. The effect of geometric nonlinearities on aeroelastic behavior, and effects of the addition of stores on a wing, are highlighted by Thompson and Strganac [5].

1.3 Identification of Gust Response

Aeroelastic induced vibrations may initiate due to a variety of reasons such as control surface vibration, pilot input, maneuver loads, transonic aerodynamic effects such as shock waves and atmospheric turbulence. The SensorCraft effort at NASA [6]

explored the development of Aeroservoelastic (ASE) models and gust load alleviation (GLA) control laws [7]. Silva has employed similar system identification techniques for identification of unsteady loads on computational fluid dynamics (CFD) as well as experimental data [8,9]. The ASE model was determined by system identification techniques using harmonic oscillations by gusts and control surface deflections. The current research follows a similar technique for identification of gust loads on the wing by extracting a transfer function between measured loads and measured gust angle. Classical methods for determination of gust loads are limited. Kussner's function [10] provides the indicial lift developed over an airfoil as it passes through sharp edged gust and using convolution, the step response may be used to generate lift for an arbitrary gust profile. However, as observed by Bisplinghoff [11], there has been limited experimental validation of the predictions of Kussner's function. In this research, we present comparisons of experimentally extracted step response with the the Kussner function. The extracted model is then coupled with unsteady aerodynamic models to predict aeroelastic loads under gust.

1.4 Previous Work and Motivation for Current Research

Slender aeroelastic structures such as airplane wings and wind turbine blades are inherently flexible. For example, commercial aircraft wings may deflect upto 10% of span [12]. At flight speeds above a critical value, the aerodynamic loads may produce a situation where the overall aeroelastic damping of the system is negative, leading to wing flutter which is characterized by divergent oscillations. Structural nonlinearity such as those exhibited by a hardening spring may allow the structure to oscillate with in certain bounds. These oscillations are called Limit Cycle Oscillations (LCO). LCOs are observed in high performance aircraft such as the F-16 and F/A-18 [13,14]. Denegri [14] noted that while linear flutter prediction techniques predicted

LCO frequency accurately, they were not suitable for predicting LCO onset speed and LCO amplitude.

Dowell et. al [1] present the general behavior of aeroelastic limit cycle oscillations for various levels of structural nonlinearity in stiffness. The behavior is represented in Figure 2. This representation of LCO amplitude plotted against wind speed is called a bifurcation diagram. The flight speed (or wind tunnel velocity), is also the bifurcation parameter. A fully linear system exhibits unbounded oscillations beyond a critical flight speed, called the flutter speed. On a bifurcation diagram, this behavior is represented as a vertical line passing through flutter speed. Bifurcation diagrams have been extensively used in this research to highlight, and compare the nonlinear behavior of aeroelastic system studied herein. Both simulations and experiments are used to generate these bifurcation diagrams.

For a system with a nonlinearity such as structural hardening stiffeness or an aerodynamic softening from stall, the behavior is best represented as a curve passing through flutter speed and bending to the right. The amount of nonlinearity determines the severity of the bend. Nonlinear structural damping such as dry friction may lead to a situation where LCO may exist even before the flutter speed if the disturbance is substantial.

Other nonlinear phenomena such as subharmonic resonance, beating etc may also happen in presence of nonlinearities. Quoting the authors of [1], "These behaviors have been delineated and studied using low-order model problems in the nonlinear dynamics literature; however, in aeroelastic wind-tunnel and flight testing, the detailed knowledge required to identify these nonlinear behaviors has rarely been available." In this research, the nonlinear phenomena, especially around the flutter speed, are studied in-depth through experiments and analytical studies.

At Texas A&M University, the Nonlinear Aeroelastic Test Apparatus (NATA) was

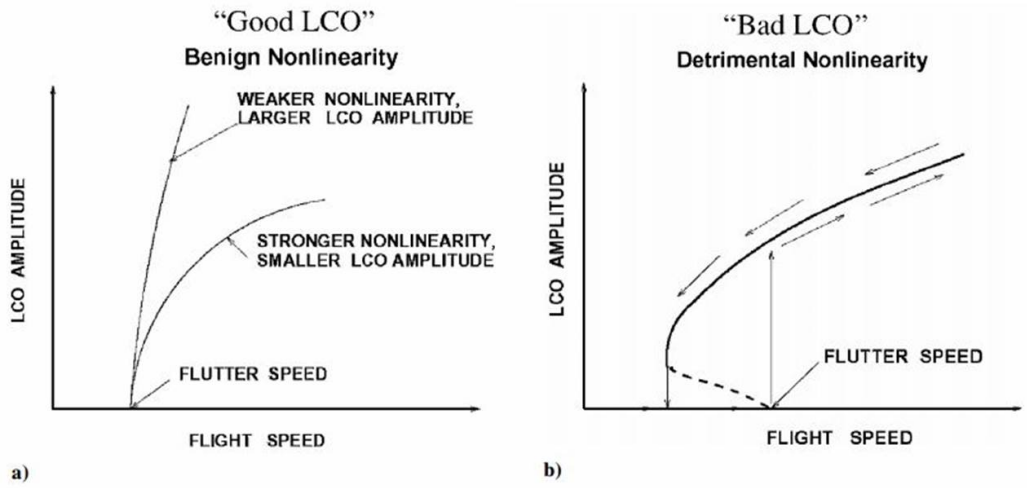

Figure 2: Schematic of LCO response. Reprinted from Figure 1 [1] with permission; Strganac, April, 2015

built with a vision to explore the nonlinear behavior of limit cycle oscillations and develop ASE control laws. Numerous studies pertaining to aeroelastic response, and nonlinear control of LCO using leading edge and trailing edge actuators have been conducted over the last decade [15–18]. A new experimental facility built around the 3'x4' low speed wind tunnel includes an updated NATA (NATA II), a pitch plunge forced oscillation system (PPDS) which doubles as a gust generator, and a gust sniffing sensor. Additional sensors on NATA II allow better system identification and validation of component models. Recent research using this facility includes validation of aerodynamic models and gust response of aeroelastic wings [19–21]. This thesis presents aspects of recent work as well as development of a robust AE model including the aspects of gust.

1.5 Research Objectives and Methodology

Figure 3 shows a schematic of a typical closed loop ASE control system. In such a control system, accelerometers are employed to measure aeroelastic response and

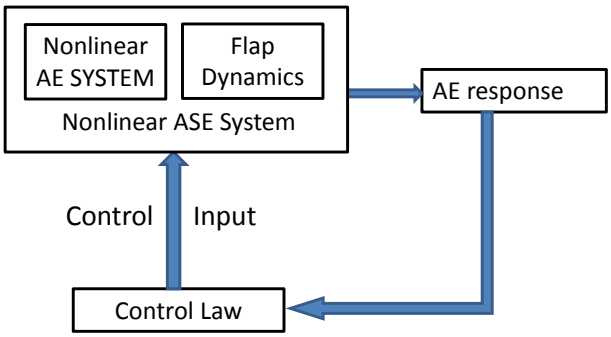

Figure 3: Schematic for a response based ASE Control

this information is used to synthesize a control input in the form of a control surface deflection. The control law is designed to meet an ASE goal such as response minimization or gust load alleviation. Such control systems have been employed on civil as well as military aircraft [22]. Figure 4 shows the ASE control system enhanced with gust information. The gust is sensed moments before it hits the wing and the information is supplied to the control system which combines it with the response information for computation of control input. Implementing such a controller in

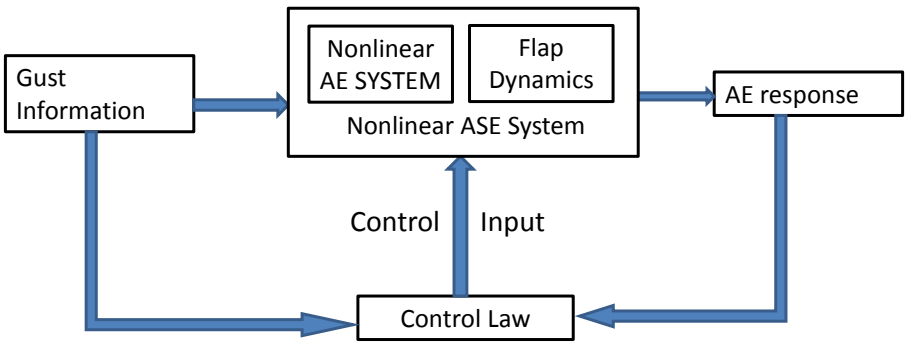

Figure 4: Schematic for ASE Control enhanced with gust information

the presence of gust loads requires various elements to be developed and validated

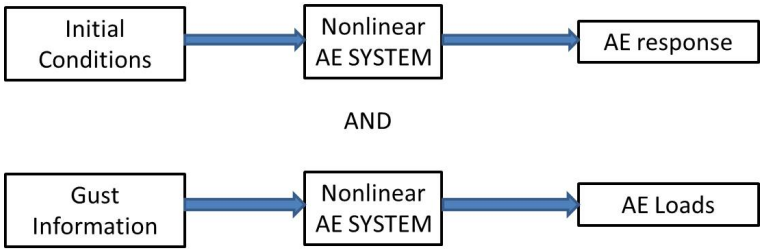

Figure 5: Schemetic for ASE control elements targeted in current research

separately. The present research targets two such elements, using the research experimental resources in the wind tunnel. The first element is to characterize the nonlinear aeroelastic system through experiments and analytical studies. The second element establishes a model between measured gust and generated loads and further combine the model with aeroelastic models to predict unsteady aeroelastic loads under gust. These elements form two branches of the complex problem of validation of ASE controllers under gust loads. The specific objectives of this research are listed as

- Develop an aeroelastic model describing the wing's response as mounted on experimental setup, conduct simulations and validate various aspects of the model with experiments.
- Develop system identification techniques for accurately estimating system parameters necessary for simulation.
- Develop the experimental hardware including flexible pitch plunge mount oscillation hardware, a gust generator and a gust sniffing sensor.
- Identify a gust model relating measured gust angle to loads. This model is integrated with aeroelastic model to extend its capabilities to handle gusts.

- Compare the predictions of AE model with experimental results and explore the effects of various nonlinearities
- Study the interaction between oncoming gusts with the aeroelastic system. Compare model predictions with experimental findings

The organization of this thesis is as follows. The theoretical concepts regarding unsteady aerodynamics, structural modeling, and a typical aeroelastic system are explained in Section 2. The design, development of the experimental setup is described in Section 3. Section 4 starts with the derivation of aeroelastic system equations corresponding to the experimental setup. The system identification techniques for identification of each of the system parameters are then presented. The development of predictive models for flutter speed and time domain aeroelastic response are presented in Section 6. The gust loads identification, validation and the design and development of the gust sensor are presented in Section 7. The developed model is coupled with previously developed aeroelastic models to predict aeroelastic loads under gust. Finally, results and discussions pertaining to nonlinear behavior of aeroelastic system are presented in Section 8.

2. THEORY

This chapter presents the theoretical concepts and fundamentals related to various aspects of nonlinear aeroelastic response and gust loads. First, three aerodynamic models are described. These aerodynamic models are used in further sections in determination of flutter speed and aeroelastic response. The representation of a structural system as a second order Ordinary Differential Equation (ODE) is then discussed along with the techniques used for identification of viscous and Coulomb damping. The equations of motion for a simple aeroelastic system are then presented. This system is later evolved to represent the wing used in experimental studies as shown in later sections.

2.1 Aerodynamic Models

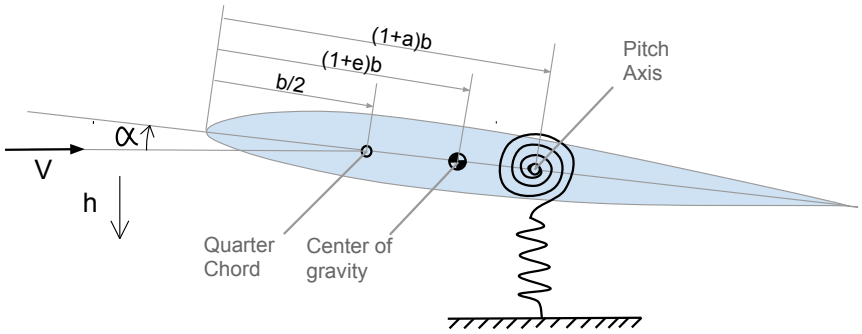

Figure 6: General Aeroelastic Section

This research focuses on a typical wing section in steady airflow. Since the test article is a wing section spanning the wind tunnel walls, will only discuss two dimensional linear aerodynamic models and not include any effects of stall.

As per quasi-static model, the lift on a unit span wing section with semi-chord, b, immersed in an airstream with velocity, U, at an angle of attack, α is given as

$$L = 2\pi\rho U^2 bS\alpha \tag{1}$$

The pitching moment at the pitch axis is given as

$$M = M_{\frac{c}{4}} + b(\frac{1}{2} + a)L = 0 \tag{2}$$

where a is defined as a measure of location of pitch axis as shown in Figure 6. $M_{\frac{c}{4}}$ is the pitching moment at quarter chord and is zero as per thin airfoil theory. This model may be tailored to reflect the experimental apparatus in the wind tunnel. For the wing with span, b, lift curve slope, $C_{L,\alpha}$ and effective moment curve slope, $C_{M,\alpha}$, the lift and moment may be written as

$$L_s = C_{L,\alpha}\rho U^2 bS\alpha \tag{3}$$

$$M_s = C_{M,\alpha}\rho U^2 b^2 S\alpha \tag{4}$$

Since quasi-static aerodynamic model is based on instantaneous angle of attack alone, it does not capture the unsteady effects that arise due to motion of airfoil. These effects are captured in part by the quasi-steady model which takes into account the rate of change of pitch and plunge displacements. The equations for lift and pitching moment about pitch axis are given as

$$L_{qs} = C_{L,\alpha}\rho U bs(\dot{h} + U\alpha + b(\frac{1}{2} - a)\dot{\alpha}) \tag{5}$$

$$M_{qs} = C_{M\alpha}\rho U b^2 s(\dot{h} + U\alpha + b(\frac{1}{2} - a)\dot{\alpha}) \tag{6}$$

In order to quantify the rate of unsteadiness of an oscillating wing, a parameter,k_r, called the reduced frequency is defined.

$$k_r = \frac{wb}{U} \tag{7}$$

w is the circular frequency of oscillation, b is the wing semi-chord, and U is the freestream wind velocity. The full unsteady aerodynamic model was derived by Theodorsen [23] and includes a complex term $C(k_r)$ which is a function of reduced frequency, k_r, and models the reduction in lift amplitude at higher reduced frequencies. Although the quasi-steady model captures the rate effects; the flow acceleration effects, also called the added mass effects are not captured.These effects arise due to the sudden acceleration and deceleration of the wing and are proportional to the second derivative of pitch and plunge angle. The lift as per Theodoreson's model is given as

$$L = \pi\rho b^2 s(\ddot{h} + U\dot{\alpha} - ba\ddot{\alpha}) + C_{L,\alpha}\rho U b s C(k_r)(\dot{h} + U\alpha + b(\frac{1}{2} - a)\dot{\alpha}) \tag{8}$$

Since $C(k_r)$ is a complex number, this model does not allow a time domain simulation for arbitrary pitch and plunge maneuvers. Peters [24] model based on lag states, alleviates this problem. Peters replaces $C(k_r)$ with λ_0 which represents average induced flow velocity. It should be noted that these induced flow velocity states capture memory effects in the flow which can be important at high reduced frequencies. The lift and moment, as per Peter's model are given as

$$L_{usp} = \pi\rho b^2 s(\ddot{h} + U\dot{\alpha} - ba\ddot{\alpha}) + C_{L,\alpha}\rho U b s(\dot{h} + U\alpha + b(\frac{1}{2} - a)\dot{\alpha} - \lambda_0) \tag{9}$$

$$M_{usp} = b(\frac{1}{2} + a)L_{usp} - \pi\rho b^3 S(\frac{1}{2}\ddot{h} + U\dot{\alpha} + b(\frac{1}{8} - \frac{a}{2})\ddot{\alpha}) \tag{10}$$

λ_0 is the average induced flow velocity given by

$$\lambda_0 \approx \frac{1}{2}\sum_{n=1}^{N} Bl_n \lambda_n \tag{11}$$

N is the total number of induced flow states. In the current work, upto 8 states have been studied and it is observed that no more than unsteady lift is insensitive to number of states for $N \geq 6$. Thus the total number of states has been chosen to be 6 for Peter's method. λ_n follow the state equation:

$$[Al]\{\dot{\lambda}\} + \frac{U}{b}\{\lambda\} = \{cl\}(\ddot{h} + U\dot{\alpha} + b(\frac{1}{2} - a)\ddot{\alpha}) \tag{12}$$

and

$$[Al] = [Dl] + \{dl\}\{bl\}^T + \{cl\}\{dl\}^T + \frac{1}{2}\{cl\}\{bl\}^T \tag{13}$$

In the above equations, bl, cl, dl and Dl are known functions [2] of n and N and are given as.

$$bl_n = \begin{cases} (-1)^{(n-1)}\frac{(N+n-1)!}{(N-n-1)!}\frac{1}{(n!)^2}, & \text{for } n \neq N \\ (-1)^{(n-1)}, & \text{for } n = N \end{cases} \tag{14}$$

$$dl_n = \begin{cases} \frac{1}{2}, & \text{for } n = 1 \\ 0, & \text{for } n \neq 1 \end{cases} \tag{15}$$

$$cl_n = \frac{2}{n} \tag{16}$$

For $k_r < 0.1$, the flow is mildly unsteady and it is common to make the assumption

$C(k_r) \sim 0$ and $\lambda_0 \sim 0$. Thus the simplified unsteady aerodynamic model is given as

$$L_{us} = \pi\rho b^2 S(\ddot{h} + U\dot{\alpha} - ba\ddot{\alpha}) + C_{L,\alpha}\rho UbS(\dot{h} + U\alpha + b(\frac{1}{2} - a)\dot{\alpha}) \tag{17}$$

$$M_{us} = C_{M,\alpha}\rho Ub^2 S(\dot{h} + U\alpha + b(\frac{1}{2} - a)\dot{\alpha}) - \pi\rho b^3 S(\frac{1}{2}\ddot{h} + U\dot{\alpha} + b(\frac{1}{8} - \frac{a}{2})\ddot{\alpha}) \tag{18}$$

These aerodynamic models are compared against each other and experimental measurements in Section 5 and used in predicting aeroelastic behavior of the wing in Section 6.

2.2 Structural Model and damping

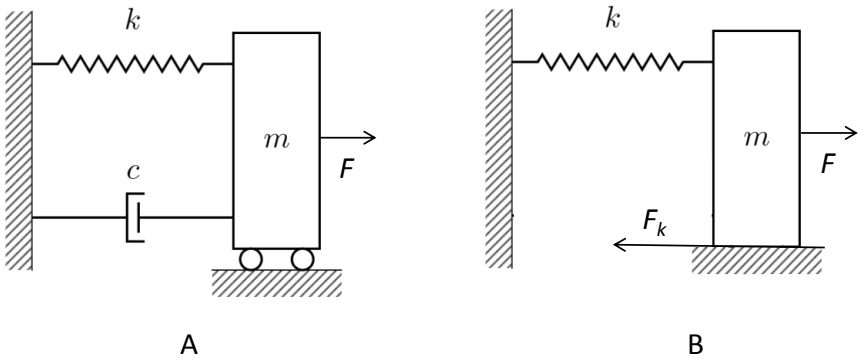

Figure 7: A simple spring mass damper system with viscous damping and Coulomb damping

Figure 7 shows a simple spring mass system under two kinds of damping. Here, m is the mass of the system, k is the linear spring constant and, F is the external force that drives the system. Case 'A' shows a dashpot type viscous damper which

opposes the motion with a force proportional to the instantaneous velocity of the mass, and in a sense opposite to the motion. The coefficient of proportionality is called the damping coefficient, c_d and the damping force is $c_d\dot{y}$. The equation of motion for such a system may be written as

$$m\ddot{y} + ky + c_d\dot{y} = F \tag{19}$$

Figure 8 shows the behavior of such a system when released from an initial displacement. In presence of viscous damping, the system shows damped oscillations with peaks following an exponential decay. The value of damping coefficient may be determined though logarithmic decrement (log-dec) method described below. For any

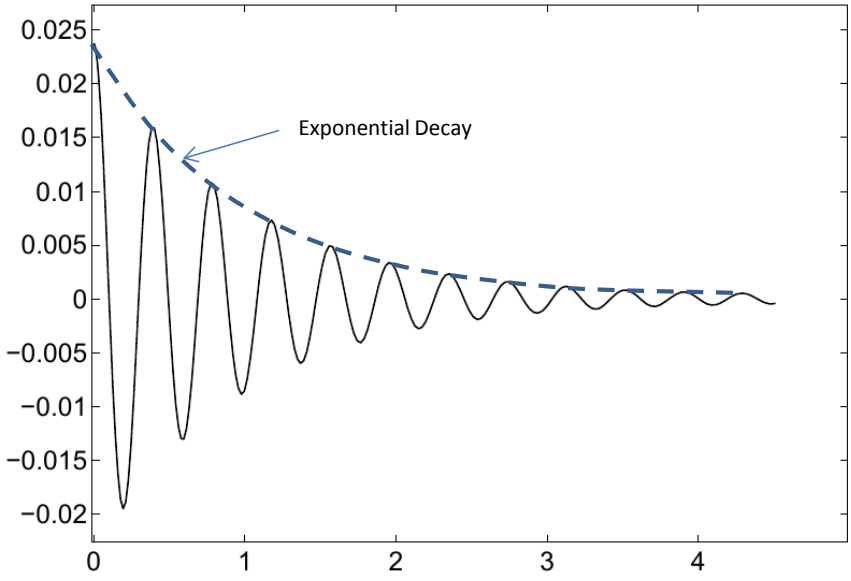

Figure 8: Typical system response with viscous damping

two peaks, n_c cycles apart, with amplitudes y and $y(t + n_cT)$, where T is the time period of oscillation, the logarithmic decrement, δ is defined as

$$\delta = \frac{1}{n_c}\ log\frac{y(t)}{y(t+nT)} \tag{20}$$

The damping ratio, ζ is a nondimensional number often expressed as percentage related to δ such that

$$\zeta = \frac{1}{\sqrt{1 + (\frac{2\pi}{\delta})^2}} \tag{21}$$

In the current research, viscous damping is often expressed using ζ. The damping coefficient may be then found using the relation

$$c_d = 2\sqrt{mk}\ \zeta \tag{22}$$

Not all systems exhibit viscous damping behavior. The systems which involve sliding type motion are likely to show damping behavior wherein the damping force, F_d, is constant and does not vary with speed but still always opposes motion. The damping force may be written as $F_d\ sign(\dot{y})$ and the equation of motion for such a system is

$$m\ddot{y} + ky + F_d\ sign(\dot{y}) = F \tag{23}$$

In case of coulomb damping, the system shows a linear decay such that the difference between any two peaks is constant. This difference in any two consecutive peaks Δy is related to the damping force as

$$\frac{k\Delta y}{4} = F_d \tag{24}$$

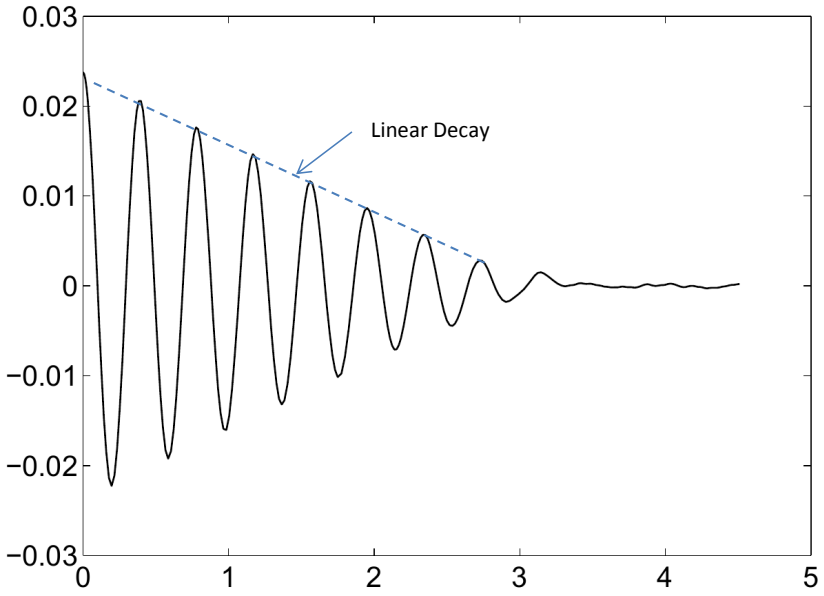

Figure 9: Typical system response with Coulomb damping

2.3 Idealized aeroelastic system system

The general two degree-of-freedom aeroelastic system [2] is represented in figure 6. The location of center of gravity and pitch axis location are represented by quantities a, and e respectively. In present study, the pitch axis is fixed at quarter chord and the location of center of gravity of the wing section is represented as x_α such that the following apply.

$$a = -\frac{1}{2} \tag{25}$$

$$b(a - e) = x_\alpha \tag{26}$$

The simplified aeroelastic wing section is shown in Figure 10. The equations of motion for this system are presented by Equations 27 and 28.

$$m\ddot{h} + mx_\alpha\ddot{\alpha} + k_h h = -L \tag{27}$$

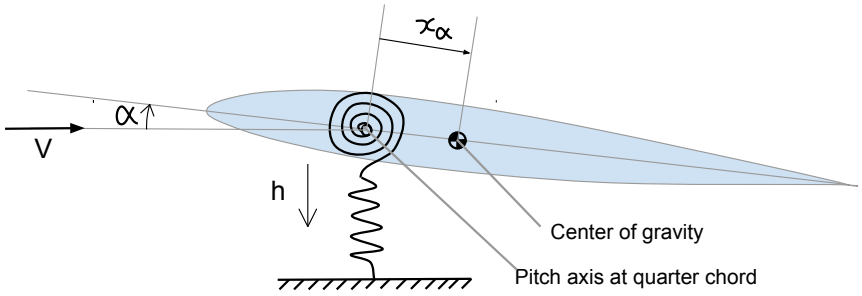

Figure 10: Simplified general aeroelastic system

$$I\ddot{\alpha} + mx_\alpha \ddot{h} + k_\alpha \alpha = M \tag{28}$$

The aeroelastic system is represented by a system of two linear coupled second order ordinary differential equations. The left hand side of these equations represent the structural loads associated with inertia and stiffness and right hand side represents the aerodynamic loads in plunge and pitch degrees of freedom, namely the lift and pitching moment about the elastic axis. The aerodynamic loads may be represented by a suitable aerodynamic model such as quasi static, quasi-steady or unsteady models described in section 2.1.

3. EXPERIMENTAL SETUP

The purpose of the experimental setup is to provide an environment to generate, measure and validate the response of a flexible wing section in the wind tunnel under transverse gust conditions. Figure 11 shows an overview of experimental setup and problem definition. The experimental setup is composed of two hardware systems or mechanisms namely, the Pitch Plunge Drive System (PPDS), and Nonlinear Aeroelastic Test Apparatus (NATA). A wing mounted on PPDS (called PPDS wing or gust wing) is actuated on command and generates gusts which travel downstream providing unsteady flow conditions for the test wing mounted on the free vibration system, NATA. Before the gust hits the test wing on NATA, the gust field generated

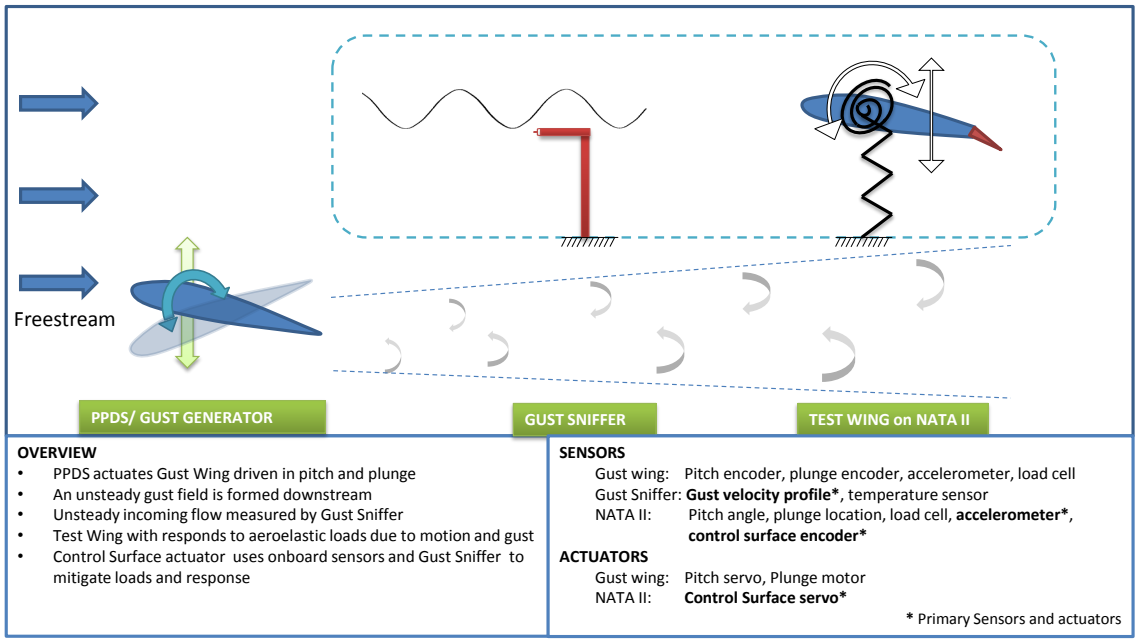

Figure 11: Overview of experimental setup

by PPDS wing is sensed by the Gust Sniffer as flow angularity. This gust sniffer sensor provides a measurement of flow angularity which is used for measuring aeroelastic loads under gust. The experimental setup features a host of sensors such as multi-component load cell, position sensors, and accelerometers. The sensor suite provides redundancy in measurements which is helpful in data filtering and system identification.

3.1 Wind Tunnel

The Texas A&M University 3'X4' low speed wind tunnel is a closed circuit tunnel powered by a constant pitch fan at variable rpm providing a top speed of 50 m/s. The tunnel temperature is maintained between 14°C and 16°C. The turbulence intensity of the tunnel is approximately 0.5%. The tunnel has multiple removable 7' long test sections. One test section has been fitted with the experimental setup for this research.

3.2 Pitch Plunge Drive System

Primarily, the Pitch and Plunge Drive System (PPDS) is built as a test-bed for conducting unsteady aerodynamic experiments. For the current research, the system acts as a gust generator as the unsteady wake from the oscillating wing provides unsteady wind for the downstream test wing. This section first describes the detailed design of PPDS and then presents its role as a gust generator.

PPDS is an experimental apparatus that provides independent pitch and plunge motions for a 4' wing supported on both ends or a cantilevered wing of length up to 4'. It also provides a measurement of unsteady aerodynamic loads, pitch and plunge positions and accelerations in real time. Figure 12 shows the overall view of PPDS as built around the removable test section. The direction of flow is from left to right. There are four major sub-assemblies that make up the PPDS, namely

frame, pitch modules (one on either side of the test section), plunge mechanism and wing assembly. The two pitch modules are free to slide on the rails on the frame. These modules are plunged synchronously by two slider crank mechanisms which are a part of the plunge mechanism. The wing assembly is free to pitch in ball bearings mounted within the pitch modules. Effectively, the wing has two degrees of freedom in pitch and plunge. The drive for pitch motion is provided by two independent but electronically synchronized servo motors mounted in the pitch modules. The plunge motion drive is provided by a single 3-phase AC motor placed underneath the test section. As per this design, the pitch mode rides on the plunge mode as the plunge motor drives the two pitch modules and the wing-balance sub-assembly together as a single payload and the pitch drive is contained in each pitch module rendering the two motions uncoupled. What separates this experimental setup from others is a unique combination of speed and size, and the choice of direct drive or indirect drive. Table 1 shows detailed capabilities of PPDS. The full description of PPDS systems and capabilities are provided in the paper by Babbar et. al [19]. Below is

Table 1: Parameters and capabilities of PPDS

Capability/Parameter	**Pitch motion**	**Plunge motion**
Control type	Closed loop	Open loop
Port/Starboard syncing	Electronic	Mechanical
Oscillation frequency	0 - 10 Hz	0 - 5 Hz
Oscillation amplitude	2 - 22 deg	0.5 - 3 in
Frequency ramp	Yes	Yes
Mean position	0 - 360 deg	6 in
Axis	Spanwise, adjustable	Vertical

a detailed description of each of PPDS's subsystems.

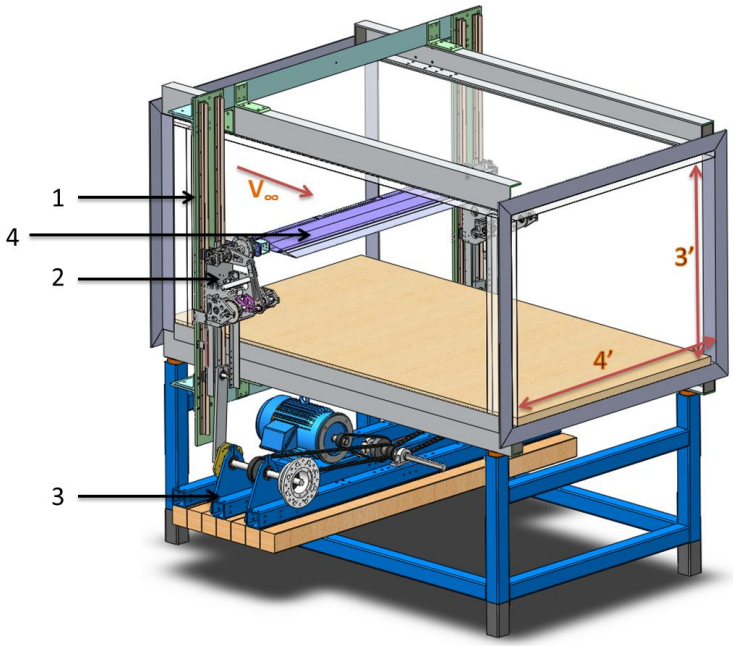

Figure 12: Gust Generator as installed on test section. Major components: 1.Frame, 2.Pitch Module, 3.Plunge mechanism, 4.Wing assembly

3.2.1 Pitch Module

Pitch Module is the assembly responsible for generating and measuring pitch motion. There are two pitch modules which are exact mirror images of each other and contain identical parts. If the wing is rigid, one pitch module is enough to induce pitch motion. If the test demands differential pitch or twist motions at the two ends, the it may be made possible with the second pitch module. Within each module, the pitch motion is carried out by components such as servo motor, gearbox and a four bar mechanism which is an indirect way to drive the wing as opposed to the direct coupling of motor shaft and wing shaft. There is an advantage for the indirect drive. For large amplitudes oscillation (10°to 22°), in order to reduce loads on the pitch motor, it is spun at constant rpm and the oscillation is generated by the four-bar mechanism by design. In this mode, the amplitude of oscillation is

varied in hardware and the motion is periodic. For small amplitudes (0.5°to 15°), the motor may be commanded an oscillating position which translates directly to the oscillating wing. This mode allows for complete freedom in choosing the motion profile including aperiodic motions, custom acceleration, and special maneuvers such as perch maneuver (pitch and hold). Each pitch module is fitted with 4 linear bearings compatible with steel rails mounted to the frame allowing free vertical sliding motion (plunge) driven by the plunge connecting rods. Figure 13 shows the

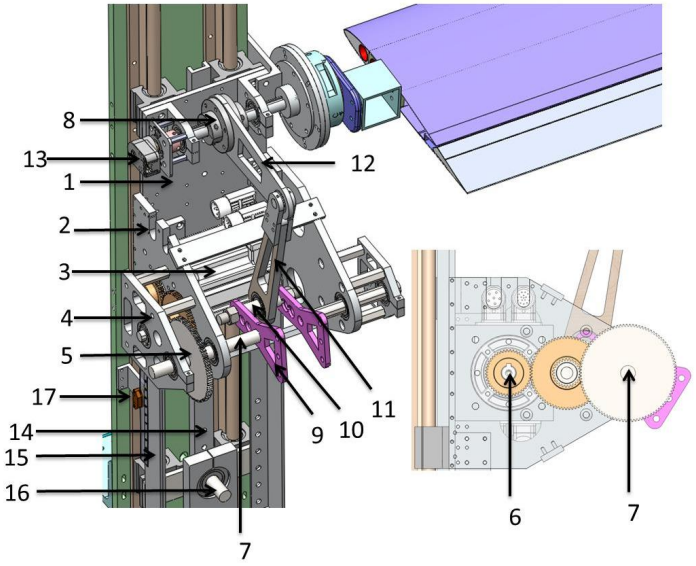

Figure 13: Pitch Module detailed view. Major components: 1.Back plate, 2.Wall, 3.Pitch actuator, 4.Mini wall, 5.Gearbox, 6.Motor shaft, 7.Drive shaft, 8.Wing shaft, 9.Crank. 10.Drive pin, 11.Connecting rod, 12.Wing bar, 13.Spine, 14.Extension channel, 15.Plunge encoder

components of the pitch module. The modules shell includes the Back Plate and two Walls which house majority of the components. The Pitch Actuator is an MPP series 92mm size Parker® servo motor and is mounted to the outer wall and the back

plate. Also, connected to the walls via stand-offs, are mini-walls, which make space for a gearbox. Figure 13 also shows the detail of the gearbox. The drive generated at the Motor Shaft, goes through two stages of speed reduction via four steel gears proving a total gear ratio of 5.688 when it reaches Drive Shaft.

The wing shaft sub assembly interfaces with the wing balance subassembly and is supported via bearings in two L-brackets connected to the back plate. A four bar mechanism, employed between the drive shaft and the wing shaft includes a set of two cranks (which divide the drive shaft in two), a drive pin, a connecting rod, and a wing bar.

In the constant rpm mode, the pitch amplitude is governed by the offset distance between drive pin and the drive shaft. The drive pin may be fitted at various locations inside the two cranks for various pitch amplitudes. The frequency is same as the rpm of the drive shaft. In the direct drive mode, the amplitude and frequency are prescribed for each oscillation separately. At the end of the wing shaft, an optical pitch encoder measures the instantaneous angular position of the wing. Since the wing shaft pass through two bearings in each pitch module, there is a capability for supporting a cantilevered wing. This feature opens up the possibility of studying flexible wings and finite span aerodynamics.

The pitch module extends via its spine and two extension channels towards the plunge interface pin which is connected to the plunge connecting rod via a bearing. The plunge interface pin may be mounted at various locations on the extension channels for various mean plunge locations. This may be used to study the effect of proximity to ground on unsteady aerodynamic loads. Also shown are the pitch encoder which measures the rotation of wing shaft with respect to the optical plunge encoder which measures the displacement of the pitch module with respect to the frame.

3.2.2 Plunge Mechanism

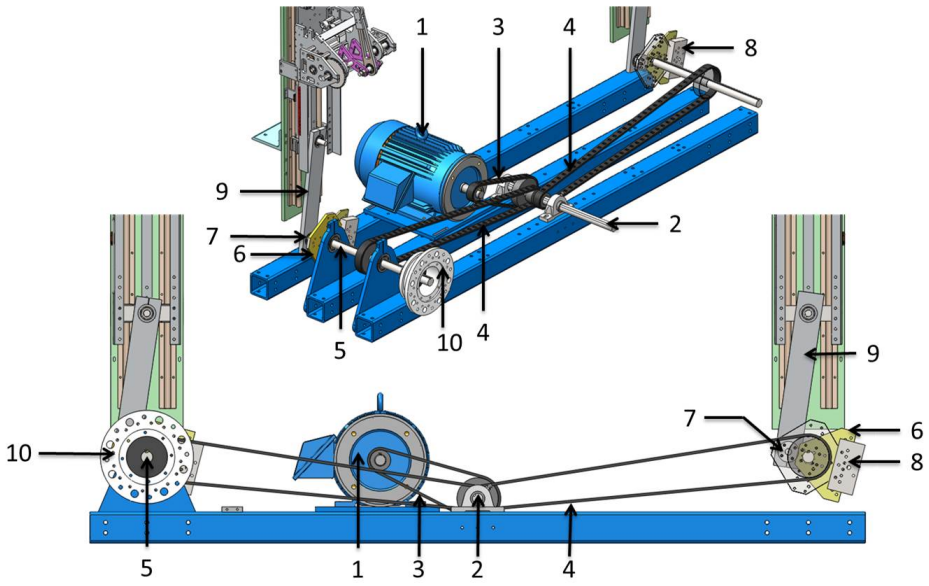

Figure 14: Plunge mechanism 1. Plunge motor, 2. Main drive shaft, 3. Primary belt drive, 4. Secondary belt drive, 5. Plunge drive shaft, 6. Plunge crank wheel, 7. Plunge crank pin, 8. Counterweight, 9. Plunge connecting rod, 10. Flywheel

Figure 14 shows two views of the plunge mechanism. On the top is the isometric view and the bottom part shows a front view. Although the port and starboard halves of the mechanism are largely identical, note that some components are intentionally hidden and some are made transparent on the starboard side of the mechanism in order to make internal parts visible. All components of the plunge mechanism are supported on the three steel square tubes bolted down to the base of the test section keeping the whole setup portable.

The Plunge mechanism assembly is responsible for providing an oscillating plunge drive to the two pitch modules which are otherwise free to slide on the vertical rails

under the force of gravity. The drive is generated by a single 5 hp 480V 3-phase AC motor called the Plunge Motor sitting on top of an aluminum plate, at 1 foot offset from the centerline of the test section on the port side. The motor drives the main drive shaft located at the centerline of the test section via a primary belt drive. The speed reduction which is the ratio of teeth on the driver pulley on the motor (28) and the driven pulley on the main drive shaft (56) is . Two secondary belt drives split the drive into two halves and drive two plunge drive shafts using identical belts and set of driver (27 teeth) and driven pulleys (56 teeth). The total speed reduction (and hence torque multiplication) achieved from the motor to each of the plunge drive shafts is 4.148.

At the end of each plunge drive shaft is a plunge crank wheel which has a series of mounting locations for the plunge crank pin and the counterweights. The normal distance between the plunge crank pin and the plunge drive shaft translates into plunge amplitude. The current settings allow plunge amplitude choices to 0.5, 1, 1.5, 2, 2.5 and 2.75 inches. By redesigning the plunge crank wheel accordingly, any custom plunge amplitude may be achieved below 4 inches before the motion profile departs considerably from being sinusoidal. As the plunge amplitude is varied, the gravity counterweight also needs to be adjusted in amount and/or location so that the moment due to the weight of plunge modules is balanced by the moment due to the counterweights. Finally, the plunge connecting rod connects the plunge crank pin to the interface pin on the each pitch module completing the slider crank mechanism. As the rotational motion of plunge drive shafts is converted into oscillating sliding motion of the plunge modules, the rapid accelerations cause immense loads on the driving mechanism and addition of inertia on the plunge drive shafts helps smooth out the motion. Thus, a custom flywheel at the end of the plunge drive shaft is employed. This flywheel has mounting holes for more weight attachments that may

be needed for various plunge amplitudes or frequencies. The plunge mode operates at constant rpm which results in a periodic oscillations of the wing. However, the rpm may be ramped from zero to a prescribed value at any rate which provides the feature of frequency ramp in plunge mode.

3.2.3 Wing Assembly

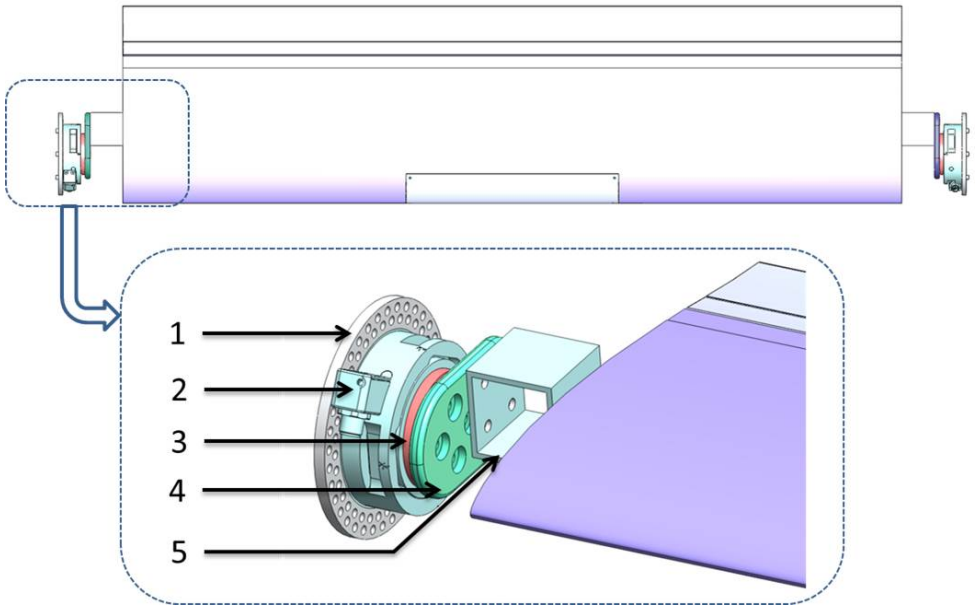

Figure 15: Wing balance sub-assembly. 1. AOA Plate, 2. Balance, 3. Balance interface plate, 4. Offset plate, 5. Wing mount tube

Figure 15 shows a view of the wing balance sub-assembly containing the wing, the port balance, starboard balance and the various attachments. Also, detail of port side of the sub-assembly is shown. AOA plate is the interface between the wing balance sub-assembly and the pitch module and is responsible for setting up mean pitch angle. It contains two series of holes at different radii offset by 5°. Any two holes in a series are 10°apart. This allow for any mean pitch angle between 0°to

360°with an interval of 5°. Any other angle may be reached by replacing this plate accordingly. Balance is an ATI® Delta 6-component load-cell which may measure three forces and three moments. The two balances mounted on two sides of the wing work in conjunction and their measurements are combined to generate the total forces in the normal and axial direction and the pitching moment. These load components are measured in balance frames and are later transformed into inertial frame of reference. Balance interface plate provides proper separation between the balance and the offset plate and is necessary for accurate measurements. Offset plate governs the location of pitch axis. In current experiments, it is designed to let the pitch axis pass through quarter chord location, but it may be designed to allow for pitching anywhere between the leading edge and mid chord location of the wing. Vertical offsets of up to an inch may also be designed for. Wing mount tube is a square tube which interfaces with the wing and also allows for the space for bolts on both sides. All the above components except the balance are made from aluminum.

3.2.4 Sensor Suite and Actuators

The pitch and plunge motors are driven by a Parker motion controller which accepts the motion input from a desktop computer via ethernet. A suite of sensors and National Instruments data acquisition system provide all necessary measurements pertaining to position, accelerations and loads. There is redundancy in motion information which is also useful for validation. These sensors are also used to identify system parameters during special maneuvers as described later chapters.

3.3 PPDS as Gust Generator

The above sections describe the PPDS as a standalone unsteady aerodynamics test apparatus. Some aspects of this research including the separation of inertial and gravity loads under dynamic environments to extract aerodynamic loads were

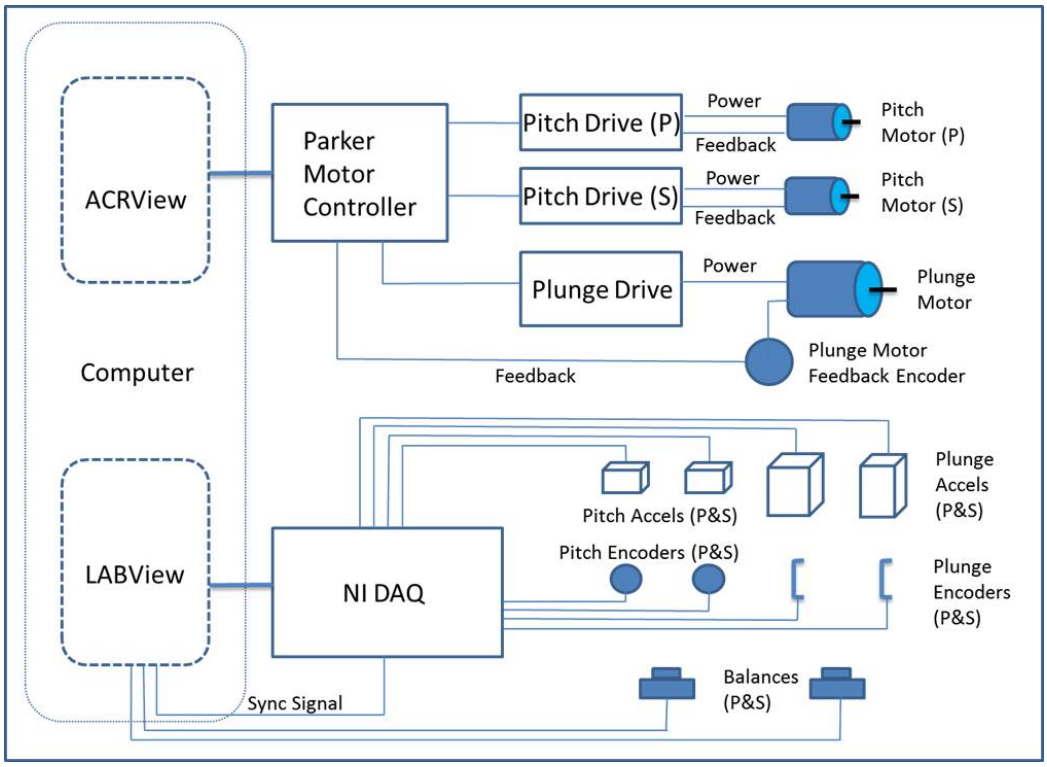

Figure 16: Schematic of PPDS actuation and data acquisition map

perfected on PPDS before those techniques were used in free aeroelastic experiments.

The motion of a wing causes the wake to become unsteady. This unsteadiness in bound circulation and shed vorticity also affects the nearby flow field downstream of the wing. Since PPDS is located upstream of the test wing, a pitch oscillation of PPDS wing causes an unsteady freestream for test wing. The plunge mode is only used to locate the PPDS wing vertically with respect to the test wing. The gust wing (PPDS wing) has been vertically located half chord below the gust sniffer and test wing such that both wings are away from the walls but the wake from gust wing does not directly impinge on the test wing while still providing an angularity in the flow. Since custom maneuvers are required to generate a gust field with high bandwidth, the pitch motion in PPDS is driven in the direct mode, i.e. the motor shaft oscillates

causing the wing shaft to oscillate.

3.4 Gust Sniffer

As gust generator oscillates the gust wing as commanded, a downwash field is formed downstream due to the variation of bound vorticity on the wing and free vortices in the wake. The angularity induced in the flow field is sufficient to cause appreciable change in wing effective angle of attack for the test wing. To sense the gusts generated by the wake of gust wing, a sensor has been developed (Figure 17) using a channel hotwire probe mounted at nearly 45°to the flow. The exact angle if immaterial as long as the sensor is calibrated and used in the same orientation. It has been assumed that the flow vector only changes direction and not magnitude as it is disturbed by the gust generator.

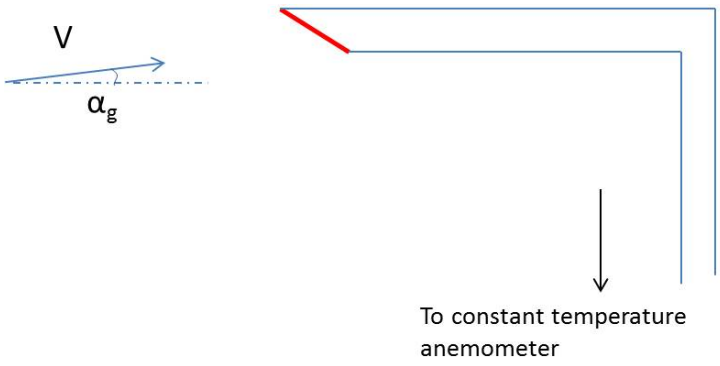

Figure 17: A sketch of Gust Sniffer

3.5 Nonlinear Aeroelastic Test Apparatus II

Nonlinear Aeroelastic Test Apparatus II is an elastic support system for a cantilevered wing providing nonlinear stiffness in pitch and linear stiffness in plunge. Figure 18 shows a model of NATA II system with wing. The nonlinear pitch stiff-

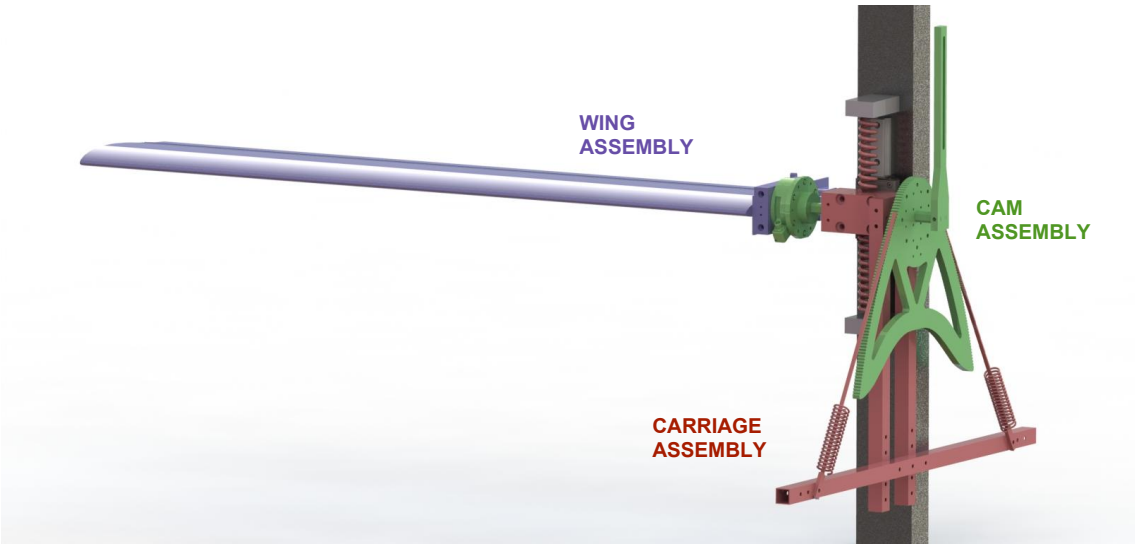

Figure 18: NATA II and Wing detailed drawing

ness is achieved using a combination of linear extension springs, a nonlinear cam and a timing belt. The nonlinear cam has grooves that match the belt. The main shaft supporting the wing passes through two ball bearings inside a solid aluminum bearing block. The bearing block is mounted to a linear slide system supported by linear springs. The pitch and plunge stiffness may be adjusted by changing the type of springs used. The wing location with respect to pitch axis may also be adjusted. The wing center of gravity location may be controlled by a sliding counterweight in the chord-wise direction. NATA II has a host of sensors including multi-component load cell for measuring lift and pitching moment, optical encoders for position and accelerometers for measuring accelerations. These sensors provide motion and load data which is then used to identify system parameters such as wing inertial parameters, support stiffness and damping etc. The NATA II wing is equipped with a full span control surface which is driven by a servo motor. The flap deflection is

measured by an optical encoder.

3.6 Complete Setup

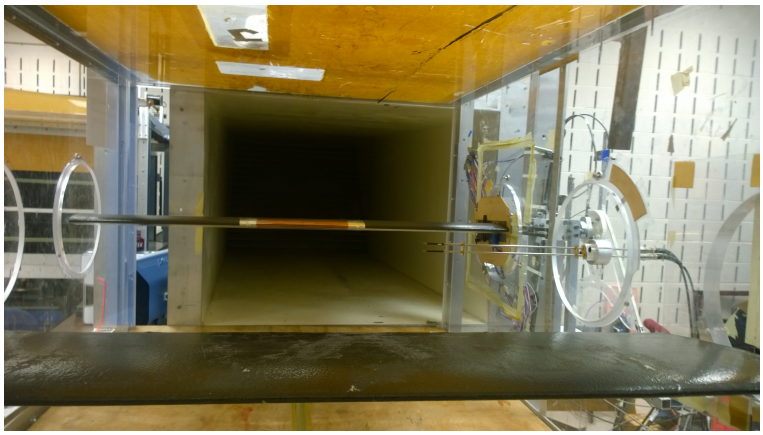

Figure 19: Front View from inside the test section

Figure 20: Side View of the experimental setup

Figure 19 shows a picture of the setup as seen from a inside test section looking downstream. The freestream first encounters the gust wing (in foreground), and

after being deflected hits the sniffer where the flow angularity is measured. The flow with angularity then passes over the NATA II wing which responds to the gust. For studies not involving the gust, the gust wing on PPDS is held at zero angle of attack. Figure 20 shows the side view of the experimental setup. It may be seen that the gust wing has been located at a vertical offset from the gust sniffer and the test wing. This prevents the wake from gust wing from directly impinging on the test wing. however, the flow is deflected in accordance with the vorticity induced by the gust wing.

4. AEROELASTIC SYSTEM EQUATIONS AND IDENTIFICATION

This chapter lays the analytical foundation of this research. First, the aeroelastic equations of motion of a typical two dimensional wing section are presented. These equations are then modified to represent wing as mounted on NATA II. The system parameters include inertial, damping, stiffness and aerodynamic parameters and are experimentally determined from experimental data by performing specific maneuvers. This approach of experimentally determining system parameters through systematic simplified maneuvers is more physics based as compared to previous attempts which was primarily based on greybox or blackbox models [17]. Once the wing inertial and aerodynamic parameters are determined, the unsteady aerodynamic loads may be extracted from the experimental measurements. Similarly, once the mount stiffness, damping and inertial parameters have been identified, the structural model in pitch and plunge is validated with experiments. These steps provide an intermediate level of validation of component models before they are combined to predict aeroelastic response.

4.1 Equations of motion for NATA II wing

Figure 21 represents the Computer Aided Design (CAD) model of test wing mounted on NATA II. Equations 27 and 28 represent an ideal aeroelastic system and will be modified to represent the experimental system. These modifications pertain to the mass and inertia distribution of various components, structural nonlinearities, and damping loads. The total pitching mass, m_α, includes the wing assembly mass, m_w, and pitch cam assembly mass, m_{cam}. Similarly, the total pitching moment of inertia includes that of the wing assembly and the cam assembly. The plunging mass, m_h includes the mass of the wing assembly, the pitch cam assembly, and the plunge

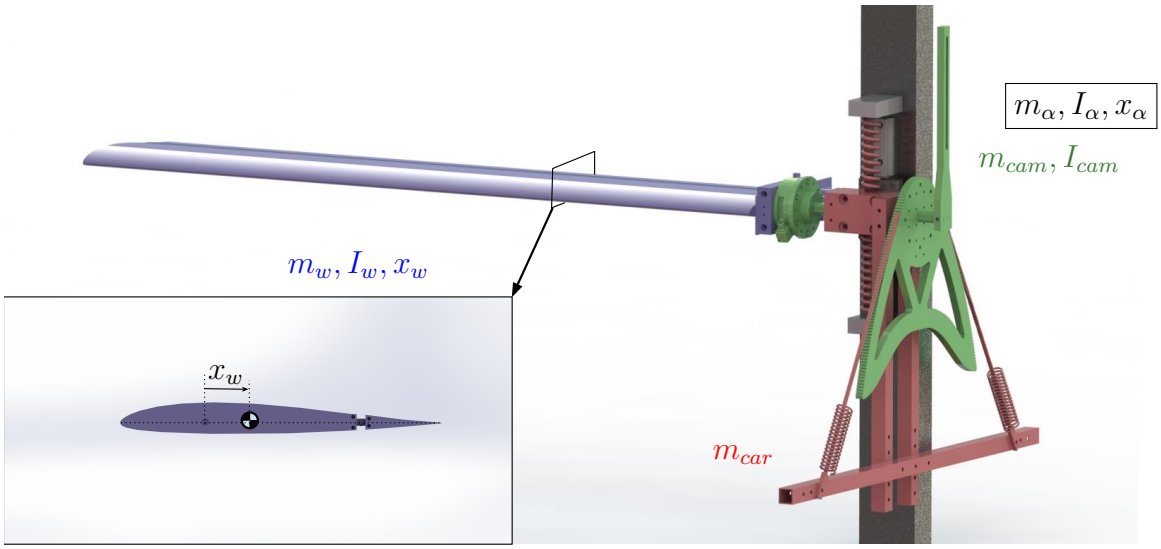

Figure 21: Wing mounted on NATA

carriage assembly. These mass and inertia relations may be written as

$$m_\alpha = m_w + m_{cam} \tag{29}$$

$$I_\alpha = I_w + I_{cam} \tag{30}$$

$$m_h = m_\alpha + m_{car} \tag{31}$$

The load term related to linear pitch stiffness, $k_\alpha \alpha$, is replaced by the torsional spring load, $F_{k,\alpha}$ which may represent a linear or a nonlinear spring. As shown later in this chapter, the nonlinearity in pitch stiffness is captured by a 4th order polynomial. Plunge stiffness term is unchanged since NATA II has linear plunge stiffness by design similar to the idealized aeroelastic system. A viscous pitch damping load term has been added to the structural model through the term $c_\alpha \dot{\alpha}$. The plunge damping force, $F_{c,h}$ is introduced which may represent either viscous damping or Coulomb

damping. The modified equations of motion are

$$m_h\ddot{h} + m_\alpha x_\alpha \ddot{\alpha} + F_{c,h} + k_h h = -L \tag{32}$$

$$I_t\ddot{\alpha} + m_\alpha x_\alpha \ddot{h} + c_\alpha \dot{\alpha} + F_{k,\alpha} = M \tag{33}$$

The center of gravity of wing, x_w, the center of gravity of cam assembly, x_{cam}, and the center of gravity of total pitching mass (consisting of the wing assembly and cam assembly), x_α, are related as

$$x_\alpha = \frac{m_w x_w + m_{cam} x_{cam}}{m_\alpha} \tag{34}$$

The cam assembly is designed with a symmetric mass distribution about the pitch axis.

$$x_{cam} = 0 \tag{35}$$

Hence,

$$m_\alpha x_\alpha = m_w x_w \tag{36}$$

Using Equation 36 and assuming nonlinear pitch stiffness, the final equations of motion assume the form

$$m_h\ddot{h} + m_w x_w \ddot{\alpha} + F_{c,h} + k_h h = -L \tag{37}$$

$$I_\alpha\ddot{\alpha} + m_w x_w \ddot{h} + c_\alpha \dot{\alpha} + F_{k,\alpha} = M \tag{38}$$

In Equations 37 and 38 above, the following definitions are applicable

$$F_{c,h} = \begin{cases} c_h \dot{h}, & \text{for viscous plunge damping} \\ F_d sign(\dot{h}), & \text{for Coulomb plunge damping} \end{cases} \tag{39}$$

$$F_{k,\alpha} = \begin{cases} k_\alpha \alpha, & \text{for linear pitch stiffness} \\ k_1\alpha + k_2\alpha^2 + k_3\alpha^3 + k_4\alpha^4, & \text{for nonlinear pitch stiffness} \end{cases} \tag{40}$$

L and M are chosen depending on the type of aerodynamic model, which are presented in section 2.1. The aerodynamic parameters to be identified are $C_{L,\alpha}$ and $C_{M,\alpha}$.

4.2 System Identification

This section details the various system identification process performed to estimate system parameters which appear in equations 37 and 38. In prior research [17], the system parameters for NATA were determined using an input out based greybox model. As a result, complete understanding of the observed aeroelastic behavior could not be accurately ascertained. In some cases, the identification process generated unrealistic values of system parameters. In the current research, physics based simple maneuvers are conducted, and measured quantities are used to identify each type of parameter. The second generation hardware (NATA II) is equipped with a host of sensors and the redundancy in the data helps with validation and verification. The key sensors utilized for identification are the multi-component load cell (for loads) and the optical encoders (for acceleration). The unknown system parameters are listed in Table 2.

Table 2: Parameters to be estimated from System Identification techniques

Wing inertial parameters	m_w, I_w, x_w
Wing aerodynamic parameters	$C_{L,\alpha}, C_{M,\alpha}$
Support inertial parameters	m_h, I_α
Support stiffness parameters	$k_1, k_2, k_3, k_4, k_\alpha, k_h$
Support damping parameters	c_α, c_h, F_d

4.2.1 Wing inertial parameters

Wing inertial parameters include the wing mass (m_w), wing moment of inertia (I_w) about the pitch axis, and the location of center of gravity of the wing with respect to pitch axis(x_w). Each of these parameters may be estimated using measurements of loads and accelerations under specific maneuvers in wind off conditions as described below. It is assumed that aerodynamic loads generated due to motion in still air are negligible as compared to the inertial loads generated. Hence, wind-off maneuvers only produce inertial loads which are directly measured by the load cell. So, for the estimation of wing inertial parameters,

$$U = 0, L = 0, M = 0; \tag{41}$$

The wing mass and location of center of gravity from elastic axis may be estimated in a plunge only maneuver ($\alpha, \dot{\alpha}, \ddot{\alpha} = 0$), while the wing is locked in pitch in wind off conditions. As may be seen in Figure 21, the pitch assembly includes a load measuring balance, which while pitching and plunging with the wing assembly, also measures the loads passing through it. Thus, Equation 37 may be examined at the location of load cell where we identify the measured normal force, F_y such that,

$$(m_{car} + m_{cam})\ddot{h} + sgn(\dot{h})F_d + k_h h = F_y \tag{42}$$

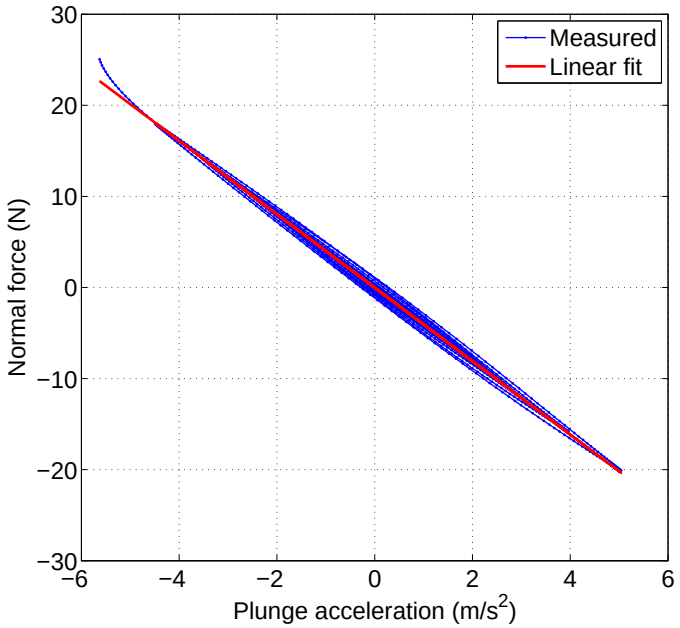

Figure 22: Identification of wing mass as the slope of linear fit between measured normal force and plunge acceleration. $m_w = 4.03\ kg$

$$m_w \ddot{h} = -F_y \tag{43}$$

Figure 22 shows the plot between the measured normal force and plunge acceleration. It can be seen that the trend is strictly linear. As suggested by Equation 43, the negative of the slope of linear fit gives the wing mass. The moment from the inertial loads acting on the center of gravity is measured by the load cell as T_z such that

$$m_w x_w \ddot{h} = T_z \tag{44}$$

Combining Equations 43 and 45

$$-F_y x_w = T_z \tag{45}$$

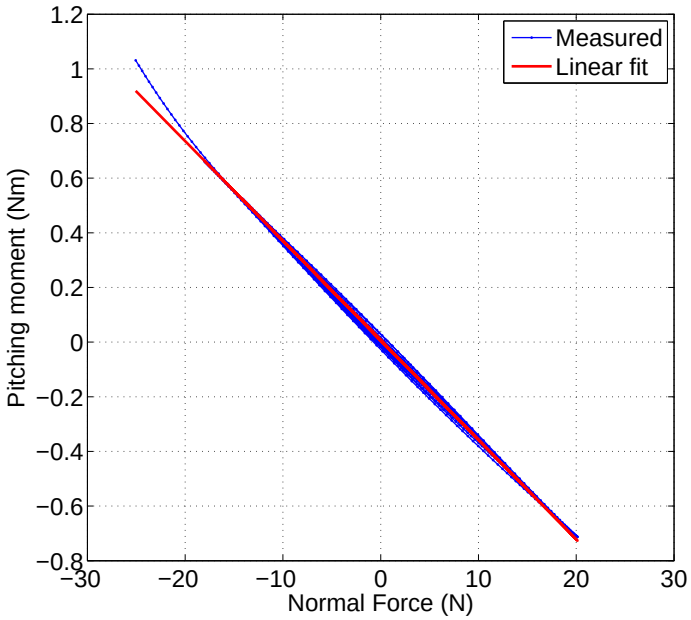

Figure 23: Identification of wing c.g. location as slope of linear fit between measured pitching moment and normal force. $x_w = 0.0364\ m$

Thus, x_w may be found as the slope of negative of slope of measured T_z vs. F_y curve in a plunge only maneuver. The measured data and linear fit are shown in Figure 23. Similarly, the wing moment of inertia may be determined during a pitch only maneuver in wind off conditions.Thus, Equation 38 may be examined at the location of load cell.

$$I_{cam}\ddot{\alpha} + c_\alpha\dot{\alpha} + k_1\alpha + k_1\alpha^2 + k_1\alpha^3 + k_4\alpha^4 = T_z \tag{46}$$

$$I_w\ddot{\alpha} = -T_z \tag{47}$$

The measured values of pitch acceleration and pitching moment are plotted in Figure 24. The negative of slope of linear fit gives the wing moment of inertia.The identified wing inertial parameters are included in the complete list of all parameters

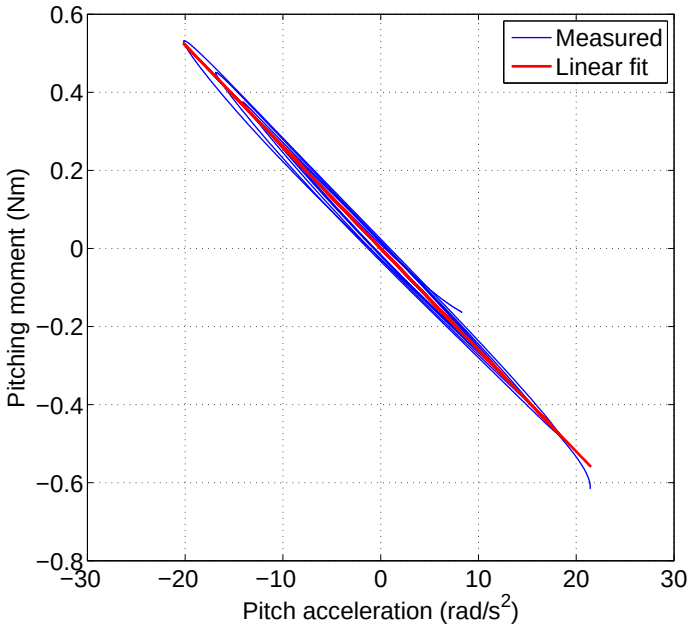

Figure 24: Identification of wing moment of inertia as slope of linear fit between measured pitching moment and pitch acceleration. $I_w = 0.0260\ kg\ m^2$

shown in Table 3.

4.2.2 Wing aerodynamic parameters

The aerodynamic parameters that appear in Equations 37 and 38 include the lift curve slope C_{L_α}, and moment curve slope, C_{M_α}, and are determined as aerodynamic loads are measured during a static test. Figure 25 shows these measurements. It is noted that because the pitch axis is at quarter chord point, the moment curve slope has a small value of 0.183. The lift curve slope (5.45) is lower than the expected value of 2π. This difference is attributed to two reasons. the wing root has control surface horns and push rods cause some flow separation at the root. Secondly the tip of the wing does not touch the wind tunnel wall to allow for the wing to plunge. This causes flow to leak through the clearance and this effectively reduces the wing

lift curve slope.

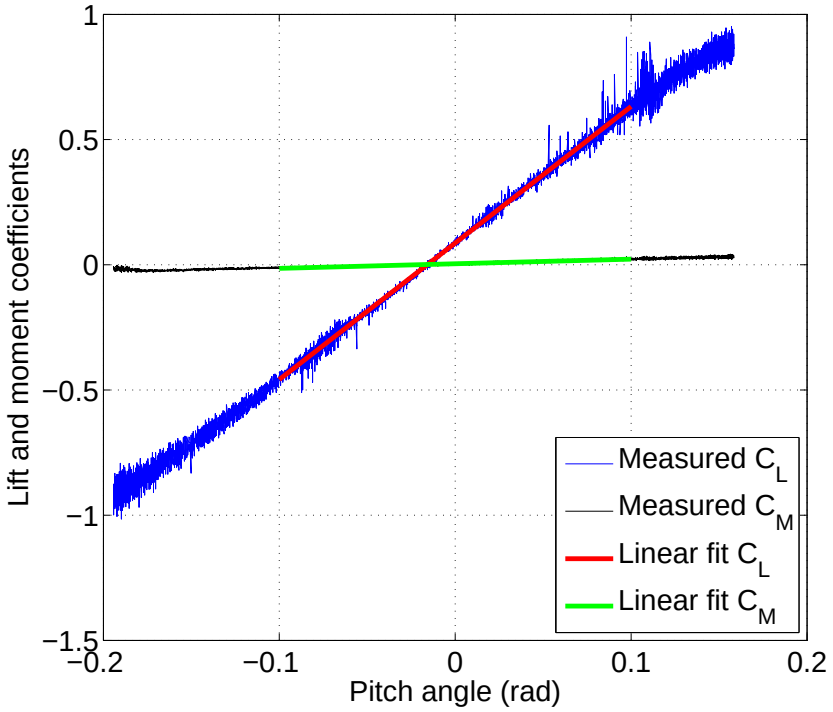

Figure 25: Identification of wing aerodynamic parameters. $C_{L_\alpha} = 5.45$ and $C_{M_\alpha} = 0.183$

4.2.3 Mount stiffness parameters

The nonlinear pitch and linear plunge stiffness parameters appearing in Equations 37 and 38 may be identified using the displacement and load measurements. For plunge stiffness measurement, the wing is locked in pitch and is displaced at the wing root in both positive and negative direction. Since there is no motion, $\dot{h}, \ddot{h} = 0$ and Equation 42 is simplified to

$$k_h h = F_y \tag{48}$$

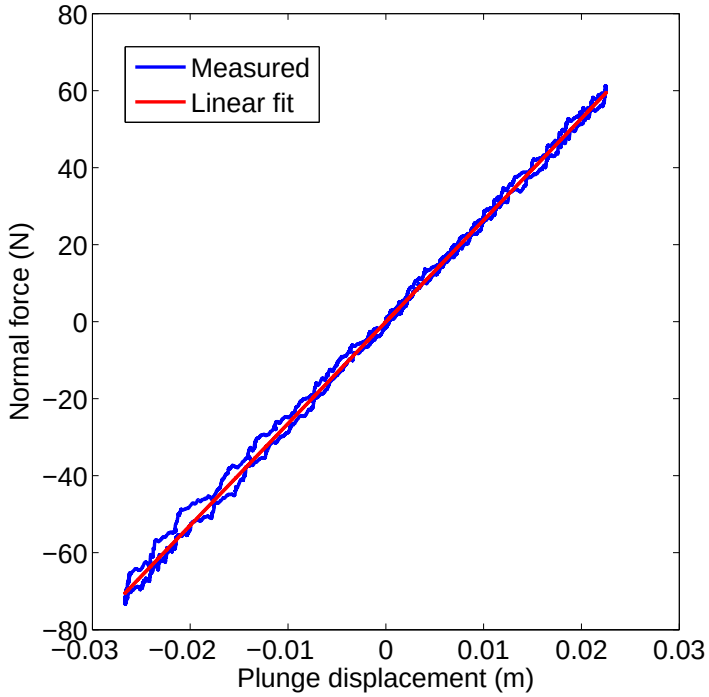

Figure 26: Identification of plunge stiffness. $k_h = 2641.8\ N/m$

F_y and h are directly measured and k_h is the slope of linear fit between the measured quantities. Similarly, the pitch stiffness is determined by plotting measured pitching moment and angular displacement in a pitch only maneuver. The wing is locked in plunge and the wing is manually twisted at the root such that $\dot{\alpha}, \ddot{\alpha} = 0$. The applied moment is transmitted through the load cell and is measured in the process. Equation 46 is rewritten as

$$k_1\alpha + k_2\alpha^2 + k_3\alpha^3 + k_4\alpha^4 = T_z \tag{49}$$

The constants k_1 through k_4 are determined through a fourth order polynomial fit between measured quantities T_z and α. Figure 27 shows the plots for identification of

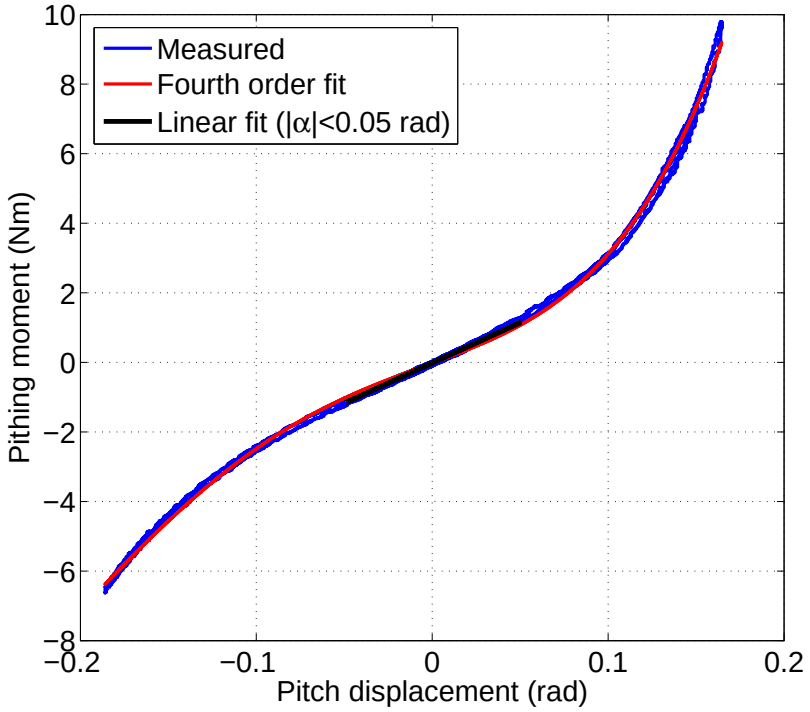

Figure 27: Identification of pitch stiffness. k_4=2302.1 Nm/rad, k_3=933.5 Nm/rad^2, k_2=10.6 Nm/rad^3, k_1=18.7 N/m

plunge and pitch stiffness. It is seen that the pitch stiffness is inherently nonlinear. However, for small pitch angle range ($|\alpha| < 0.05$ rad), the pitch stiffness may be linearized. This is important information for two reasons. First, the flutter speed prediction may be made from linear analysis, and secondly, the linear pitch stiffness is used in identification of total pitch inertia as shown in a later section. The values of nonlinear pitch stiffness (polynomial constants k_1 through k_4), linear plunge stiffness (k_h) and the linearized pitch stiffness ($k_{\alpha,l}$) are listed in Table 3.

4.2.4 Mount damping parameters

The pitch and plunge motions are made possible with the help of ball bearings. These ball bearings have frictional effects which are modeled with a damping model

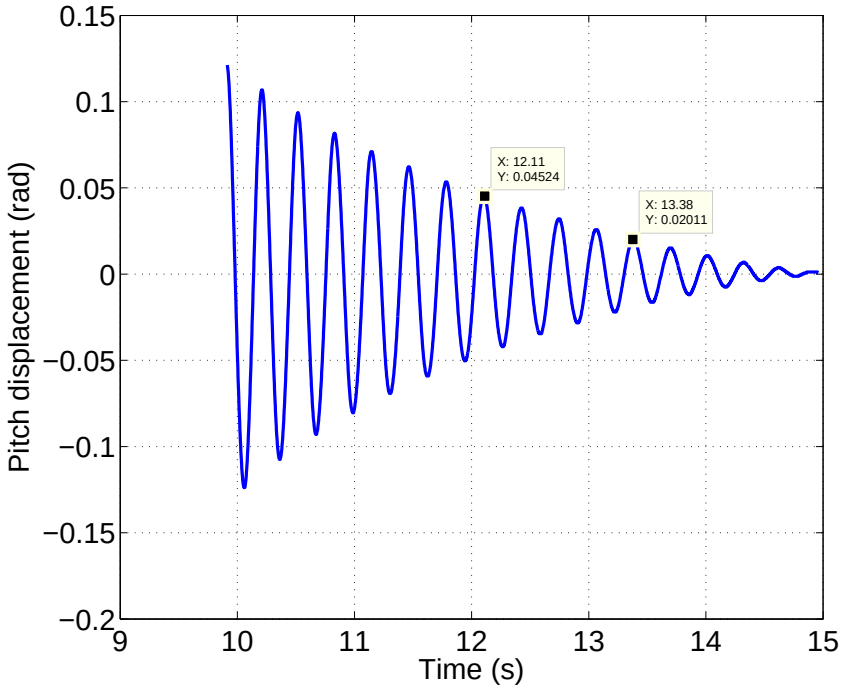

Figure 28: Identification of pitch damping (viscous model). $\zeta_\alpha = 0.0322$

in the equations of motion. The rotational ball bearings tend to have small damping may be characterized as viscous type. On the other hand, linear bearings are known to exhibit higher values of damping and it is usual to observe Coulomb type (dry friction) damping behavior. In reality, the damping behavior is a mix of different types of damping but, to simplify, one type of model is employed to identify the damping. Also, pitch and plunge damping are identified separately by locking the other type of motion during the identification maneuver.

The damped pitch response, generated as the wing is disturbed in pitch, is shown in Figure 28 . This behavior is best represented with a viscous damping model since the decay is almost exponential. Thus traditional logarithmic decrement (log-dec) method may be used to estimate the viscous damping ratio. It should be noted pitch

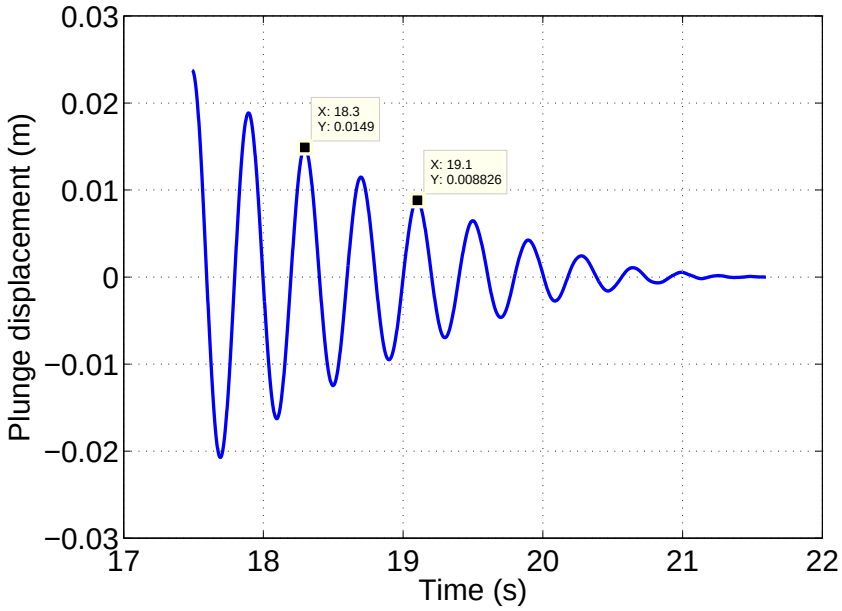

Figure 29: Identification of plunge damping (Coulomb case: $F_d = 2.0 \pm 0.5\ N$, Viscous case: $\zeta_h = 0.0416$)

mode is inherently nonlinear due to the cam and this method is only applicable for linear systems, so the linearized pitch stiffness is used and only small amplitudes are considered. Using the log-dec approach described in Section 2, the pitch damping ratio is found using the coordinates of the two data points highlighted in Figure 28. The pitching damping is expressed as damping ratio, ζ_α and the value is found to be 0.0322.

Figure 29 shows the system behavior in plunge generated as the system is releases from a plunge initial condition while the pitch mode is locked. Unlike the pitch response, the linear bearings in plunge mode show a behavior closer to Coulomb damping since the decay is closer to linear than exponential. This is typical for linear sliding motion. The assumption of nonlinear Coulomb damping explains a very important nonlinear system behavior observed in experiments as demonstrated

later. Additionally, plunge damping is also modeled as purely viscous damping using similar approach as pitch damping. This allows us to explore the effects of nonlinear damping Vs. linear damping on aeroelastic response. It also enables study of effects of structural damping on flutter speed prediction using linear techniques as demonstrated Section 6. Assuming Coulomb damping, the procedure mentioned in Section 2 (Figure 9) has been followed and the value of damping force, F_d has been found to be 2.0 N.

It has been found that an important aspect of nonlinear aeroelastic response, the LCO onset speed is sensitive to the amount of nonlinear damping. The identification of Coulomb damping depends on the choice of data points picked for identification. Thus a range of Coulomb damping values has been found to allow for the variance in identified values. The two extreme values of Coulomb damping force considered are 2.5 N and 1.5 N.

4.2.5 Mount inertial parameters

The mount inertial parameters include plunge mass, m_h, and the total pitch inertia, I_α. The plunge mass is directly measured using a balance and the value is found to be 10.25 kg. Total pitch inertia cannot be directly measured and hence must be identified from experiments. Since pitch damping is small, it is assumed that damped pitch frequency is nearly equal to the natural frequency (ω_α). Using the time coordinates of data points in Figure 28, ω_α may be related to pitch inertia such that

$$I_\alpha = \frac{k_{\alpha,l}}{\omega_\alpha^2} \tag{50}$$

It was found that the aeroelastic response, especially the LCO amplitude was sensitive to the value of total pitch inertia. The variance in determination of total pitch inertia was found to be was found to be of the order of 0.0025 $kg\ m^2$ while the value

of total pitch inertia itself was found to be 0.0587 $kg\ m^2$. It may be noted that this value of total pitch inertia is higher than the value of wing inertia because it includes the inertia of other components such as wing shaft, cam, bearings etc.

In addition to the above system parameters, the geometric parameters include the wing chord, $c = 0.298\ m$, semi-chord, $b = \frac{c}{2} = 0.149\ m$ and wing span, $S = 1.206\ m$. All parameters identified above are listed in Table 3.

Table 3: Identified aeroelastic system parameters

Inertial	$m_w : 4.03\ kg \quad I_w : 0.0260\ kg\ m^2 \quad x_w : 0.0364\ m$ $m_h : 10.25\ kg \quad I_\alpha : 0.0587 \pm 0.0025\ kg\ m^2$
Stiffness	$k_4 : 2302.1\ Nm/rad \quad k_3 : 933.5\ Nm/rad^2 \quad k_2 : 10.6\ Nm/rad^3$ $k_1 : 18.7\ N/m \quad k_{\alpha,l} : 23.201\ N/m \quad k_h : 2641.8\ N/m$
Damping	$\zeta_\alpha : 0.0322 \quad \zeta_h : 0.0416 \quad F_d : 2.0 \pm 0.5\ N$
Aerodynamic	$C_{L_\alpha} : 5.45 \quad C_{M_\alpha} : 0.183$
Geometric	$b : 0.149\ m \quad S : 1.206\ m$

5. VALIDATION OF COMPONENT MODELS

In Section 4, the system parameters were identified. Before these parameters are used for solving aeroelastic equations of motion (Equations 37 and 38), the component models including the aerodynamic models and structural model are validated with experiments. These findings are reported in this section.

5.1 Validation of Aerodynamic Models

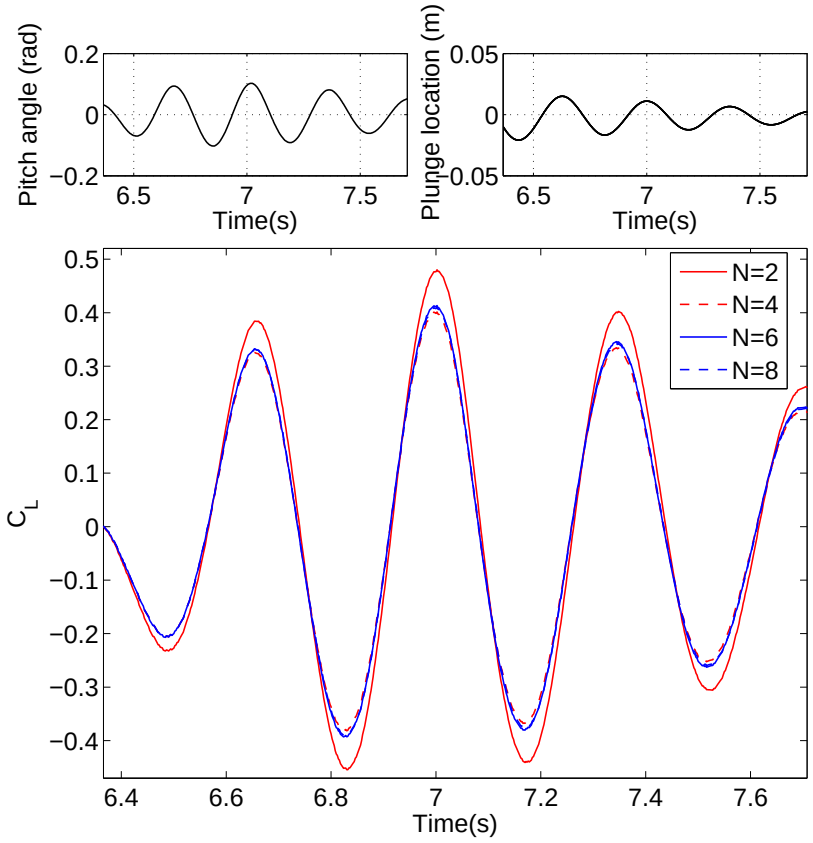

Figure 30: Determination of optimum number of lag states for Peter's model for C_L

The unsteady lift and moment are represented by various models as described in Section 2. Peters model is widely used unsteady aerodynamic model given its ability to account for high levels of unsteadiness ($k > 0.1$) and the ability to handle periodic as well as aperiodic motions of wings. Figure 30 shows the dependence of coeffocient of lift on number of lag states, N, chosen for the model. The maneuver is a combination of pitch and plunge at $U = 10\ m/s$. It is clear that the number of C_L begins to show invariance to number of lag states after $N = 4$. Typically, $N = 6$ is chosen as the optimum number of lag states and our findings support that.

Figure 31 presents the comparison of measured C_L with those predicted by various aerodynamic models during a combined pitch plunge maneuver at $U = 10\ m/s$. The pitch and plunge motion are also depicted in the figure. The total measured data (labeled 'measured total') shows a measurement of raw loads. This is simply the output from the load cell nondimensionalized by reference lift. The inertial loads arising due to the motion of the wing need to be identified and separated from these loads. An identification technique was developed for extraction of purely unsteady aerodynamic loads and is described in this paper [19]. The extracted aerodynamic loads from experiments are also plotted. Three models for lift have been presented. First, it may be seen that all models perform reasonably well when compared with experimental data. It is interesting to note while unsteady model overpredicts the lift coefficient while Peter's model (N=6) underpredicts the C_L when compared to experiments. For the development of aerelastic model, unsteady aerodynamic model has been picked as the candidate given its simplicity when compared with Peter's model. Figure 32 presents similar results for C_M. Here it may be seen that quasi-steady models does not capture the unsteady moment coefficient. The unsteady model and Peter's model best predict the evolution of pitching moment. In Section 6, the unsteady aerodynamic model has been chosen as the primary model. However

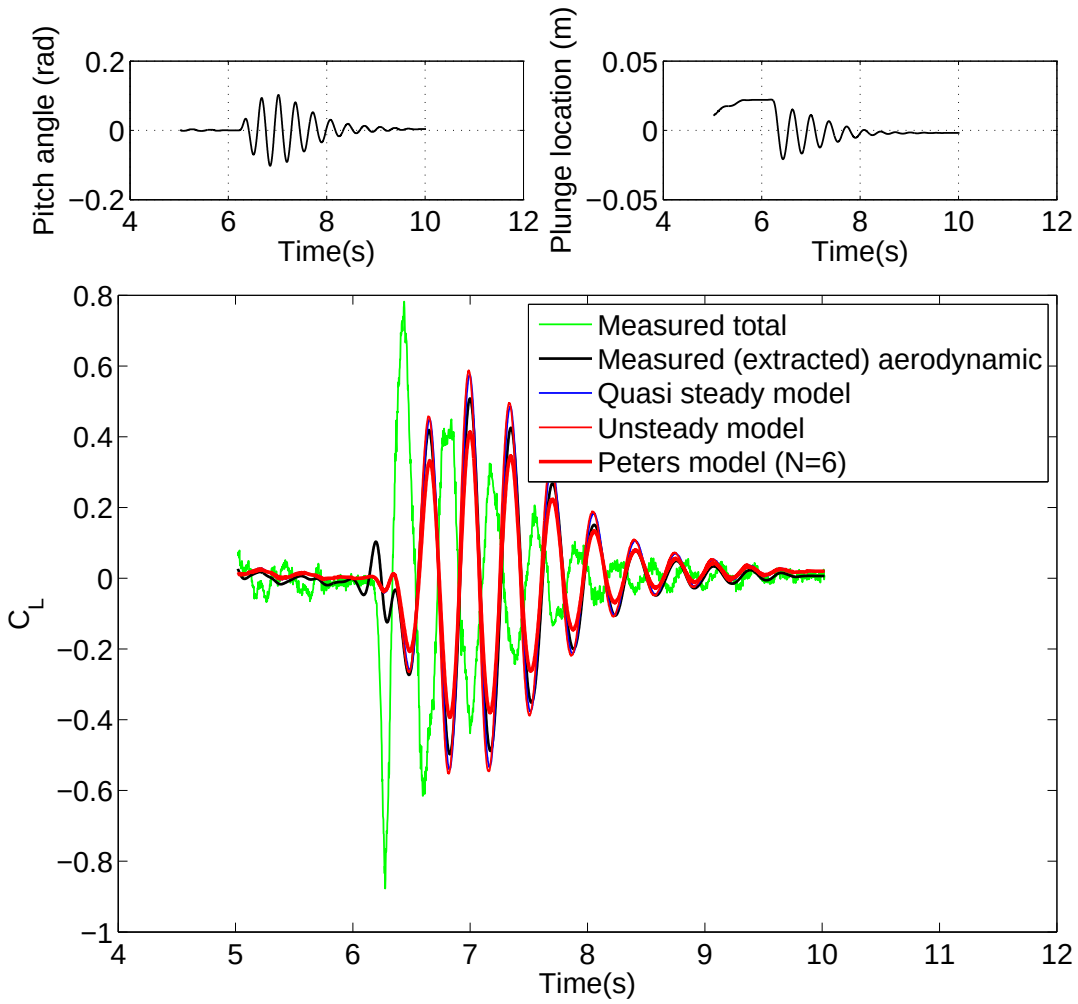

Figure 31: Comparison and Validation of aerodynamic models with experiments for C_L

Peter's model has also been used where appropriate.

5.2 Validation of structural model

The structural parameters identified in Section 4 are validated with experiments by simulating the response in pitch and plunge and comparing with experiments.

Figure 33 shows the comparison of experimentally measured pitch response to

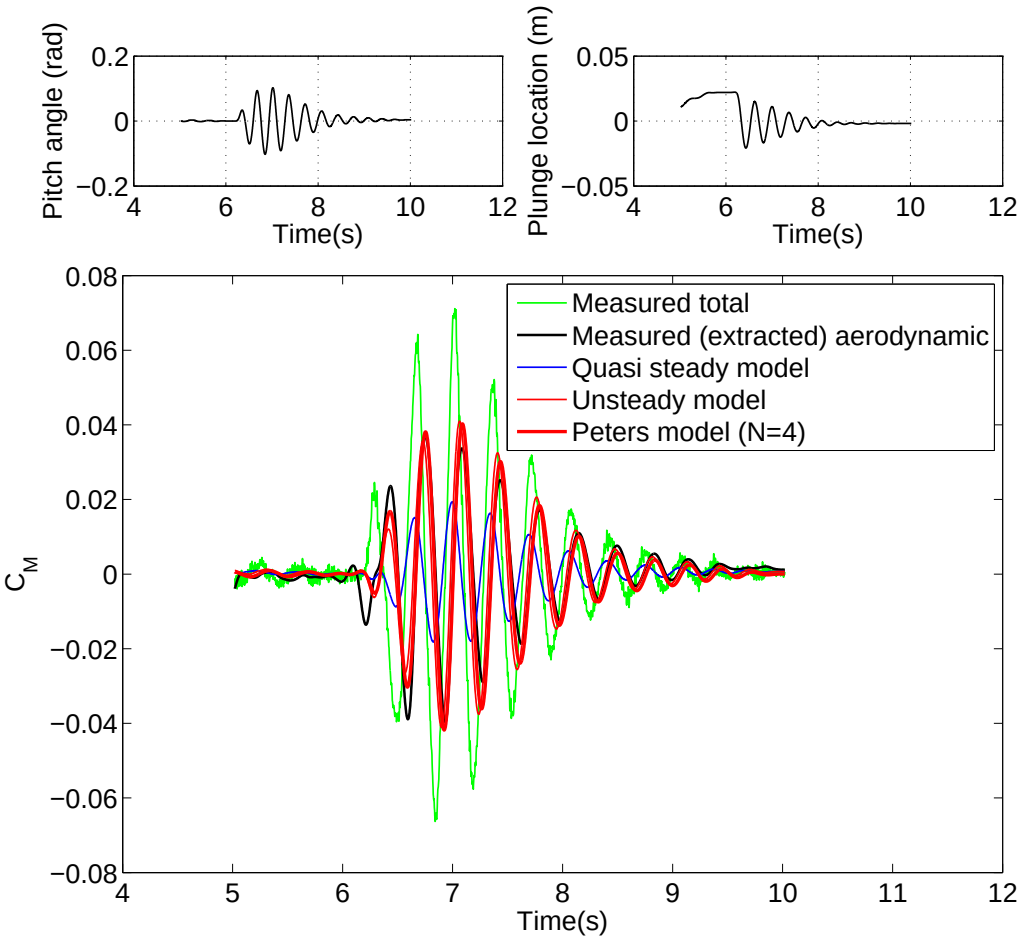

Figure 32: Comparison and Validation of aerodynamic models with experiments for C_M

the modeled pitch response assuming viscous damping. It is seen that the modeled pitch response matches the experimental response well but, towards the end where amplitudes are small, the modeled response continues the exponential decay while the measured response dies out quickly. This confirms the presence of a small level of Coulomb type damping in these bearings. For this study, we neglect the Coulomb damping behavior in the pitch mode. Figure 34 shows the comparison of the measured plunge response with predicted response damping models. It may be seen

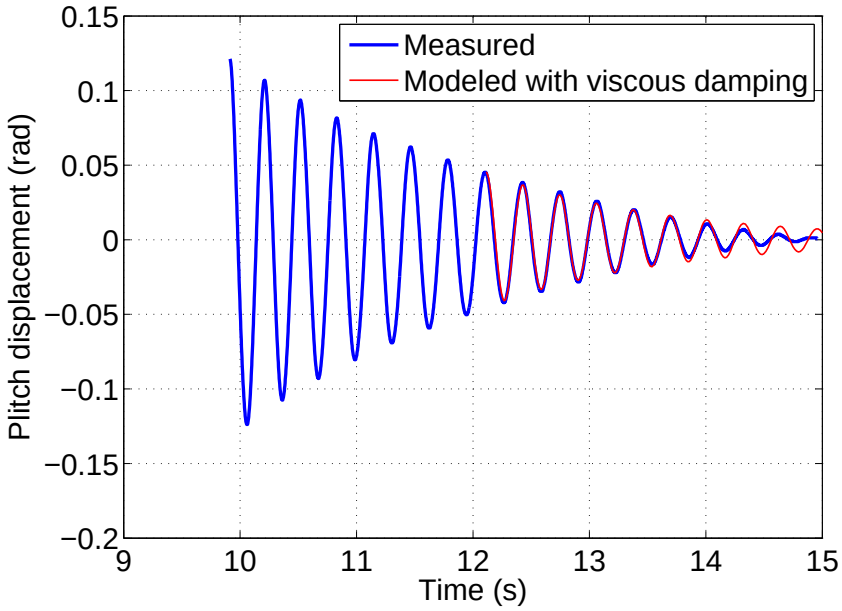

Figure 33: Validation of modeled pitch damping (viscous) with experiments

that using both models have their strengths and weaknesses. The Coulomb damping model appears to predict the overall time to equilibrium well while showing inaccuracy in predicting extreme displacements in earlier cycles. The viscous damping model predicts the first few cycles very well but cannot capture the sharp decay of response at small amplitudes. One of the objectives of this research is to compare the behavior of limit cycle oscillations of the wing in presence of nonlinear Coulomb damping as well as a more conventional linear viscous damping. At this stage, all parameters have been identified and component models have been validated. In the next section, the component models are combined and two predictive aeroelastic models are discussed.

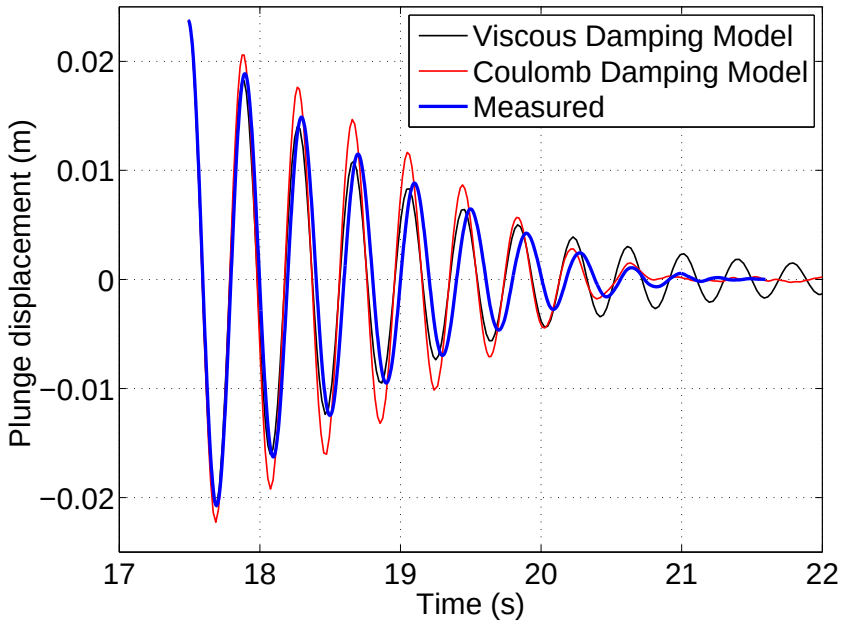

Figure 34: Validation of modeled plunge damping (viscous and Coulomb) with experiments

6. PREDICTIVE AEROELASTIC MODELS

The equations of motion presented as Equations 37 and 38 may now be solved since all the system parameters have been identified. These parameters are listed in Table 3. In the study of linear aeroelastic behavior, many analytical methods focus on predicting flutter speed. Below this critical speed, any disturbance will decay to equilibrium. At speeds closer to the flutter speed, the decay rate will be slower. Past the flutter speed, any disturbance will lead to growing oscillations with increasing amplitude. For a nonlinear system, the response might be bounded and the system may exhibit limit cycle oscillations(LCO).

The flutter boundary has been obtained by an eigen analysis of the linearized equations of motion using the p-method [2]. The effects of structural damping on flutter speed is also discussed. Herein, time domain aeroelastic response is obtained by integrating a state space model representation of the equations of motion under prescribed freestream and initial conditions.

6.1 Flutter Speed Prediction

Flutter is a a dynamic aeroelastic instability defined as divergent oscillation of the wing as wind speed exceeds a critical value, also called the flutter speed. For a typical wing section with linear stiffness in pitch and plunge and no structural damping, there is a critical value of wind speed below which the aerodynamic damping is positive. Above this speed, the aerodynamic damping is negative and the system exhibits divergent oscillations. In aircraft systems, such a behavior usually leads to catastrophic wing failure. Nonlinearities such as a hardening spring or aerodynamic stall give rise to conditions under which the response may be bounded. Such conditions are beyond the scope of eigenvalue analysis but the linearized system behavior

is of importance to the study of the nonlinear problem.

First in this chapter, the eigenvalue solution for a typical ideal aeroelastic system with the same characteristics as the one used by Hodges [2] is presented. This approach assumes a simple quasi-static aerodynamic model for illustration. After the solution technique is verified, the parameters are changed to the NATA II parameters to predict the flutter speed for the experimental system. It should be noted that the equations are linearized before eigenvalue solution is computed. Then, the effects of various aerodynamic models is explored. Lastly, the effect of viscous damping is studied.

6.1.1 Flutter speed of a typical section

The equations of motion of a typical wing section with an ideal lift curve slope of $C_{L,\alpha} = 2\pi$, mounted on a two degree-of-freedom linear aeroelastic mount are represented by equations 27 and 28.

The left hand side of these equations represent the structural loads and the right hand side represents the aerodynamic loads, namely the lift and pitching moment. First, let us consider a quasi-staic aerodynamic model based on the instantaneous pitch angle. According to this model, the lift and moment are given as Equations 1 and 2. The combined aeroelastic equations for a wing of unit span may be written as

$$m\ddot{h} + mx\ddot{\alpha} + k_h h = -2\pi\rho U^2 b\alpha \tag{51}$$

$$I\ddot{\alpha} + mx\ddot{h} + k_\alpha \alpha = 2\pi\rho U^2 b^2 \alpha(\frac{1}{2} + a) \tag{52}$$

A state vector x may be defined such that $x = [h\ \dot{h}\ \alpha\ \dot{\alpha}]^T$ such that $\dot{x} = [\dot{h}\ \ddot{h}\ \dot{\alpha}\ \ddot{\alpha}]^T$.

Thus Equations 51 and 52 may be cast in to the form $A\dot{x} = Bx$ as:

$$\underbrace{\begin{bmatrix} 1 & 0 & 0 & 0 \\ 0 & m & 0 & mxb \\ 0 & 0 & 1 & 0 \\ 0 & mxb & 0 & I \end{bmatrix}}_{A} \underbrace{\begin{bmatrix} \dot{h} \\ \ddot{h} \\ \dot{\alpha} \\ \ddot{\alpha} \end{bmatrix}}_{x} = \underbrace{\begin{bmatrix} 0 & 1 & 0 & 0 \\ -k_h & 0 & -2\pi\rho U^2 b^2 \alpha & 0 \\ 0 & 0 & 0 & 1 \\ 0 & 0 & -k_\alpha + 2\pi\rho U^2 b^2 \alpha(\frac{1}{2} + a) & 0 \end{bmatrix}}_{B} \underbrace{\begin{bmatrix} h \\ \dot{h} \\ \alpha \\ \dot{\alpha} \end{bmatrix}}_{\dot{x}} \tag{53}$$

For this case, the structural parameters of the system are chosen to match Hodges non-dimensional parameters as found in [2]. The eigenvalues of $A^{-1}B$ are given by the complex conjugate pairs $v_1 = \Gamma_1 \pm i\Omega_1$ and $v_2 = \Gamma_2 \pm i\Omega_2$. To non-dimensionalize, the modal frequency and damping are determined by dividing the real and imaginary parts of these eigenvalues with pitch natural frequency used as the reference, ω_α, and are given as $\frac{\Omega_1}{\omega_\alpha}, \frac{\Omega_2}{\omega_\alpha}$ and $\frac{\Gamma_1}{\omega_\alpha}, \frac{\Gamma_2}{\omega_\alpha}$. The modal frequency and damping are functions of freestream velocity, U and may be plotted with a non-dimensional reduced velocity given as:

$$V = \frac{U}{b\omega_\alpha} \tag{54}$$

These plots are shown in Figure 35 in blue color. As the reduced velocity increases, the modal frequencies in pitch and plunge approach each other and may coalesce. The flutter is characterized by a bifurcation of modal damping .

If a more sophisticated aerodynamic model, such as one based on Peter's method, is used, the lift and moment are as per Equations 9 and 10 with a lift curve slope of $C_{L,\alpha} = 2\pi$ and for a unit span. The aeroelastic equations for the unit span wing are given as

$$m\ddot{h} + mx\ddot{\alpha} + k_h h = -\pi\rho b^2(\ddot{h} + U\dot{\alpha} - ba\ddot{\alpha}) + 2\pi\rho U b(\dot{h} + U\alpha + b(\frac{1}{2} - a)\dot{\alpha} - \lambda_0) \tag{55}$$

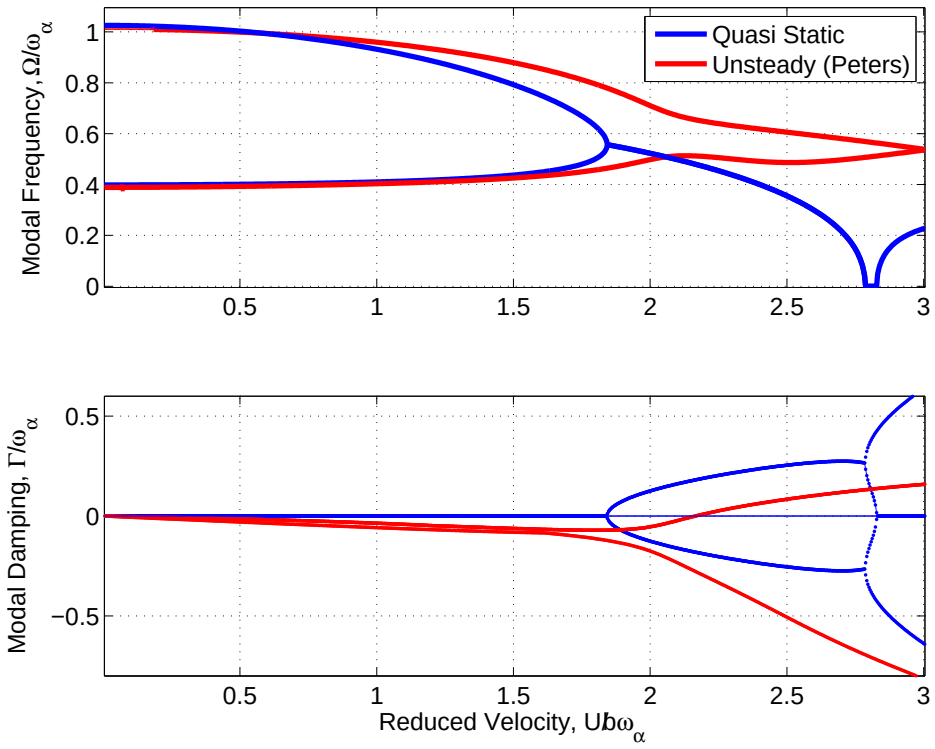

Figure 35: Flutter speed prediction for the Hodges wing with quasi static and unsteady aerodynamic models

$$I\ddot{\alpha} + mx\ddot{h} + k_\alpha \alpha = b(\frac{1}{2} + a)L - \pi\rho b^3(\frac{1}{2}\ddot{h} + U\dot{\alpha} + b(\frac{1}{8} - \frac{a}{2})\ddot{\alpha}) \tag{56}$$

For the sake of completion, equations describing the average induced velocity λ_0 are repeated here.

$$\lambda_0 \approx \frac{1}{2}\sum_{n=1}^{N} Bl_n\lambda_n \tag{57}$$

where N is the total number of induced flow states. As seen in Section 6, the number of states have a little impact on lift prediction beyond 4. Thus Peter's model with $N = 6$ is used in the current work for simulations and comparison with experiments.

λ_n follows the state equation:

$$[Al]\{\dot{\lambda}\} + \frac{U}{b}\{\lambda\} = \{cl\}(\ddot{h} + U\dot{\alpha} + b(\frac{1}{2} - a)\ddot{\alpha}) \tag{58}$$

and

$$[Al] = [Dl] + \{dl\}\{bl\}^T + \{cl\}\{dl\}^T + \frac{1}{2}\{cl\}\{bl\}^T \tag{59}$$

In the above equations, bl, cl, dl and Dl are known functions of n and N and are given as

$$Dl_{nm} = \begin{cases} \frac{1}{2n}, & \text{for } n = m + 1 \\ \frac{-1}{2n}, & \text{for } n = m - 1 \\ 0, & \text{for } n \neq m \pm 1 \end{cases} \tag{60}$$

$$bl_n = \begin{cases} (-1)^{(n-1)} \frac{(N+n-1)!}{(N-n-1)!} \frac{1}{(n!)^2}, & \text{for } n \neq N \\ (-1)^{(n-1)}, & \text{for } n = N \end{cases} \tag{61}$$

$$dl_n = \begin{cases} \frac{1}{2}, & \text{for } n = 1 \\ 0, & \text{for } n \neq 1 \end{cases} \tag{62}$$

$$cl_n = \frac{2}{n} \tag{63}$$

To solve the equations with Peter's model, we assume a state vector as previously defined, but, in addition to the four states, the state vector will have an additional six states, λ_1 through λ_6. Thus, $x = [h\ \dot{h}\ \alpha\ \dot{\alpha}\ \lambda_1\ \lambda_2\ \lambda_3\ \lambda_4\ \lambda_5\ \lambda_6]^T$ and $\dot{x} = [\dot{h}\ \ddot{h}\ \dot{\alpha}\ \ddot{\alpha}\ \dot{\lambda_1}\ \dot{\lambda_2}\ \dot{\lambda_3}\ \dot{\lambda_4}\ \dot{\lambda_5}\ \dot{\lambda_6}]^T$. Using this formulation, the equations of motion take the form

$$[A]\{\dot{x}\} = [B]\{x\} \tag{64}$$

$[A]$ and $[B]$ are matrices given by

$$A = \begin{bmatrix} A1_{(4X4)} & A2_{(4X6)} \\ A3_{(6X4)} & Al_{(6X6)} \end{bmatrix}_{10X10} \tag{65}$$

$$B = \begin{bmatrix} B1_{(4X4)} & B2_{(4X6)} \\ B3_{(6X4)} & B4_{(6X6)} \end{bmatrix}_{10X10} \tag{66}$$

$A1, A2, A3, Al, B1, B2, B3$, and $B4$ are given by

$$A1 = \begin{bmatrix} 1 & 0 & 0 & 0 \\ 0 & m & 0 & mxb \\ 0 & 0 & 1 & 0 \\ 0 & mxb & 0 & I \end{bmatrix}_{4X4} \tag{67}$$

$$A2 = \begin{bmatrix} 0 & \dots & 0 \\ \vdots & \ddots & \vdots \\ 0 & \dots & 0 \end{bmatrix}_{4X6} \tag{68}$$

$$A3 = \begin{bmatrix} 0 & -cl_1 & -Ucl_1 & -b(\frac{1}{2} - a)cl_1 \\ \vdots & \vdots & \vdots & \vdots \\ 0 & -cl_6 & -Ucl_6 & -b(\frac{1}{2} - a)cl_6 \end{bmatrix}_{6X4} \tag{69}$$

and $[Al]_{6X6}$ is given as

$$[Al]_{6X6} = [Dl]_{6X6} + \{dl\}_{6X1}\{bl\}^T_{1X6} + \{cl\}_{6X1}\{dl\}^T_{1X6} + \frac{1}{2}\{cl\}_{6X1}\{bl\}^T_{1X6} \tag{70}$$

$$B1 = \begin{bmatrix} 0 & 1 & 0 & 0 \\ -k_n & -2\pi\rho Ub & -2\pi\rho^2 Ub & -[\pi\rho h^2 U + 2\pi\rho Ub^2(0.5-a)] \\ 0 & 0 & 0 & 1 \\ 0 & 2\pi\rho Ub^2(0.5+a) & 2\pi\rho U^2 b(0.5+a) - ka & b(0.5-a)[\pi\rho b^2 U + 2\pi\rho b^2 U(0.5-a)] - \pi\rho b^3 U \end{bmatrix} \tag{71}$$

$$B2 = \begin{bmatrix} \{0 \;..\; 0\}_{6X1} \\ \pi\rho Ub\{bl\}_{6X1} \\ \{0 \;..\; 0\}_{6X1} \\ -\pi\rho Ub(0.5-a)\{bl\}_{6X1} \end{bmatrix}_{4X6} \tag{72}$$

$$B_3 = \begin{bmatrix} 0 & 0 & 0 & 0 \\ 0 & 0 & 0 & 0 \\ 0 & 0 & 0 & 0 \\ 0 & 0 & 0 & 0 \\ 0 & 0 & 0 & 0 \\ 0 & 0 & 0 & 0 \end{bmatrix}_{6X4} \tag{73}$$

$$B_4 = -\frac{U}{b}\begin{bmatrix} 1 & 0 & 0 & 0 & 0 & 0 \\ 0 & 1 & 0 & 0 & 0 & 0 \\ 0 & 0 & 1 & 0 & 0 & 0 \\ 0 & 0 & 0 & 1 & 0 & 0 \\ 0 & 0 & 0 & 0 & 1 & 0 \\ 0 & 0 & 0 & 0 & 0 & 1 \end{bmatrix}_{6X6} \tag{74}$$

The modal frequency and modal damping is calculated similar to the previous case. The matrix $A^{-1}B$ has 10 eigenvalues (hence 5 pairs of modal frequencies and damping) but out of these only 2 pairs show the expected behavior marked by coalescence of modal frequencies and modal damping crossing x-axis. These are given in Figure 35. In this case, the flutter is characterized by the modal damping curve crossing x-axis at zero damping. The purpose of this example, is to establish the technique and reproduce the results obtained by Hodges. It is found that the predictions of flutter speed and flutter frequency match the findings reported in [2]. The reduced flutter velocity using the quasi-static aerodynamic model is found to be $V_F/b\omega_\alpha = 1.843$ and the corresponding flutter frequency is found as $\Omega_F/\omega_\alpha = 0.5565$. For unsteady aerodynamics case with Peter's method, the reduced flutter speed and flutter frequency are found as $V_F/b\omega_\alpha = 2.165$ and $\Omega_F/\omega_\alpha = 0.6557$ respectively. These results closely match the predictions as reported in reference [2]. Now, this technique will be applied to the modified system equations representing the experimental hardware. Flutter behavior will be explored with different aerodynamic models and in presence of viscous structural damping.

6.1.2 Flutter speed of wing on NATA

In this section, the eigenvalue solution technique (p-method) validated in the previous section is applied to the current NATA II wing. The effect of various aerodynamic models and structural damping on flutter speed is studied. Since this technique is only applicable to linear systems, the plunge damping is modeled as viscous. The equations of motion are presented in Equations 37 and 38. The aeroelastic equations assuming quasi- static aerodynamics are listed as

$$m_h\ddot{h} + mxb\ddot{\alpha} + c_h\dot{h} + k_h h = -C_{L,\alpha}\rho U^2 bs\alpha \tag{75}$$

$$I\ddot{\alpha} + mxb\ddot{h} + c_\alpha\dot{\alpha} + k_\alpha\alpha = C_{L,\alpha}\rho U^2 b^2 s\alpha(\frac{1}{2} + a) \tag{76}$$

The aeroelastic equations assuming Peter's model for unsteady aerodynamics model are given as

$$m_h\ddot{h}+mxb\ddot{\alpha}+c_h\dot{h}+k_h h = -(\pi\rho b^2 s(\ddot{h}+U\dot{\alpha}-ba\ddot{\alpha})+C_{L,\alpha}\rho Ubs(\dot{h}+U\alpha+b(\frac{1}{2}-a)\dot{\alpha}-\lambda_0)) \tag{77}$$

$$I\ddot{\alpha} + mxb\ddot{h} + c_\alpha\dot{\alpha} + k_\alpha\alpha = b(\frac{1}{2} + a)L - \pi\rho b^3 s(\frac{1}{2}\ddot{h} + U\dot{\alpha} + b(\frac{1}{8} - \frac{a}{2})\ddot{\alpha}) \tag{78}$$

And, using the simpler unsteady aerodynamic model ($\lambda_0 = 0$), the aeroelastic equations are

$$m_h\ddot{h}+mxb\ddot{\alpha}+c_h\dot{h}+k_h h = -(\pi\rho b^2 s(\ddot{h}+U\dot{\alpha}-ba\ddot{\alpha})+C_{L,\alpha}\rho Ubs(\dot{h}+U\alpha+b(\frac{1}{2}-a)\dot{\alpha})) \tag{79}$$

$$I\ddot{\alpha} + mxb\ddot{h} + c_\alpha\dot{\alpha} + k_\alpha\alpha = b(\frac{1}{2} + a)L - \pi\rho b^3 s(\frac{1}{2}\ddot{h} + U\dot{\alpha} + b(\frac{1}{8} - \frac{a}{2})\ddot{\alpha}) \tag{80}$$

Using the above three sets of equations, the eigenvalue analysis is conducted using the p-method as described in the previous section. The flutter speed prediction is

studied as a function of complexity of aerodynamic model, maintaining pitch and plunge values as determined by the system identification in section 4.2.4. Figure 36

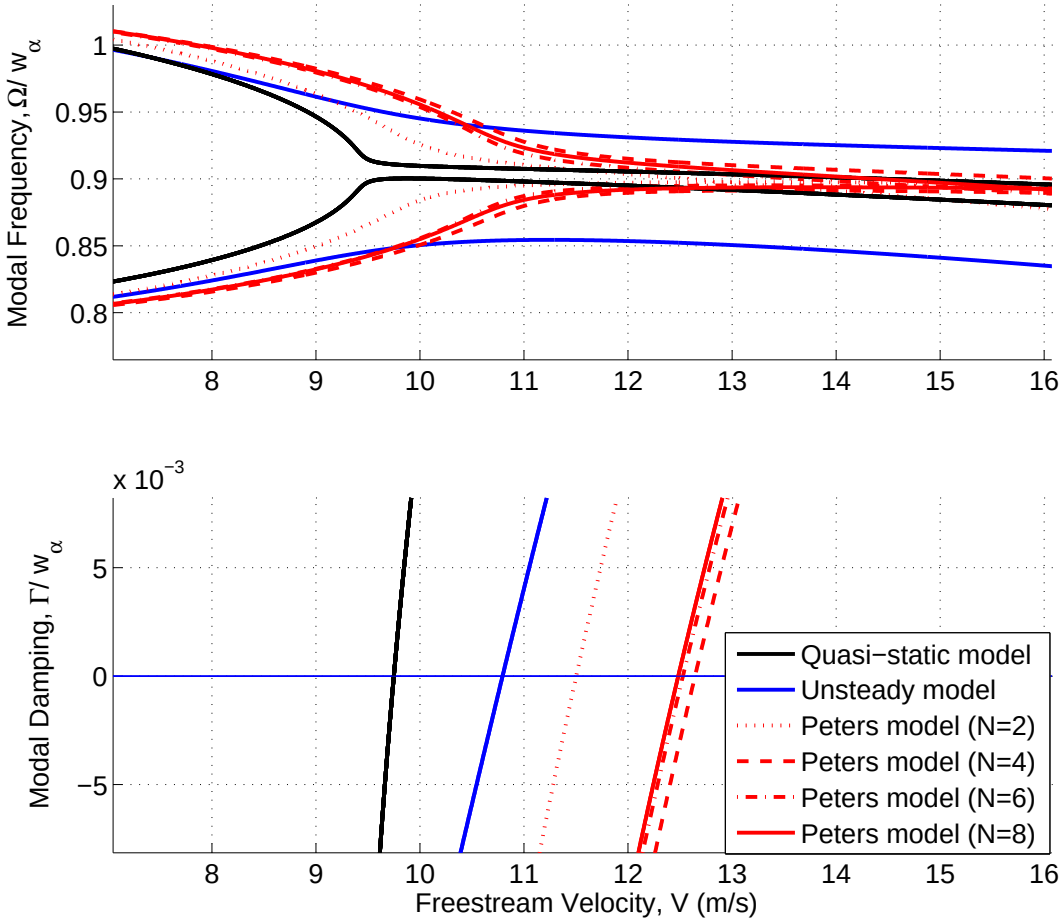

Figure 36: Flutter speed prediction of NATA wing as a function of aerodynamic models with damping values $\zeta_h = 0.0416, \zeta_\alpha = 0.0322$

shows the dependence of flutter speed on choice of aerodynamic model.

The flutter speed is marked by the modal damping changes sign from negative to positive. It may be observed that the predicted flutter speed increases from

9.73 m/s to 10.57 m/s as the complexity of aerodynamic model increases form quasi-static to unsteady model and and further to 12.57 m/s in case of Peter's model. In order to study the effect of structural damping on flutter speed, the simple unsteady aerodynamic model has been chosen. This is supported by the fact that this model matches with measured aerodynamic loads as shown in Chapter 5.1. Figure 37

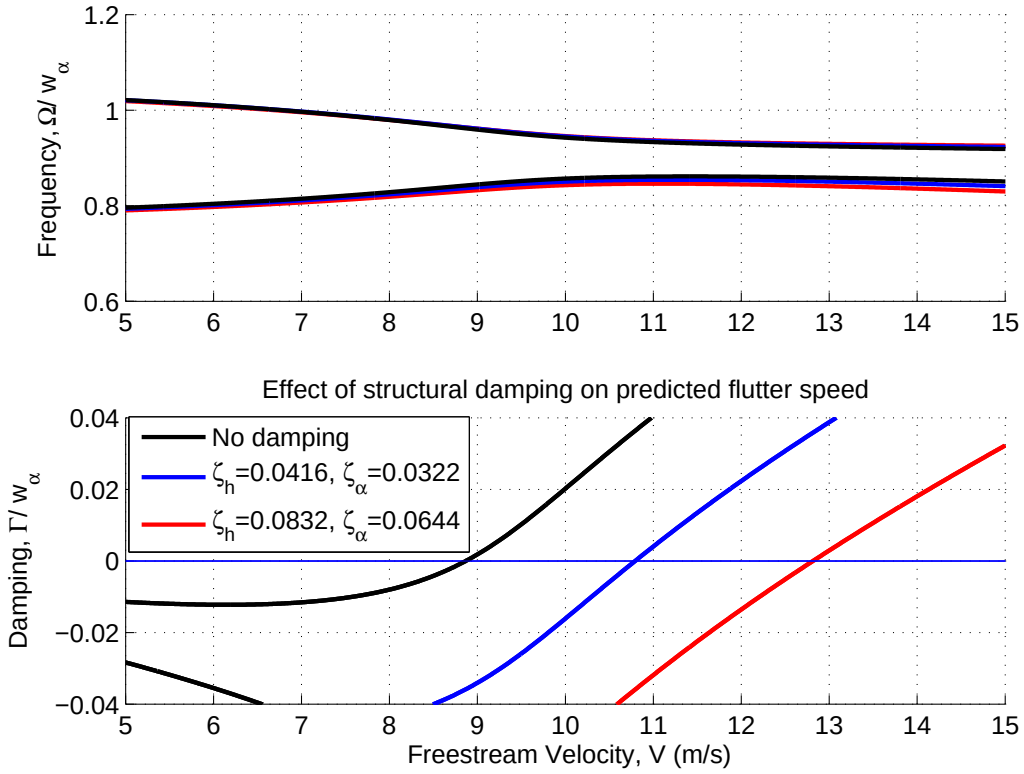

Figure 37: Effect of structural damping on predicted flutter speed

shows the behavior of flutter speed with variation in structural viscous damping. The aerodynamic model is fixed as the simple unsteady model. The three values of damping considered are zero damping, damping as identified from experiments ($\zeta_h =$

$0.0416, \zeta_\alpha = 0.322$), and twice the value of identified damping($\zeta_h = 0.0832, \zeta_\alpha = 0.644$). It is observed that increase in structural damping increases flutter speed. This is to be expected as higher dynamic pressures are required to overcome increased dissipation forces.

These predictions for the flutter speed and its dependence on damping will be compared with experimental results in chapter 8.

6.2 Time domain aeroelastic model

The previous section presents the predictive model for flutter speed and its dependence on choice of aerodynamic model and structural damping. This section details the development of a time domain nonlinear aeroelastic model and allows for a study of the dependence of aeroelastic response on nonlinearities, initial conditions and air speed. The equations of motion presented in equations 37 and 38 are cast into a state space model which may be used to simulate time domain aeroelastic response of the wing for a chosen wind speed and initial conditions in pitch and plunge. For this simulation, nonlinear pitch stiffness, the unsteady aerodynamic model, and a Coulomb plunge damping model are used. It should be noted that although Peter's model was used to explore dependence of flutter speed on type of aerodynamic model and number of lag states, the aerodynamic model used in this time domain aeroelastic model does not include any lag states. The model equations of motion are written as

$$m_h\ddot{h} + m_w x_w \ddot{\alpha} + F_d sign(\dot{h}) + k_h h = -(C_{L_\alpha}\rho U b s(\dot{h} + U\alpha + b(\frac{1}{2} - a)\dot{\alpha}) \qquad (81)$$

$$I_\alpha\ddot{\alpha}+m_w x_w\ddot{h}+c_\alpha\dot{\alpha}+k_1\alpha+k_2\alpha^2+k_3\alpha^3+k_4\alpha^4 = b(\frac{1}{2}+a)L-\pi\rho b^3 s(\frac{1}{2}\ddot{h}+U\dot{\alpha}+b(\frac{1}{8}-\frac{a}{2})\ddot{\alpha}) \tag{82}$$

A state vector x may be defined such that $x = [h\ \dot{h}\ \alpha\ \dot{\alpha}]^T$ any $\dot{x} = [\dot{h}\ \ddot{h}\ \dot{\alpha}\ \ddot{\alpha}]^T$ The equations of motion are now written in the form.

$$M\dot{x} = F(x) \tag{83}$$

such that

$$M = \begin{bmatrix} 1 & 0 & 0 & 0 \\ 0 & m & 0 & mxb \\ 0 & 0 & 1 & 0 \\ 0 & mxb+\frac{1}{2}\pi\rho b^3 s & 0 & I+\pi\rho b^4 s(\frac{1}{8}-\frac{a}{2}) \end{bmatrix} \tag{84}$$

and

$$F = \begin{bmatrix} \dot{h} \\ -C_{L_\alpha}\rho U b s(\dot{h}+U\alpha+b(\frac{1}{2}-a)\dot{\alpha})-sgn(\dot{h})F_d-k_h h \\ \dot{\alpha} \\ b(\frac{1}{2}+a)L-\pi\rho b^3 s(U\dot{\alpha})-c_\alpha\dot{\alpha}-k_1\alpha-k_2\alpha^2-k_3\alpha^3 \end{bmatrix} \tag{85}$$

Thus, the solution may be found by integrating the equation

$$\dot{x} = M^{-1}F(x) \tag{86}$$

The integration has been performed by MATLAB® function ODE45 under various initial conditions to explore the aeroelastic behavior as a function of wind speed, structural damping, etc.

The effect of airspeed on aeroelastic response is studied. Two sample outputs at different wind speeds are presented in Figure 38. The system is disturbed with the same plunge initial condition, and the simulation is allowed to develop. The two

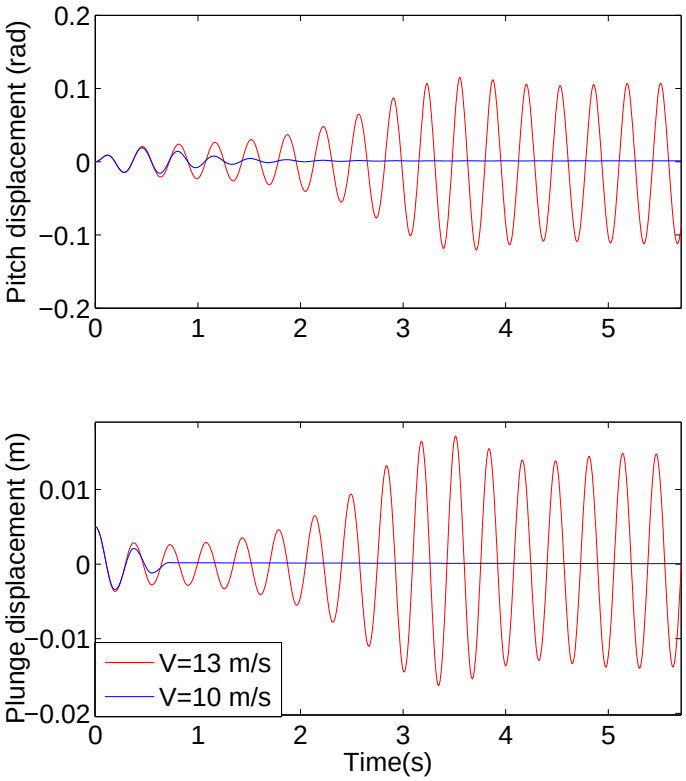

Figure 38: Effect of wind speed, U, on LCO response at the same plunge initial condition of $h_0 = 0.005\ m, \alpha_0 = 0\ rad$

speeds tested are 10 m/s and 13 m/s. These speeds are chosen because it was seen in the last section that the flutter speed is expected to be between those values. Note that the simulation predicts completely different result for these two cases. At the lower speed, the response decays in less than 1 second, but at 13 m/s, the system response grows until it reaches a limiting value. This limit is the limit cycle oscillation amplitude. This suggests that a critical speed exists between the two tested values, and beyond this critical speed, limit cycle oscillations will happen.

Figure 39 shows the behavior of system at the wind speed of 13 m/s, but with different plunge initial displacements of $h_0 = 0.004\ m$ and $h_0 = 0.005\ m$. For

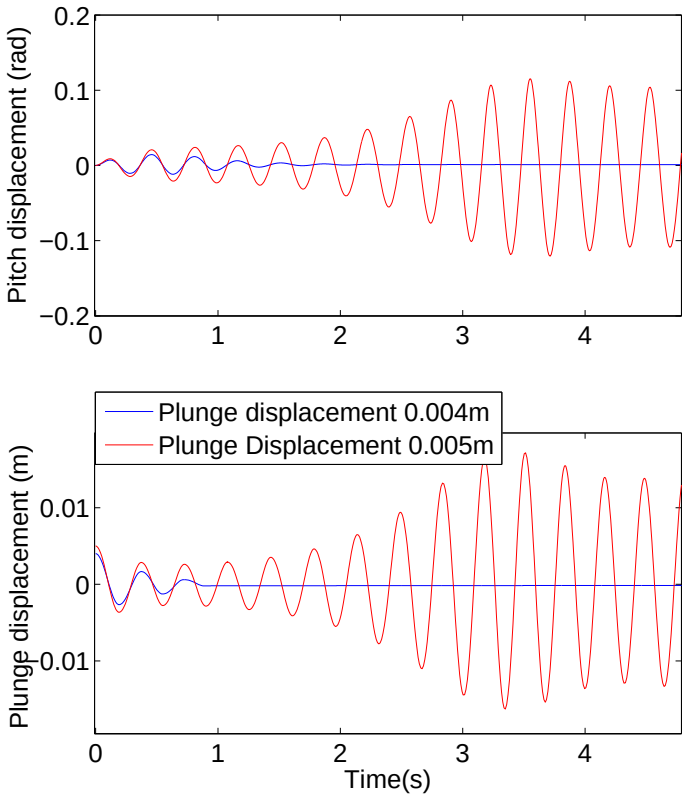

Figure 39: Effect of plunge initial condition on LCO response at $U = 13\ m/s$

such a small change in initial conditions, the system behaves markedly differently. Dependence of initial conditions is typical behavior for nonlinear systems. This also suggests that there may be a critical initial condition for a set velocity above which any system disturbance will result in oscillation.

A benefit of such a time domain aeroelastic model is the opportunity for studying phenomena which will otherwise be difficult to study by experiments. One such example is the study of aeroelastic response in absence of structural nonlinearity and frictional effects (nonlinear damping). It is interesting to repeat the numerical simulations without any structural, or damping nonlinearities. Thus, the nonlinear pitch

stiffness is replaced with a linearized pitch stiffness, Coulomb damping is replaced with viscous damping, and the system is disturbed at various plunge initial conditions at 13 m/s. The results are presented in Figure 40. There are two interesting findings here. First, when compared to the nonlinear case, the system does not oscillate within bounds. The removal of nonlinear hardening stiffness term which was responsible for bounding the system, causes the response to diverge marking flutter. Secondly, the replacement of damping nonlinearity (Coulomb damping) with viscous damping also removes initial condition dependence. All three initial conditions result in divergent behavior of the system.

The predictive models for finding the flutter boundary and both the nonlinear and linear aeroelastic response are used to generate a bifurcation diagram which is presented in Section 8 along with a comparison with experiments.

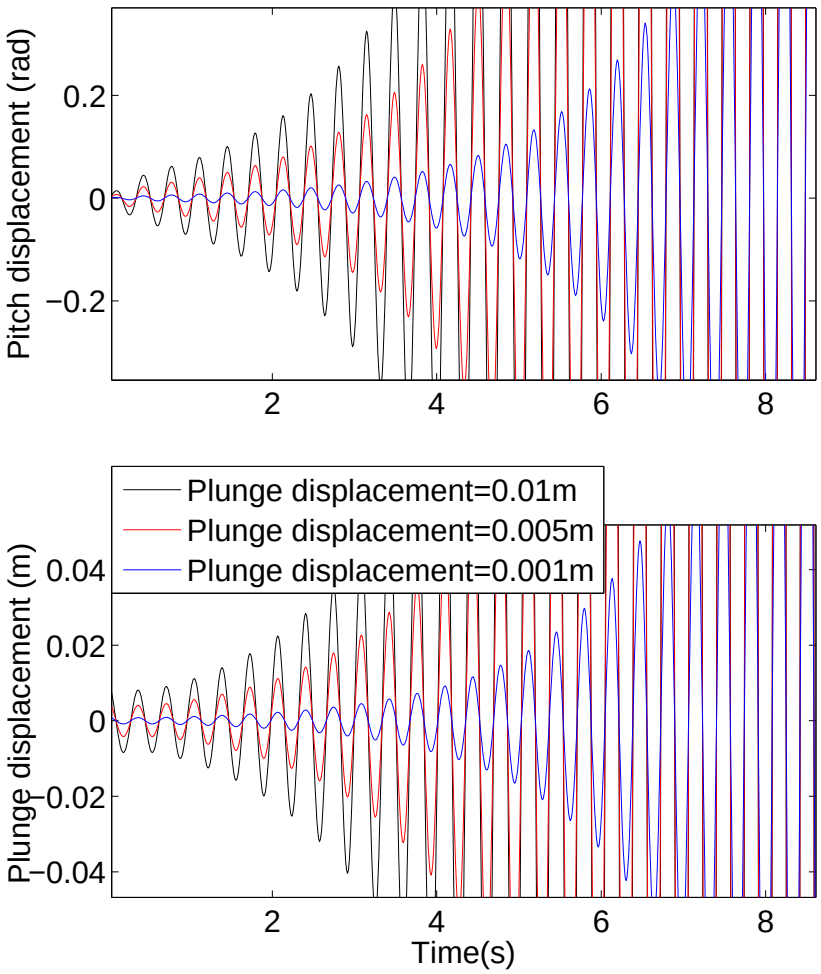

Figure 40: Effect of plunge initial condition on flutter response of linear system at $U = 13\ m/s$

7. MODELING AND VALIDATION OF GUST LOADS

This chapter presents the development of gust sniffer as a sensor, the identification process of extracting gust model from experimental data and comparison of measured aeroelastic lift with predictions. As described earlier in Chapter 3, the gust sniffer is essentially a hot film probe mounted at approximately 45° to the incoming flow The probe is connected to a Constant Temperature Anemometer (CTA) which provides both the signal conditioning and sensor balancing via Wheatstone bridge. The output voltage from the CTA corresponds to the rate cooling of the probe. The probe is calibrated for flow angularity at various wind speeds. A schematic of gust sniffer is shown in Figure 41. By design, flow with angularity causes a different level of cooling, to which the anemometer responds by an increased voltage. This change of output voltage corresponds to the angle of flow. With this calibration information, flows with small but arbitrary angularity may be measured.

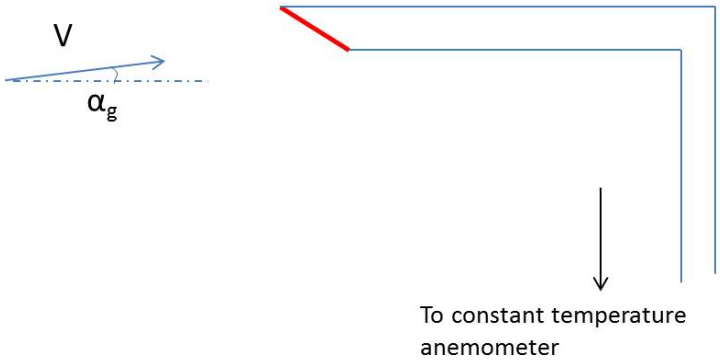

Figure 41: A sketch of Gust Sniffer

7.1 Gust Sniffer Calibration

The gust sniffer sensor is mounted on a removable circular window of the test section between the gust wing and the NATA II wing. This allows for the sniffer to sense the flow field upstream of the wing. The circular window may be rotated with the gust sniffer sensor so that the sniffer may be exposed to a known amount of flow angularity for calibration purposes. For small flow angularity ($|\alpha_g| < 5°$) it has been

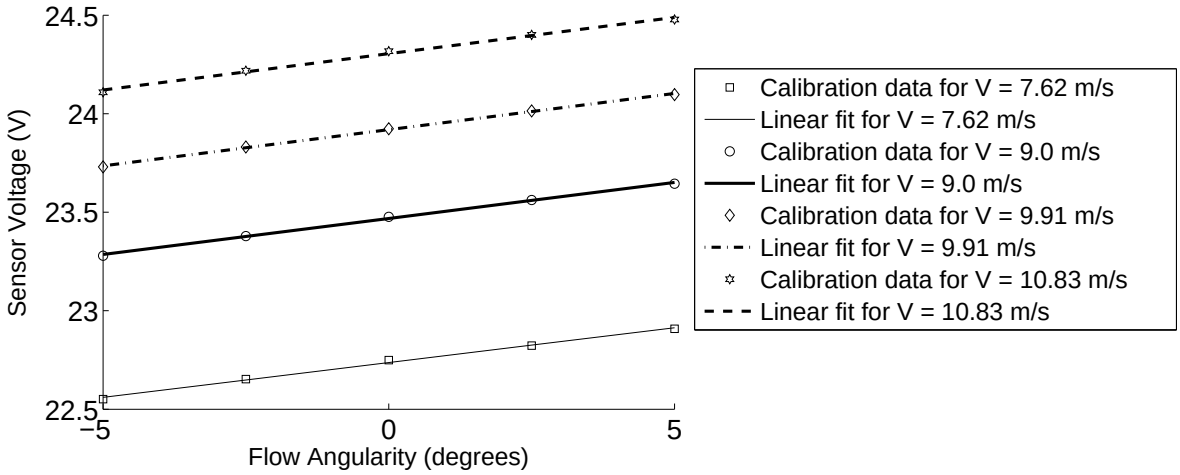

Figure 42: Gust Sniffer Calibration at various wind speeds

found that the output voltage from the anemometer is linearly proportional to the flow angularity. Moreover, the slope of the line is invariant of wind speed. Figure 42 shows the calibration plots between output voltage and flow angularity at various wind speeds.

7.2 Gust Loads Model Identification

In order to study the effect of a gust on the aeroelastic system, a model between measured gust at the sniffer and the generated loads at the wing must be found.

The classical model of Kussner [10] computes the lift on an wing as it enters a sharp edged gust. This step response may be convolved to generate a prediction of gust loads for an arbitrary gust profile. However, it has been found that Kussner's model does not lead to prediction of the loads as measured. There has been a limited effort in experimentally validating the Kussner gust model [11] . One reason could be the effects of wind tunnel walls. The size of wing may give rise to unsteady blockage effects, so models assuming free flight conditions may not be valid. Thus, a model relating measured gust angle to the loads generated at the wing has been generated from experimental data. The input data is the gust angle as measured by the sniffer and the output is the lift measured at the wing. It should be noted that during this identification process, the wing is locked in pitch and plunge. This is necessary because any motion of the wing may give rise to inertial and aerodynamic loads, not pertaining to gust at all. Figure 43 shows the input and output data. It should be noted that the gust angle is varied arbitrarily at different rates in order to cover a high bandwidth. The transfer function (in laplace domain, $\tilde{s}$) between gust angle and measured lift is given in Equation 87. Note that the symbol, s was reserved for nondimensional time, so $\tilde{s}$ is used to represent Laplace domain.

$$L_g(\tilde{s}) = \frac{-0.2741\tilde{s} + 0.03611}{\tilde{s}^2 + 1.301\tilde{s} + 0.1092} \quad \alpha_g(\tilde{s}) \tag{87}$$

Figure 44 shows the lift due to a step response for the identified model and also shows the Kussner's predictions and static theory for comparison. The static theory simply treats gust angle as an effective angle of attack and there are no associated lags. Step responses are scaled with the static theory. Kussner's function predicts that the lift on the wing eventually approaches the static value after 40 units of nondimensionl time. In other words, the full effect of a gust is felt after the gust has traveled

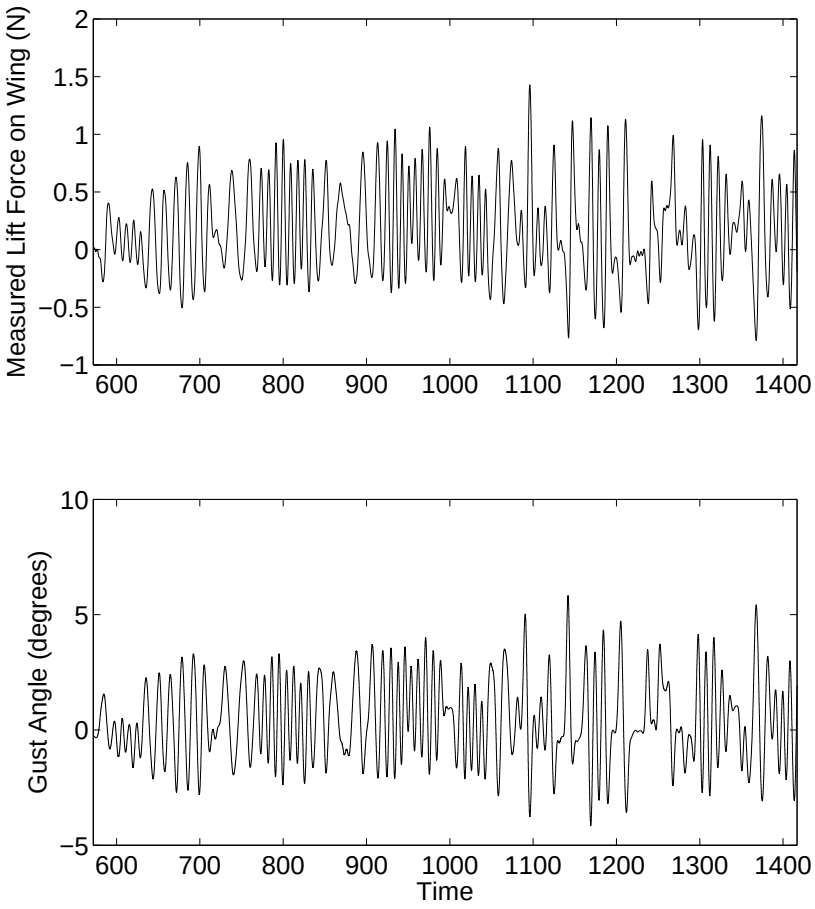

Figure 43: Measured Gust angle and lift as input experimental data for model development

40 semi-chords downstream of the wing. Since Kussner's function, by definition is the lift relative to the static theory experienced by a wing section as it encounters a sharp edged gust, it is appropriate to call the Kussner's function, the step response to gust. Thus, the identified step response from experiments may be seen as equivalent Kussner's function as extracted from the experimental data. There are two main differences when compared to Kussner's function. First, the maximum lift predicted

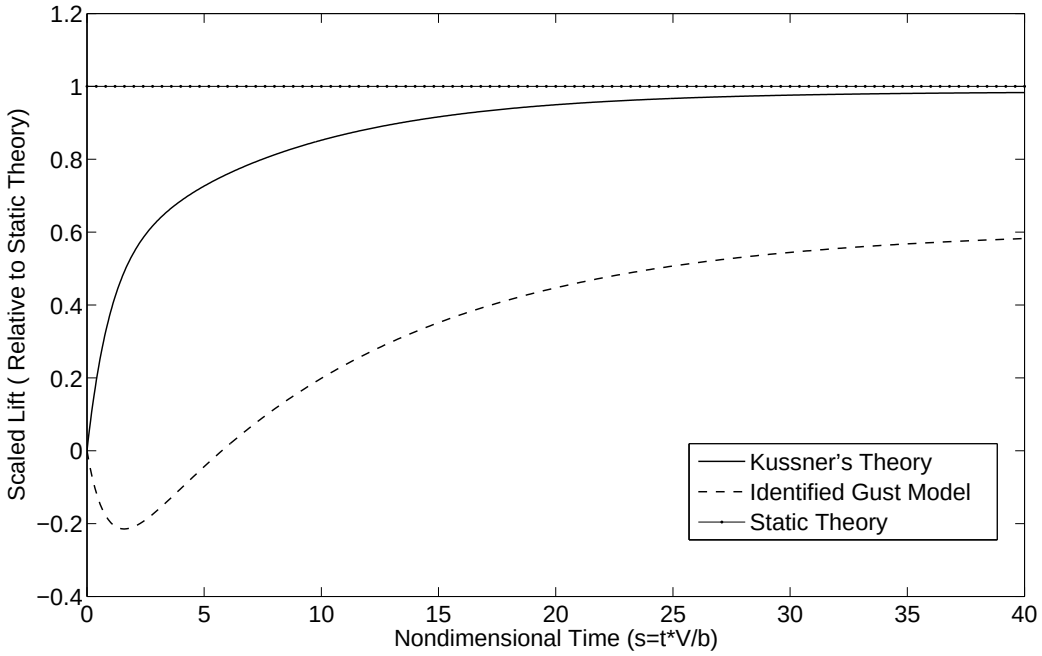

Figure 44: Comparison of Step response of gust model with theoretical models

by the model is only approximately 60% ofthe Kussner's value. Secondly, the lift drops instantly as gust angle is input and eventually increases after $s = 5$. It is not entirely clear why a dip in the step response is seen. However, it is believed that the method to generate a gust in the wind tunnel, boundary wall effects such as blockage and the placement of the gust sniffer with respect to the wing are all factors that may affect the model. The placement of the gust sniffer is an important factor because the gust sniffer measures the local value of the gust whereas the lift on the wing represents the entire effect of the flow field. Further investigations are required to ascertain the cause of this behavior.

The identified model represents the lift as measured in experiments. Figure 45 shows the measured lift with predictions from the identified model, Kussner's model and static theory. It may be seen that the identified model provides a good approach

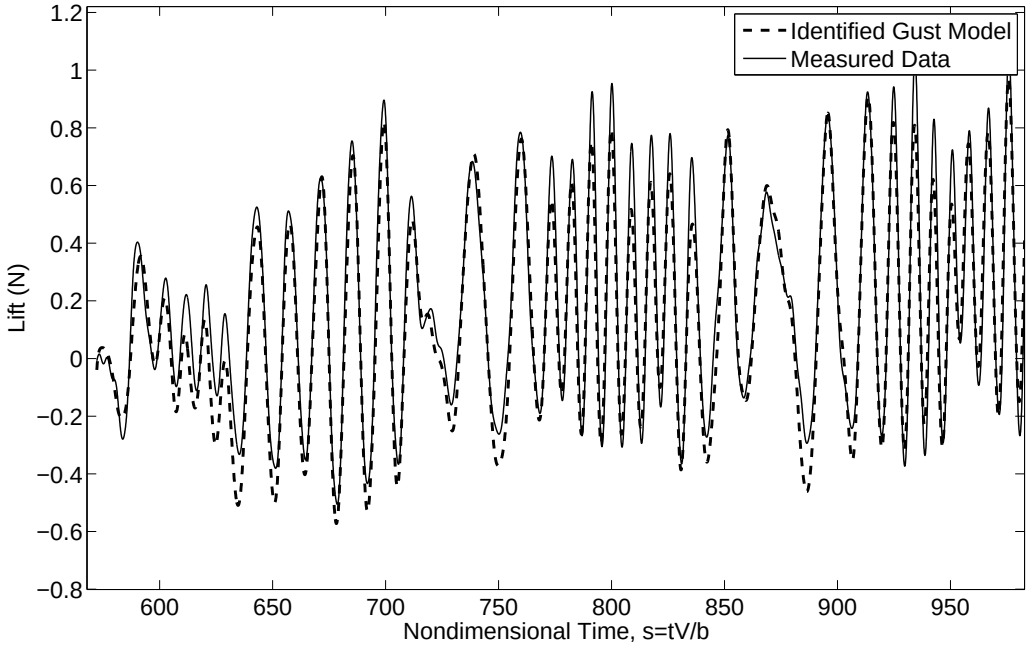

Figure 45: Comparison of predictions of gust model theoretical models with measured data

to predict lift.

This identified gust loads model is integrated with unsteady aerodynamics model and aeroelastic loads in the presence of gust are predicted and compared with experiments.

7.3 Aeroelastic loads under harmonic gust

Figure 46 shows the pitch and plunge response of the wing under harmonic gusts at constant amplitude but at varying frequency at a wind speed of $U \approx 10\ m/s$. This plot may be seen frequency response of the aeroelastic wing to gust. It should be noted that the two significant frequencies are the uncoupled pitch and plunge natural (damped) frequencies. These are determined in wind off conditions and are marked with dotted and dashed lines respectively. At forcing frequencies lower

than plunge uncoupled frequency (2.5 Hz), the gust does not induce any appreciable pitch or plunge response. At frequencies higher than plunge uncoupled frequency but lower than pitch uncoupled frequency (3.16 Hz), the plunge response amplitude does not change appreciably and pitch response remains negligible. Substantial pitch and plunge response is generated near pitch uncoupled frequency. This frequency is where the aeroelastic wing interacts the most with the gust. At higher frequencies, the response reduced before leveling at smaller values.

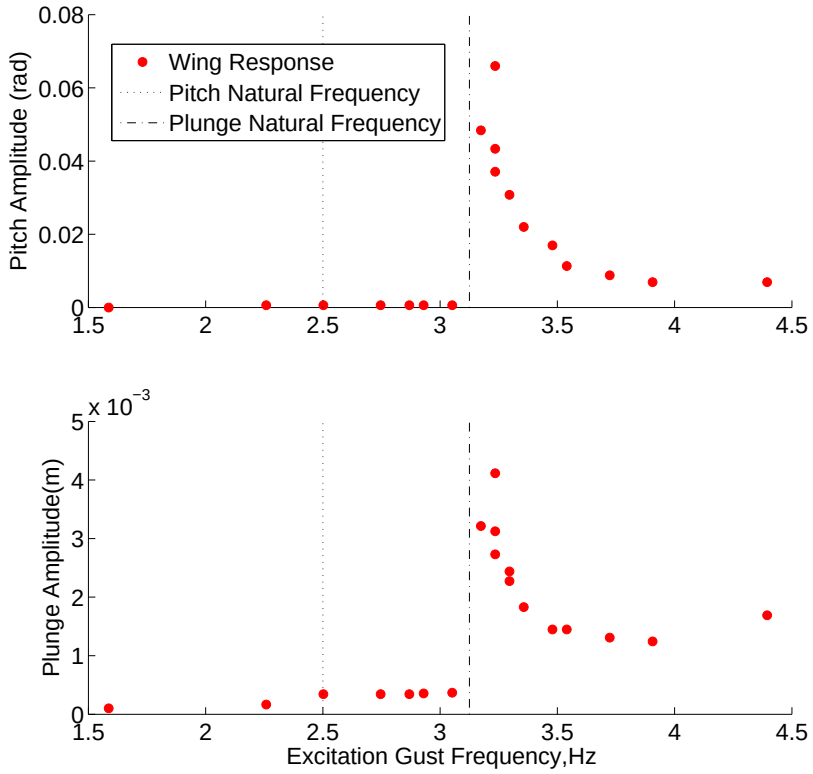

Figure 46: Comparison of predictions of gust model theoretical models with measured data at $U \approx 10\ m/s$

While the wing oscillates under the influence of gust, unsteady aerodynamic loads

and unsteady gust loads are generated. The unsteady aeroedynamic model has been combined with the gust loads model expressed by Equation 87 to predict the aeroelastic loads under gust. This combined predictive model is compared against experimental measurements. Two forcing frequencies are considered. Figure 47 shows the predicted and measured C at forcing frequency of 2.85 Hz. The predicted C_L include gust loads, unsteady aerodynamic loads and the sum of both models. It may be seen that the predicted total C_L does not match the measured C_L. However, in the second case, at forcing frequency of 3.25 Hz, the predicted total C_L shows a better match. It may be observed that at higher forcing frequency, the wing pitch response is substantial and the contribution from the unsteady aerodynamic model helps in improving the accuracy of the combined model.

These preliminary findings only scratch the surface of complex interaction of gusts, nonlinear aeroelastic effects. Further research focusing on interaction of the aeroelastic wing with gust in presence of nonlinear damping is needed along with integration of time domain aeroelastic model with gust model.

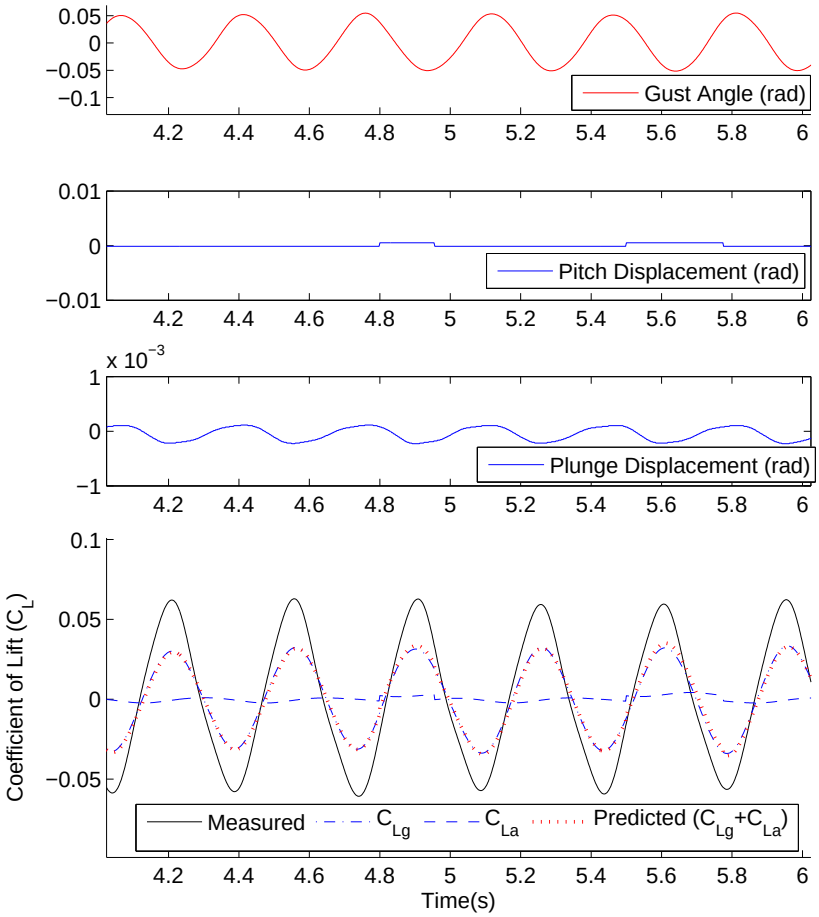

Figure 47: Comparison of predictions of gust model theoretical models with measured data

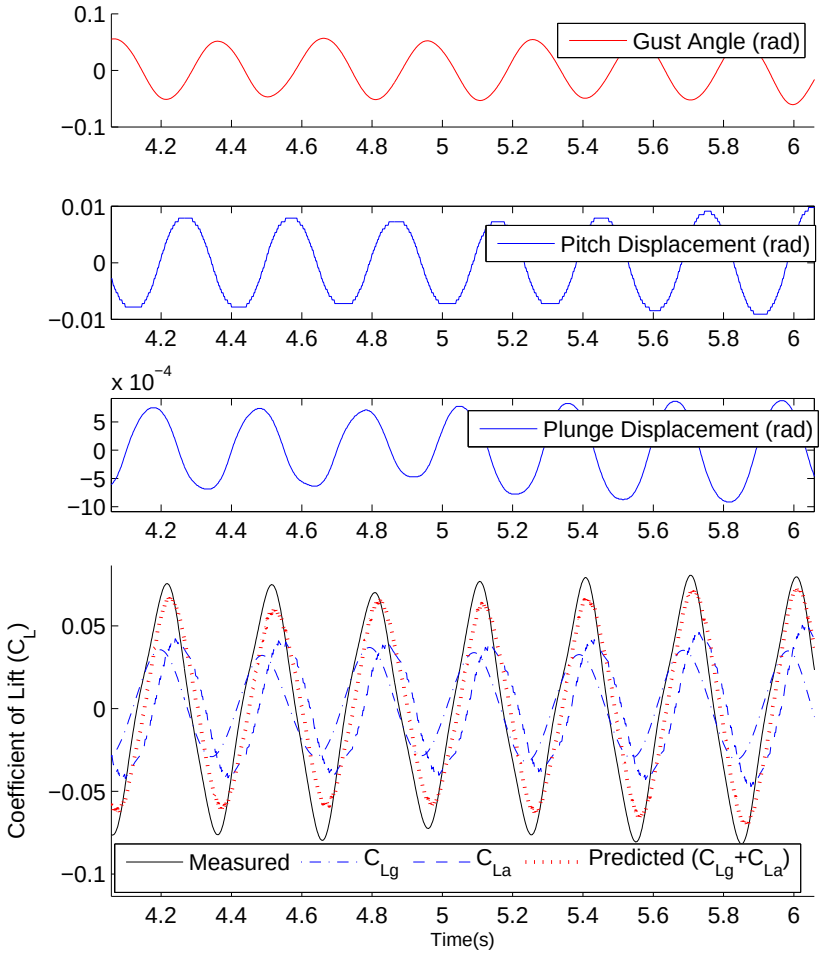

Figure 48: Comparison of predictions of gust model theoretical models with measured data

8. RESULTS AND DISCUSSION: NONLINEAR AEROELASTIC RESPONSE

This chapter presents the results from the time domain aeroelastic simulation tool presented in Chapter 6 and comparison with experimental measurements. One of the major strengths of such a tool is the flexibility to choose the system characteristics to study the behavior of system response on important features. For example, the aeroelastic system may be simulated as one without any stiffness and damping nonlinearities. Experimentally, it is impossible to completely remove these features selectively. The results presented in this chapter are of three types namely, a bifurcation diagram, time domain response and phase diagrams. The bifurcation diagrams help study the aeroelastic response as a function of a bifurcation parameter, i.e. the wind tunnel velocity and depict the various stable and unstable boundaries associated with the nonlinear system. Time domain results simply show the evolution of system behavior with time. These bifurcation diagrams are instrumental in comparing predicted behavior with measured output. The bifurcation diagrams are supported by a phase diagram to highlight nonlinear behavior characterized by the jumping of system response between stable states.

8.1 Aeroelastic behavior of Linear System: Simulations

First, the behavior of linear system is explored. Figure 49 shows the bifurcation diagram of the linear system characterized by linear pitch and plunge stiffness and viscous damping in both pitch and plunge. Such a system is expected to depict no flutter until the wind speed reaches a critical value beyond which the system will show flutter. The top plot shows the initial conditions used to excite the system. Two sets of initial conditions are shown, one set results in decayed response (no flutter) and the other set includes conditions that resulted in a divergent system response

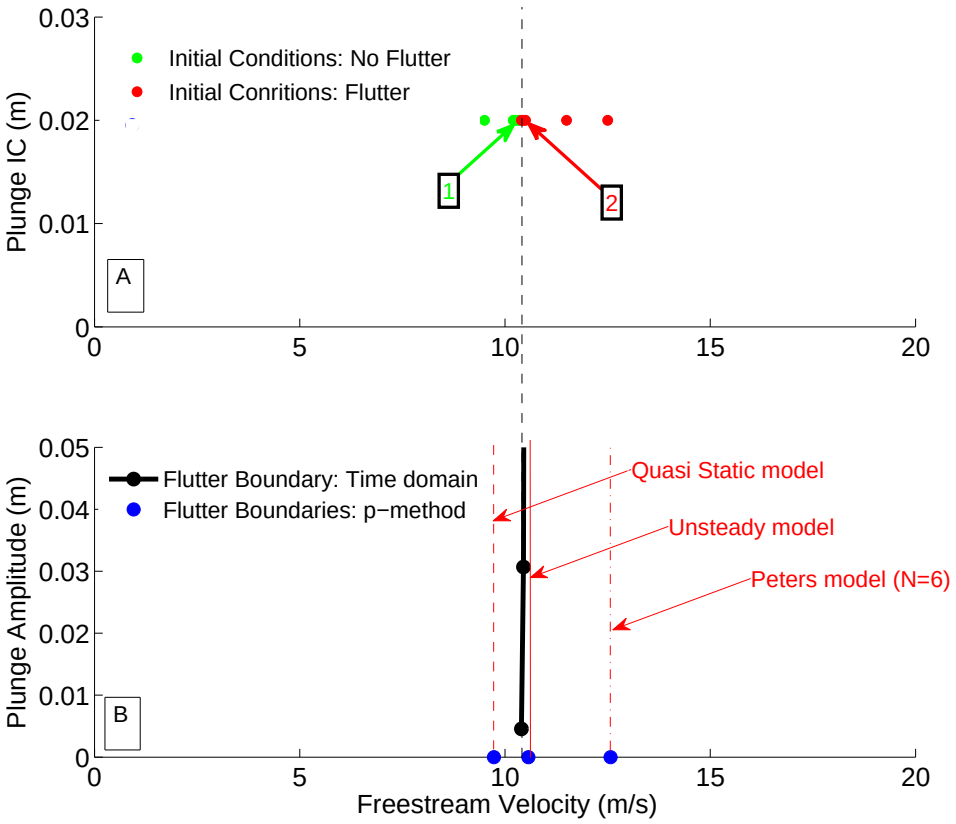

Figure 49: Determination of flutter boundary for the linear system

(flutter). The plot on the bottom shows the response of the system for cases which resulted in flutter. A vertical line may be drawn passing through $U = 10.45\ m/s$ which may be seen as the flutter boundary. This is validated by time domain system response at $U = 10.4\ m/s$ and $U = 10.45\ m/s$ as shown in Figure 50. In order to locate the flutter boundary, the simulation is run for a large time (100 seconds). It may be seen that for the same initial condition, the system response decays at $U = 10.4\ m/s$ and the oscillations grow for $U = 10.45\ m/s$ confirming that the flutter boundary as predicted by simulation of linear aeroelastic system is located at $U \approx 10.4\ m/s$.

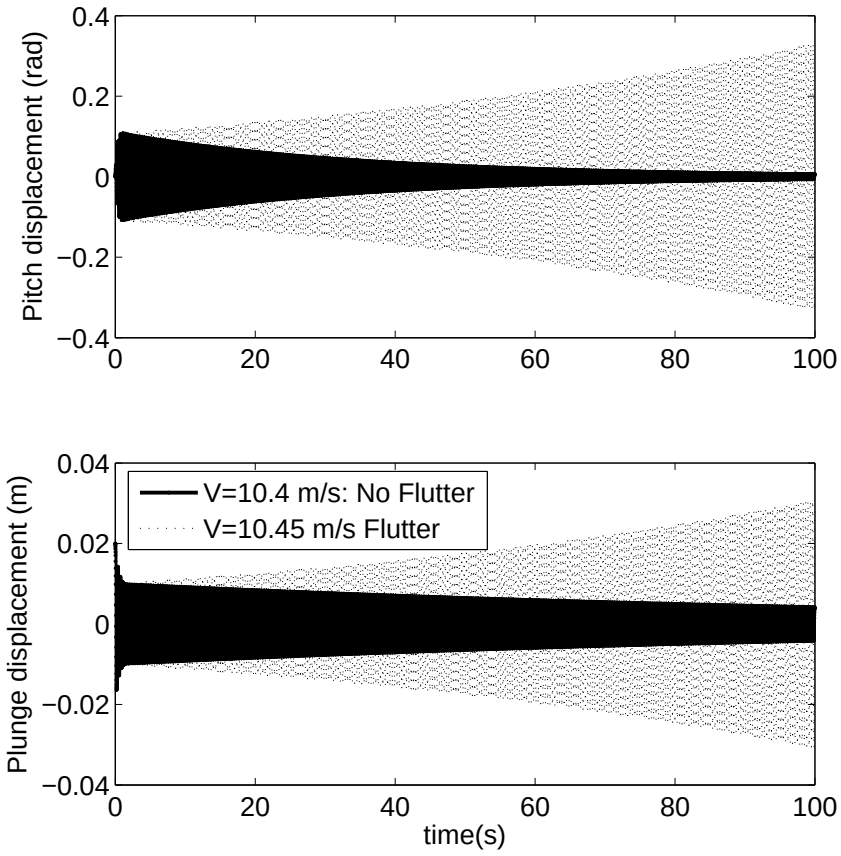

Figure 50: Validation of flutter boundary location: time domain behavior (refer back to last figure)

Also seen on Figure 49 are three blue dots on x-axis. These depict the predicted flutter speed from p-method as described in Chapter 6, Figure 36. The p-method prediction of flutter speed varies with the choice of the aerodynamic model. It may be seen that the the flutter boundary predicted by the unsteady aerodynamic model is the closest match with the flutter boundary as predicted by bifurcation studies which use the same model. Refering back to Figure 2, the linear system behavior is expected to be a vertical line passing though flutter speed.

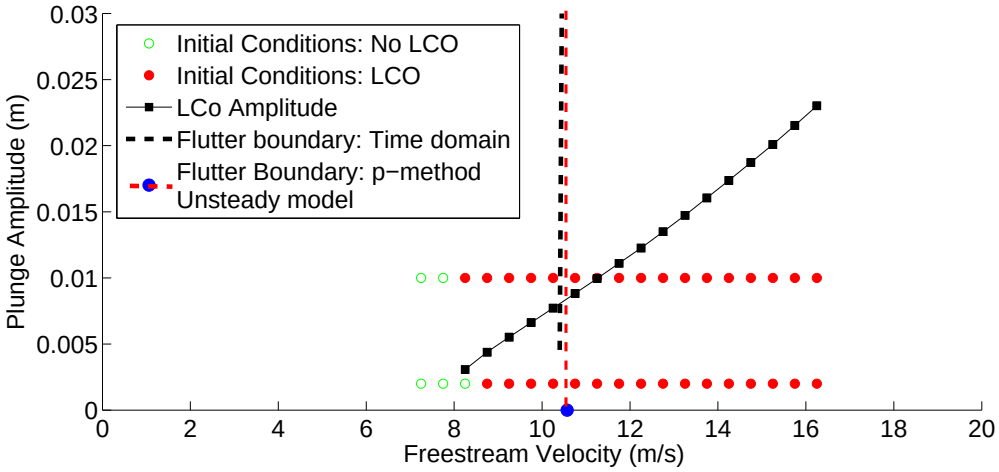

Figure 51: Comparison of predictions of gust model theoretical models with measured data

In order to examine the stiffness nonlinearity, the stiffness as identified from the system identification procedure is used instead of linear pitch stiffness. A set of initial conditions with varying plunge displacements and freestream speesd are considered and system response is plotted on the same axis. The results are presented in Figure 51. The first feature to be noted is that the system response is not divergent. For example, at 12.2 m/s, an initial displacement of $h_0 = 0.002\ m$ and $h_0 = 0.01\ m$ both result in an LCO with an amplitude of $0.012\ m$. This LCO amplitude is constant for all plunge displacements for one wind speed and vary linearly with wind speed. The LCO onset speed is also of interest. It may be seen that the LCO amplitude line may be extrapolated to meet the x-axis at LCO onset speed. The predicted LCO onset speed (approximately 7 m/s) is smaller than flutter boundary predicted by earlier methods. It appears that that the inclusion of stiffness nonlinearity in the

analysis does not prove helpful for prediction of LCO onset speed. It is concluded that stiffness nonlinearity is instrumental in capturing LCO amplitudes.

It should also be noted that the location of the stable boundary (LCO amplitude line) depends on the chosen system parameters. The parameter that seems to affect the location of this boundary the most is total pitch inertia, I_α. The identification process suggests a range of values for this parameter between $0.06 \pm 0.002\ kgm^2$. Using the extreme values, the stable boundary extremes are plotted in Figure 52.

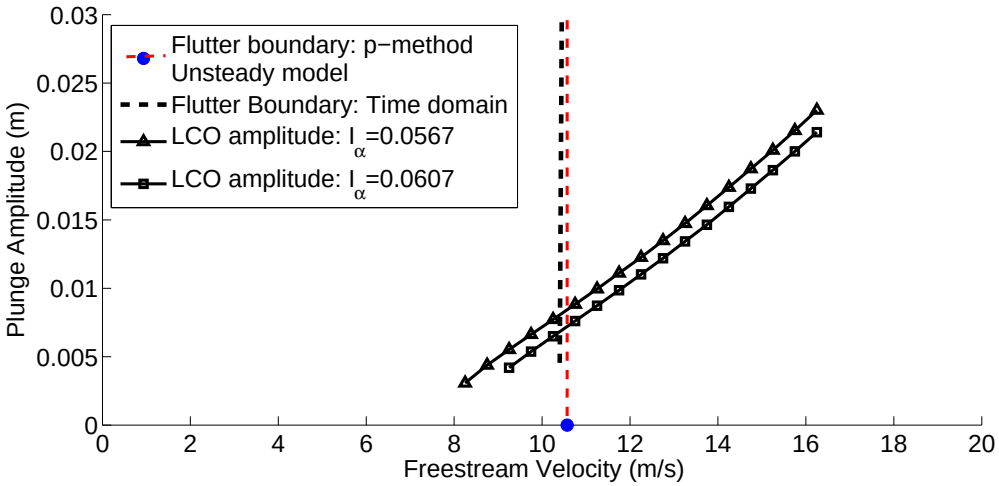

Figure 52: LCO amplitude prediction for limiting values of identified total pitch inertia

8.3 Effect of Damping Nonlinearity on Aeroelastic Response: Simulations

LCO responses that are strong functions of initial condition are not captures by simulations with linear damping. Thus, the nonlinear damping model describing dry friction (Coulomb damping model) is employed. The bifurcation diagram is generated by simulating the system response for a set of initial conditions and wind speeds. The results are presented in Figure 53. When compared to the previous case,

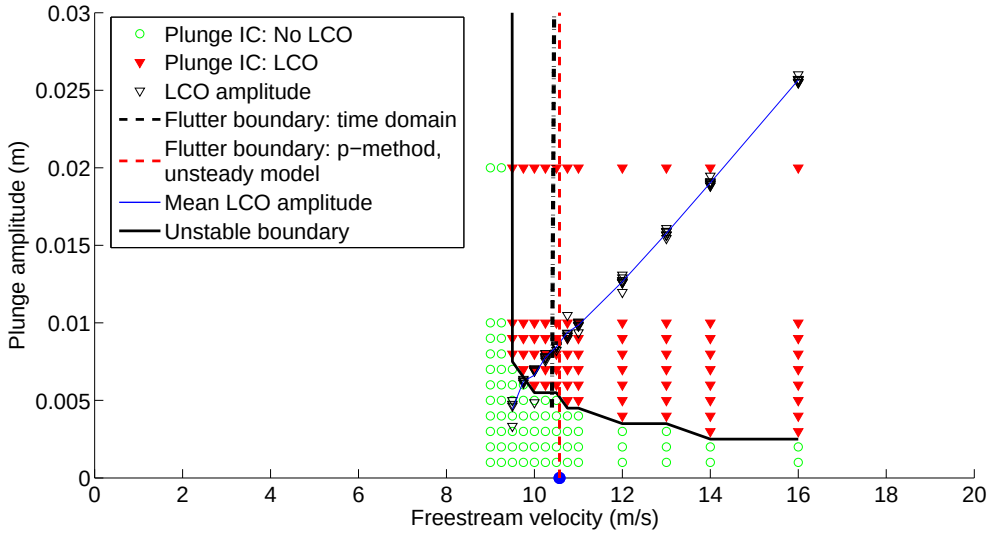

Figure 53: Comparison of predictions of gust model theoretical models with measured data

a new boundary is seen. This boundary represents the locus of the highest value of plunge displacement at each wind speed which does not result in an LCO. In other words, any plunge displacement below or to the left of this boundary will not result in an LCO. For a given wind speed, e.g. 11 m/s, a plunge displacement less than $h_0 = 0.005$ m will decay to zero and system will not result in a LCO. However any higher displacement will trigger the system to achieve a stable state marked by the LCO of amplitude of approximately 0.01 m. Note, no LCO will occur below a speed of 9.5 m/s which marks the LCO onset speed. Also, similar to the previous case, the stable LCO amplitude is somewhat independent of initial conditions and is a linear function of wind speed.

When compared to Figure 2 b repeated here as Figure 54, the simulation captures the jump behavior. Below the flutter speed, LCO is possible as long as displacements are high enough. However, the generic sketch shows that the unstable

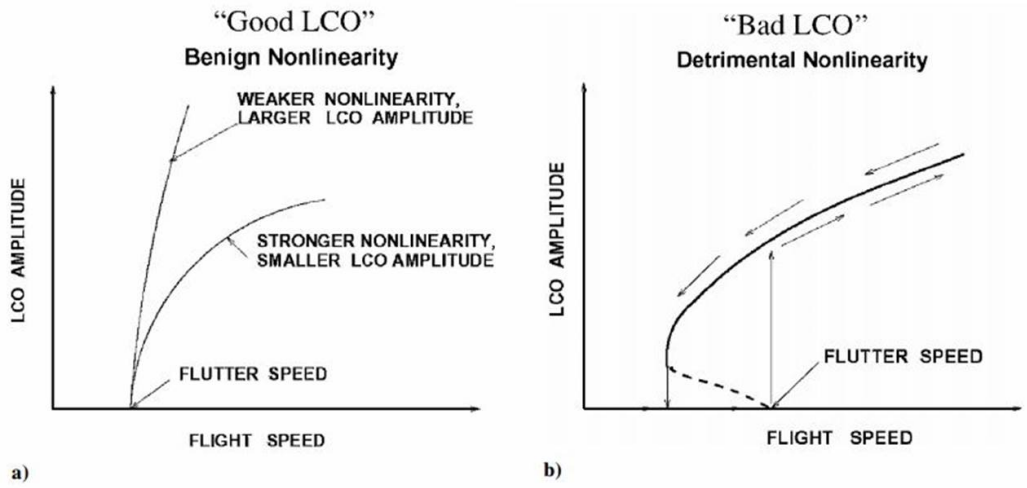

Figure 54: Schematic of LCO response. Figure 1 from [1]

boundary meets the x-axis at flutter speed, whereas the current simulation predicts that unstable boundary does not meet the x axis even at high speeds.

8.4 Stable and unstable boundaries: Simulations

Figure 55 shows the upper and lower bounds for stable and unstable boundaries. The stable boundary (marked in red with triangular markers) and the unstable boundary (marked in blue with triangular markers) are dependent on total pitch inertia, I_α, and the value of Coulomb damping, F_d. It has been found that the identification process predicts a range of F_d depending on sample data. The range of F_d values are found to be $2.0 \pm 0.5\ N$ and that of I_α is found to be $0.0587 \pm 0.002\ kg\ m^2$ as found by the system identification process. Also seen in Figure 55, are the flutter boundary predictions from time domain aeroelastic model and p-method using unsteady aerodynamic model and Peter's model. The following observations are made by this information:

- The predicted LCO onset speed is a strong function of nonlinear damping. The

assumption of a pure Coulomb model and the assumption of constant damping values may be responsible for a large variance in identified damping values (25%).

- The flutter speed predicted by time domain model ($\approx 10.4\ m/s$) is close to the value predicted by p-method with unsteady aerodynamics model ($\approx 10.4\ m/s$) and these values lie within the predicted boudnds of LCO onset speed ($\approx 9.5 - 11\ m/s$). The flutter speed predicted by p-method (Peters aerodynamics model) is much higher. However, all flutter boundary predictions are simulations and it cannot be concluded which method predicts flutter speed most accurately.

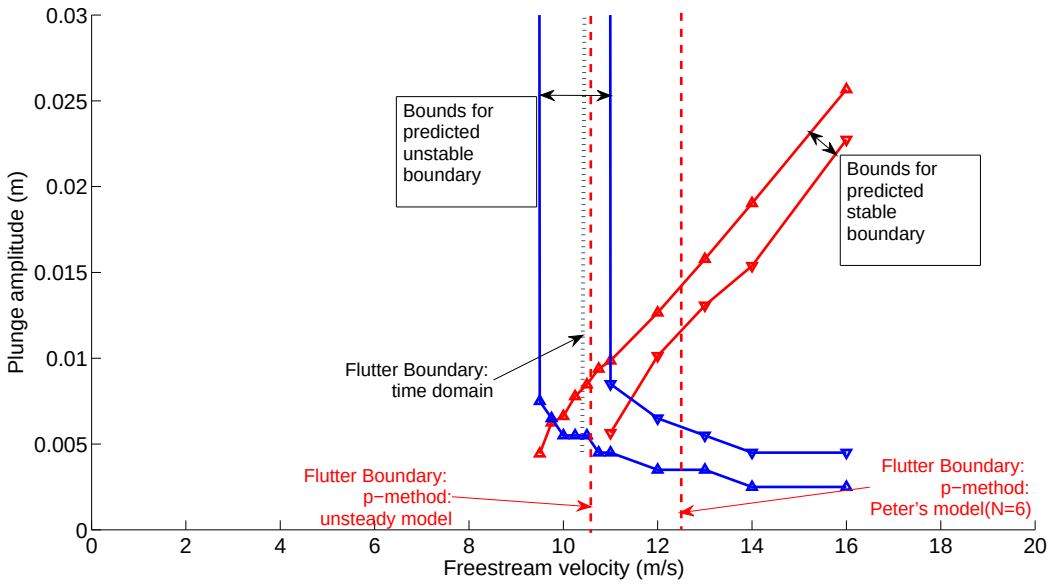

Figure 55: Effect of identification errors on stable and unstable boundaries

8.5 Stable and unstable boundaries: Simulations and Experiments comparison

The stable and unstable boundaries are compared with those generated by experiments. Figure 56 presents the unstable boundaries predicted by simulation and experiments It is observed that the best prediction of flutter speed is at 11 m/s

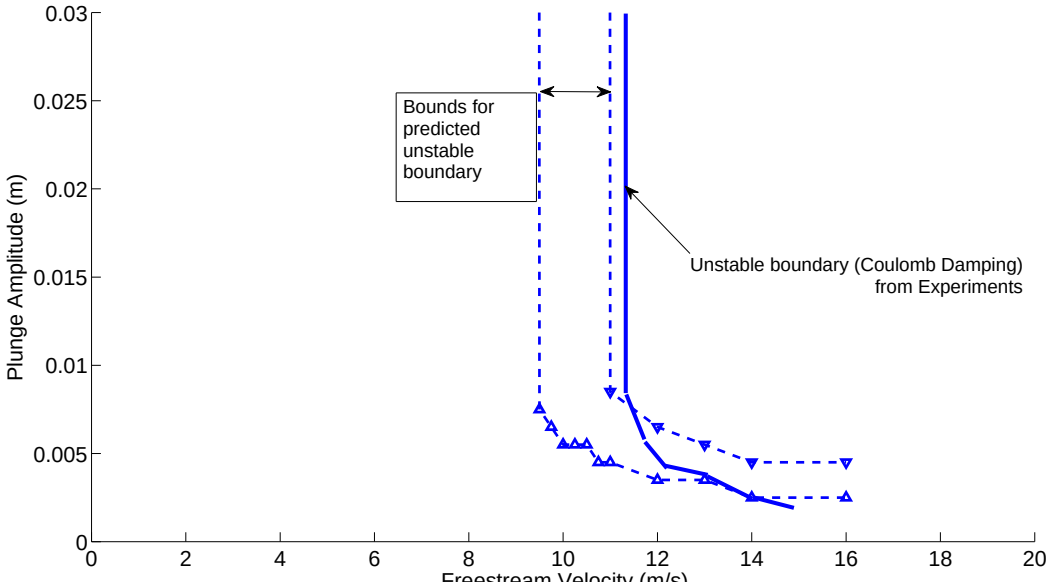

Figure 56: Comparison of predicted and measured unstable boundaries

whereas the measured value is approximately 11.4 m/s. The part of boundary between 11.5 m/s and 15 m/s is predicted by the simulation. It is reminded that the simulation assumes the unsteady aerodynamics model. It is conceivable that adoption of Peter's model increases the amount of aerodynamic damping which could result in a better match with experiments. Further work exploring this possibility is recommended.

Figure 57 presents the stable boundary comparison between simulations and experiments. The following observations are made.

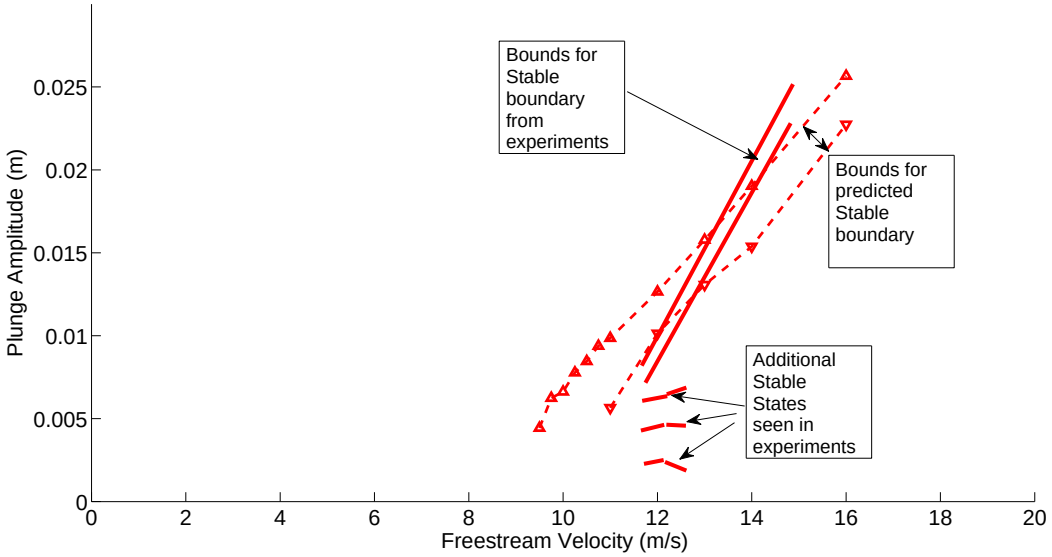

Figure 57: Comparison of predictions of gust model theoretical models with measured data

The slope of predicted stable boundary is lower than the slope of measured boundary. Thus, At high wind speeds ($U > 14\ m/s$), the observed LCO in experiments at higher than the predicted values. The slope of this boundary is related to the structural nonlinearity. It is hypothesized that at higher speeds, aerodynamic effects such as blockage and other boundary corrections may be responsible for the behavior. Apart from the primary stable boundary, the experiments show the presence of multiple semi-stable states observed at onset of LCO and extend upto $12.5 m/s$. It is observed that in the wind speed range of 11.6 m/s through 12.5 m/s, not all LCOs fall on the primary boundary. Some intermediate LCOs are also observed for smaller disturbances. Herein, these states are called 'semi-stable' states. They show a similarity to a stable boundary as the system settles into a constant amplitude LCO like behavior. But without any further input, after a finite time, it changes its state to another similar state or primary LCO. These jumps in states may be between

two semi-stable states or between a semi-stable state and the stable state. Once the system reaches the primary stable state, it does not return to the semi-stable state. There was no pattern observed pertaining to the jump behavior and there was no relation observed between initial conditions and semi-stable state reached. One instance of jump behavior is shown as a phase diagram in Figure 58. The plot on top shows the time domain response. It is noted that the system settles into a state that resembles a small amplitude LCO for approximately 20 seconds before it it gradually jumps into a higher amplitude state. This new state is the primary LCO. The phase diagram shown below shows the two orbits. It is interesting to note that considering the aeroelastic model with Coulomb damping and nonlinear stiffness are unable to capture this phenomena.

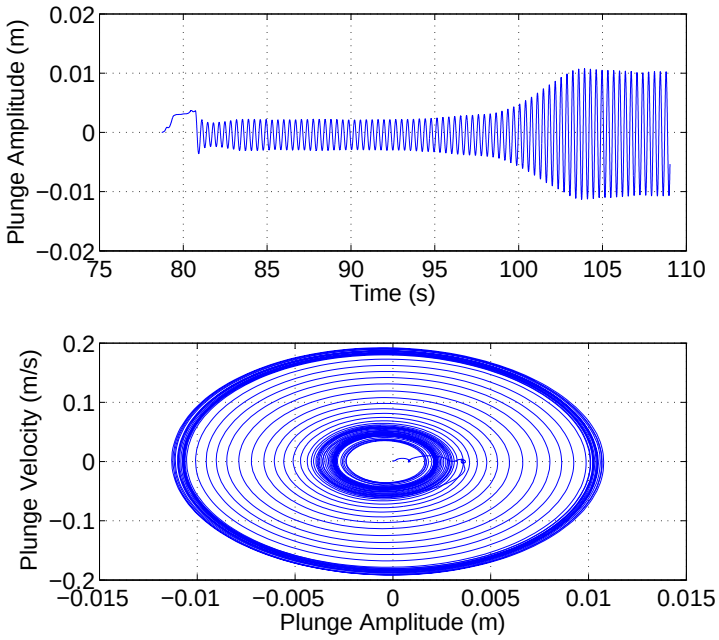

Figure 58: Comparison of predictions of gust model theoretical models with measured data

Figure 59 shows experimentally observed boundaries, semi stable states and predicted flutter boundaries. This bifurcation diagram may be compared to the bifurcation sketch reported in the literature (Figure 54). The sketch predicts that the unstable boundary meets the x-axis indicating that at high speeds, the slightest disturbance will result in LCO. In the current wind tunnel experiments, it was observed that although the unstable boundary approaches x-axis, they do not intersect. The experiments could not be carried out beyond 16.5 m/s because of large LCO amplitudes. This difference may be due to the linear bearings used in the experimental setup.

Also of importance is the flutter speed. As shown in the sketch, the flutter speed is higher than LCO onset speed. In the current work, we were not able to locate flutter speed experimentally. Out of the three methods that are employed to predict flutter speed, Peter's method predicts the flutter speed higher than the experimentally observed LCO speed. This is another area identified where further investigation is recommended for experimental determination of flutter speed and ascertaining the validity of models.

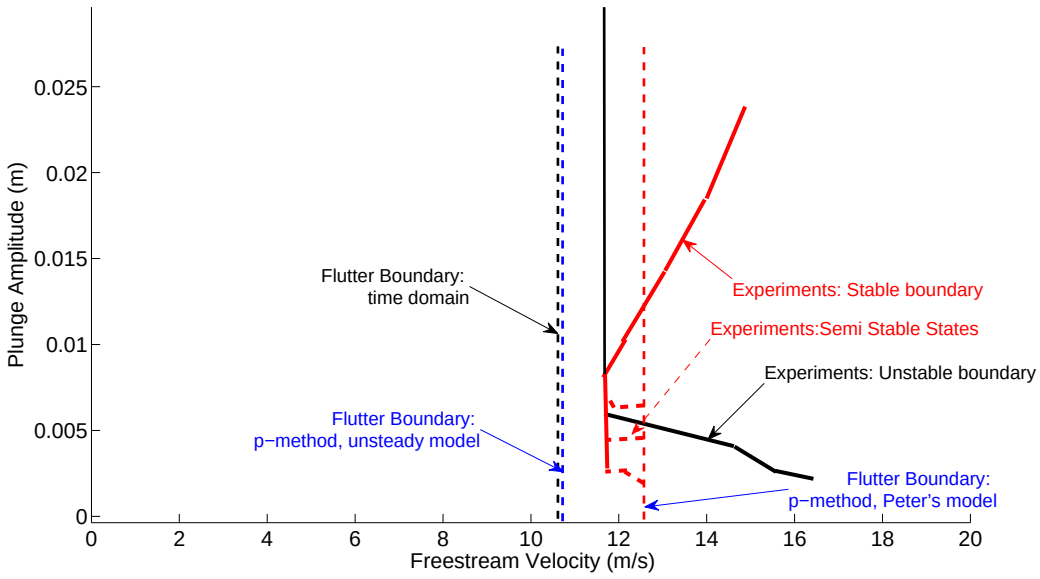

Figure 59: Experimental boundaries

9. CONCLUSIONS AND FUTURE WORK

This research describes the development of an aeroelastic model capable of predicting aeroelastic response of a typical wing section under gust. Experimental facility including a flexible free vibration pitch plunge mount, a forced oscillation apparatus and a new gust sniffer sensor have been developed. Various aspects of the model including the aerodynamic model, structural model and the gust model are validated with experiments.

The effect of nonlineariries on onset and evolution of aeroelastic instabilities including flutter and LCO has been studied in detail. Through bifurcation diagrams, the sensitivity of various boundaries (stable and unstable) to uncertainties in system parameters such as inertia and damping has been explored. the phenomena of semi-stable states in aeroelastic behavior is observed experimentally. This phenomena is not captured by predictive model. The classical models for gust response are found to not predict the measured loads on the wing. A transfer function has been identified to represent experimentally observed gust loads. This gust model is integrated with the aeroelastic model to predict aeroelastic response under gusts.

This predictive tool and accompanying experimental facility will serve as a platform for continuing research in development of aeroservoelastic control techniques.

Three areas for future works have been identified.

1. The identified gust loads model does not match the classical theory. Also the identified model has inconsistent performance in predicting aeroelastic loads under gust. It is not clear if wind tunnel boundary wall effects are affecting the predicted model. Also the gust sniffer does not provide a full picture of the flow field angularity since it is a point measurement. A full survey of gust field

will also enable a better model. A robust gust model is key to demonstration of GLA control laws in the wind tunnel.

2. Flutter boundary has only been determined through various simulations. The location of flutter boundary should be determined from experiments in order to draw further conclusions on the LCO behavior near flutter speed.

3. This two dimensional study on a typical wing section may be extended to a three dimensional cantilevered wing. This is a natural extension of the current work towards understanding of nonlinear aeroelastic behavior.

BIBLIOGRAPHY

[1] Dowell, E., Edwards, J., and Strganac, T., "Nonlinear aeroelasticity," *Journal of aircraft*, Vol. 40, No. 5, 2003, pp. 857–874.

[2] Hodges, D. H. and Pierce, G. A., *Introduction to structural dynamics and aeroelasticity*, 15, Cambridge University Press, 2011.

[3] Tang, D. and Dowell, E., "Chaotic stall response of helicopter rotor in forward flight," *Journal of fluids and structures*, Vol. 6, No. 3, 1992, pp. 311–335.

[4] Kim, K. and Strganac, T. W., "Aeroelastic studies of a cantilever wing with structural and aerodynamic nonlinearities," AIAA Paper 1412(2002), 2002.

[5] Thompson, J., DavidE. and Strganac, T., "Nonlinear Analysis of Store-Induced Limit Cycle Oscillations," *Nonlinear Dynamics*, Vol. 39, No. 1-2, 2005, pp. 159–178.

[6] Lucia, D. J., "The sensorcraft configurations: A non-linear aeroservoelastic challenge for aviation," AIAA Paper 1943(2005), 2005.

[7] Silva, W. A., Vartio, E., Shimko, A., Kvaternik, R. G., Eure, K. W., and Scott, R. C., "Development of aeroservoelastic analytical models and gust load alleviation control laws of a sensorcraft wind-tunnel model using measured data," AIAA 1935(2006), 2006.

[8] Silva, W. A., "Reduced-order models based on linear and nonlinear aerodynamic impulse responses," AIAA-99-1262, 1999.

[9] Silva, W. A., Piatak, D. J., and Scott, R. C., "Identification of experimental unsteady aerodynamic impulse responses," *Journal of aircraft*, Vol. 42, No. 6, 2005, pp. 1548–1551.

[10] Kussner, H. G., "Stresses produced in airplane wings by gusts," Tech. Rep. NACA TM 654, 1932.

[11] Bisplinghoff, R. L., Ashley, H., and Halfman, R. L., *Aeroelasticity*, Courier Corporation, 2013.

[12] Ostrower, J., "A Closer Look at 787 Wing Flex," http://www.flightglobal.com/blogs/flightblogger/2008/05/a-closer-look-at-787-wingflex.html, 2008. Online; accessed 4-April-2015.

[13] Bunton, R. W. and Denegri, C. M., "Limit cycle oscillation characteristics of fighter aircraft," *Journal of Aircraft*, Vol. 37, No. 5, 2000, pp. 916–918.

[14] Denegri, C. M., "Limit cycle oscillation flight test results of a fighter with external stores," *Journal of Aircraft*, Vol. 37, No. 5, 2000, pp. 761–769.

[15] ONeil, T., Gilliat, H., and Strganac, T. W., "Investigations of aeroelastic response for a system with continuous structural nonlinearities," AIAA-96-1390, 1996.

[16] Strganac, T. W., Ko, J., and Thompson, D. E., "Identification and control of limit cycle oscillations in aeroelastic systems," *Journal of Guidance, Control, and Dynamics*, Vol. 23, No. 6, 2000, pp. 1127–1133.

[17] Block, J. J. and Strganac, T. W., "Applied active control for a nonlinear aeroelastic structure," *Journal of Guidance, Control, and Dynamics*, Vol. 21, No. 6, 1998, pp. 838–845.

[18] Ko, J., Strganac, T. W., and Kurdila, A. J., "Stability and control of a structurally nonlinear aeroelastic system," *Journal of Guidance, Control, and Dynamics*, Vol. 21, No. 5, 1998, pp. 718–725.

[19] Babbar, Y., Suryakumar, V. S., and Strganac, T. W., "Experiments in Free and Forced Aeroelastic Response," American Institute of Aeronautics and Astronautics, AIAA-2013-0054, 2013,
doi:10.2514/6.2013-54.

[20] Babbar, Y., Suryakumar, V. S., and Strganac, T. W., "An Approach for Prescribed Experiments for Aerodynamic-Structural Dynamic Interaction," American Institute of Aeronautics and Astronautics, AIAA-2013-0056, 2013.

[21] Babbar, Y., Suryakumar, V. S., and Strganac, T. W., "Experiments in Aeroelastic Response and Control under Gust," American Institute of Aeronautics and Astronautics, AIAA-2013-1637.

[22] Christopher, D. and Christine, V., "Survey of applications of active con-trol technology for gust alleviation and new challenges for light-er-weight aircraft," Tech. Rep. NASA TM-2012-216008, 2012.

[23] Theodorsen, T., "General theory of aerodynamic instability and the mechanism of flutter," Tech. Rep. NACA-TR-496, 1949.

[24] Peters, D. A., Karunamoorthy, S., and Cao, W.-M., "Finite state induced flow models. I-Two-dimensional thin airfoil," *Journal of Aircraft*, Vol. 32, No. 2, 1995, pp. 313–322.

APPENDIX A

The following files are attached with this thesis.

1. The matlab script file *ae_solver_main_visc.m* is the main code that accepts initial conditions from the file, *ae_runs_time_domain_visc.xlsx* and plots response information for those initial conditions. Bifurcation boundaries are then extracted from this information. This code uses the matlab function, *ae_solver_fun_visc.m* as the solver function via ODE45.

2. The matlab code, *flutter.m* plots flutter boundaries for various aerodynamic models including quasi-static, quasi-steady, unsteady, and Peter's model.